

A HYPERFINE ANALYSIS OF THE $^4\Pi - X^4\Sigma^-$ TRANSITION OF
RHENIUM MONOCARBIDE

By

Ryan Hall

Bachelor of Science, University of New Brunswick, 2013

A Thesis Submitted In Partial Fulfilment of the Requirements for the Degree of

Master of Science

in the Graduate Academic Unit of Chemistry

Supervisor: Allan G. Adam, Ph. D., Department of Chemistry

Examining Board: Allan G. Adam, Ph. D., Department of Chemistry
John J. Neville, Ph. D., Department of Chemistry
Dennis Tokaryk, Ph. D., Department of Physics

This thesis is accepted by the Dean of Graduate Studies

The University of New Brunswick

August, 2016

© Ryan Hall, 2016

Abstract

In this thesis, the first spectroscopic study of rhenium monocarbide, ReC, is presented. ReC molecules were produced via a supersonic molecular jet apparatus. The ReC spectrum was studied utilizing both high and low-resolution spectroscopic techniques, including laser induced fluorescence (LIF) and dispersed fluorescence (DF). The low-resolution survey scan was performed and four bands from this system were identified, and studied using high-resolution. This clearly revealed the ^{187}ReC and ^{185}ReC isotopologues, and extensive hyperfine structure, which resulted in a complex spectrum. This experimental data appears to be consistent with a $^4\Pi-X^4\Sigma^-$ transition, which agrees with Dr. Grein's [1] calculations. A program has been written using the Hamiltonian matrix for a $^4\Pi - X^4\Sigma^-$ transition, as reported in the literature [2]. After performing a fit using assigned transitions in our spectrum, molecular constants were extracted to describe the molecular system. Dispersed fluorescence spectra were used to extract vibrational information.

References

1. Dr. Friedrich Grein, Personal Communication
2. Adam, A.G., Azuma, Y., Barry, J.A., Merer, A.J., Sassenberg, U., Schröder, J.O., *J. Chem. Phys.*, **100**, 6240-6262 (1994)

Acknowledgements

First and foremost, I would like to thank Dr. Allan Adam for agreeing to become my supervisor for the duration of my Master degree. Without him I would not have had the opportunity to perform research in the laser lab to begin with. He first introduced me to the laser scene and showed me how all the machinery (ancient and new) worked, and then assisted me with the endless hours of data taking. There was also the occasional occurrence of being thrown to the wolves when he had a meeting or other engagement, leaving me to do things on my own, which actually helped me to learn my way around the lab faster. Of course, there were still the occasional reminders when I forgot to turn something on, or what the command line that I wanted was on the computers that are older than I am. After experimentation was done, he then helped me out with processing the huge number of data points into something we can actually deal with, and then helped me to find patterns amongst the thousands of lines in my spectrum. He was also kind enough to explain anything to me that I didn't understand, or that I curiously asked about.

I would also like to really thank Dr. Dennis Tokaryk for essentially being a co-supervisor, if only in practice rather than name. He worked alongside me most of the way through analysing my collected data, and also aided me with much of the computer work so that I would know how to use programs like Igor Pro and Loomis-Wood to do my analysis. His assistance also majorly came into play with the programming aspect of my project, due to my having no previous programming experience whatsoever. Without his assistance with the programming, this would have been a much larger obstacle than it already was. He was also instrumental in teaching me any information I

required to further my understanding of the material constituting my research, which was definitely needed as I was without certain aspects of physics in my background.

Another person in our lab who definitely deserves recognition is Joyce MacGregor for her expert, and sometimes magical, laser technician assistance. She somehow manages to get the more finicky lasers (*cough* cw laser *cough*) to work properly when no one else can, no matter how many times they try. Needless to say, data would have been much more difficult and time costly to gather without her technical mastery. I also have professor emeritus Dr. Colan Linton to thank for his help introducing me to the program pgopher, so that I would have some clue as to how to use it to try to make predictions and fits for my spectrum.

In addition to these specific individuals, there have also been a number of students as members of our group as part of their honours projects. So, I would like to thank Nicole, Ricarda, and Lindsay for livening up the lab and breaking up the extended periods of data analysis at my desk by giving me some more people to chat with. As a whole, the group members of the laser lab have a great sense of humour and are very easy to get along with, which made my experience in the laser lab a very positive one.

Table of Contents

Title Page	i
Abstract	ii
References	iii
Acknowledgements	iv
Table of Contents	vi
List of Tables	ix
List of Figures	xi
Chapter 1 – Introduction	1
References	8
Chapter 2 – Theory	10
2.0 – Electronic Structure of an Atomic System	10
2.1 – Electronic Angular Momentum of Atoms	13
2.2 – Systems of Many-Electron Atoms	16
2.3 – The Angular Momentum of Many-Electron Atoms	17
2.4 – Application of the Schrödinger Equation to Molecules	18
2.5 – Electronic Structure of Diatomic Molecules	21
2.6 – Hund’s Coupling Cases in Diatomic Molecules.	23
2.7 – The Vibrational Structure of Diatomic Molecules	26
2.8 – The Rotational Structure of Diatomic Molecules	32
2.9 – The Rovibrational Structure of Diatomic Molecules	35

2.10 – The Rovibronic structure of Diatomic Molecules	39
2.11 – The Franck-Condon Principle	43
2.12 – Magnetic Hyperfine Structure of Diatomic Molecules	45
2.13 – Parity	51
2.14 – Isotope Effect	55
2.15 – Dispersed Fluorescence	56
References	58
Chapter 3 – Experimental Setup	59
3.0 – The Ablation Source	59
3.1 – Preparation of the Precursor Gas Mixture	61
3.2 – The Rhenium Rod and Formation of Rhenium Monocarbide	63
3.3 – Electronic Components	65
3.4 – Optimization	66
3.5 – Experimental Techniques	67
References	70
Chapter 4 – Spectral Results and Analysis	71
4.0 – Low Resolution Survey	71
4.1 – Dispersed Fluorescence Analysis	73
4.2 – High Resolution Spectral Analysis	76
4.3 – Selective Detection	95
4.4 – ReC Molecular Jet with Argon Carrier Gas at Higher Pressure	96
4.5 – Strategies Utilized to Identify F2/F3 Branches Using the Cold Spectra	99
4.6 – Spectrum Fitting and Constant Determination	102

4.7 – Results of the Fitting Process106
4.8 – Lifetime Determination	111
References	116
Chapter 5 – Conclusions	117
5.0 – Conclusions117
5.1 – Future Considerations	119
References	121
Appendices122
Appendix A – Full Low-Resolution Spectrum	122
Appendix B – DF Spectra With Wavelength Setting of Dye laser.	124
Appendix C – Assignments for the ^{187}ReC Isotopologue in the 426 nm Band.	127
Appendix D – Assignments for the ^{185}ReC Isotopologue in the 426 nm Band.	133
Appendix E – Assignments for the ^{187}ReC Isotopologue in the 438 nm Band.	139
Appendix F – Assignments for the ^{185}ReC Isotopologue in the 438 nm Band.	157
Appendix G – Assignments for the ^{187}ReC Isotopologue in the 448 nm Band.	175
Appendix H – Assignments for the ^{185}ReC Isotopologue in the 448 nm Band.	185
Appendix I – Assignments for the ^{187}ReC Isotopologue in the 462 nm Band.	.194
Appendix J – Assignments for the ^{185}ReC Isotopologue in the 462 nm Band.	.204

Curriculum Vitae

List of Tables

Table 1.1 – The Energies of the Ground and Excited States of ReC.	5
Table 3.1 – List of Laser Dyes Used In Low-Resolution Survey	68
Table 4.1 – Determined Vibrational Parameters	74
Table 4.2 – Comparison of Spacing Between the 438 and 448 nm Bands	86
Table 4.3 – Sample of Program Input	105
Table 4.4 – Sample of Program Output	107
Table 4.5 – List of Parameters as Determined by Our Fit for the 438 nm Band . . .	109
Table 4.6 – Lifetimes of ReC Resulting from Exponential Fits to Decay Curves . .	114
Table C1 – ${}^tR_{3e1e}$ Assignments for the ${}^{187}\text{ReC}$ Isotopologue in the 426 nm Band . .	128
Table C2 – ${}^pQ_{3e4f}$ Assignments for the ${}^{187}\text{ReC}$ Isotopologue in the 426 nm Band . .	131
Table D1 – ${}^tR_{3e1e}$ Assignments for the ${}^{185}\text{ReC}$ Isotopologue in the 426 nm Band . .	134
Table D2 – ${}^pQ_{3e4f}$ Assignments for the ${}^{185}\text{ReC}$ Isotopologue in the 426 nm Band . .	137
Table E1 – ${}^tR_{3e1e}$ Assignments for the ${}^{187}\text{ReC}$ Isotopologue in the 438 nm Band . .	140
Table E2 – ${}^pQ_{3e4f}$ Assignments for the ${}^{187}\text{ReC}$ Isotopologue in the 438 nm Band . .	145
Table E3 – ${}^oP_{3f4f}$ Assignments for the ${}^{187}\text{ReC}$ Isotopologue in the 438 nm Band . .	148
Table E4 – ${}^sQ_{3f1e}$ Assignments for the ${}^{187}\text{ReC}$ Isotopologue in the 438 nm Band . .	150
Table E5 – ${}^qR_{3f4f}$ Assignments for the ${}^{187}\text{ReC}$ Isotopologue in the 438 nm Band . .	153
Table E6 – ${}^tP_{3e1e}$ Assignments for the ${}^{187}\text{ReC}$ Isotopologue in the 438 nm Band . .	155
Table F1 – ${}^tR_{3e1e}$ Assignments for the ${}^{185}\text{ReC}$ Isotopologue in the 438 nm Band . .	158
Table F2 – ${}^pQ_{3e4f}$ Assignments for the ${}^{185}\text{ReC}$ Isotopologue in the 438 nm Band . .	163
Table F3 – ${}^oP_{3f4f}$ Assignments for the ${}^{185}\text{ReC}$ Isotopologue in the 438 nm Band . .	166
Table F4 – ${}^sQ_{3f1e}$ Assignments for the ${}^{185}\text{ReC}$ Isotopologue in the 438 nm Band . .	168

Table F5 – ${}^qR_{3f4f}$ Assignments for the ${}^{187}\text{ReC}$ Isotopologue in the 438 nm Band . . .	171
Table F6 – ${}^rP_{3e1e}$ Assignments for the ${}^{187}\text{ReC}$ Isotopologue in the 438 nm Band . . .	173
Table G1 – ${}^tR_{3e1e}$ Assignments for the ${}^{187}\text{ReC}$ Isotopologue in the 448 nm Band . . .	176
Table G2 – ${}^pQ_{3e4f}$ Assignments for the ${}^{187}\text{ReC}$ Isotopologue in the 448 nm Band . . .	181
Table G3 – ${}^oP_{3f4f}$ Assignments for the ${}^{187}\text{ReC}$ Isotopologue in the 448 nm Band . . .	183
Table H1 – ${}^tR_{3e1e}$ Assignments for the ${}^{185}\text{ReC}$ Isotopologue in the 448 nm Band . . .	186
Table H2 – ${}^pQ_{3e4f}$ Assignments for the ${}^{185}\text{ReC}$ Isotopologue in the 448 nm Band . . .	190
Table H3 – ${}^oP_{3f4f}$ Assignments for the ${}^{185}\text{ReC}$ Isotopologue in the 448 nm Band . . .	192
Table I1 – ${}^tR_{3e1e}$ Assignments for the ${}^{187}\text{ReC}$ Isotopologue in the 462 nm Band . . .	195
Table I2 – ${}^pQ_{3e4f}$ Assignments for the ${}^{187}\text{ReC}$ Isotopologue in the 462 nm Band . . .	200
Table I3 – ${}^oP_{3f4f}$ Assignments for the ${}^{187}\text{ReC}$ Isotopologue in the 462 nm Band . . .	202
Table J1 – ${}^tR_{3e1e}$ Assignments for the ${}^{185}\text{ReC}$ Isotopologue in the 462 nm Band . . .	205
Table J2 – ${}^pQ_{3e4f}$ Assignments for the ${}^{185}\text{ReC}$ Isotopologue in the 462 nm Band . . .	209
Table J3 – ${}^oP_{3f4f}$ Assignments for the ${}^{185}\text{ReC}$ Isotopologue in the 462 nm Band . . .	211

List of Figures

Figure 1.1 – Predicted States and Most Probable Transitions	6
Figure 2.1 – Spin Orbit Coupling Diagram of a $^4\Pi$ Electronic State	23
Figure 2.2 – Vector Diagram of Hund’s Case (a) Coupling Scheme	24
Figure 2.3 – Vector Diagram of Hund’s Case (b) Coupling Scheme	26
Figure 2.4 – Harmonic Potential vs. Morse Potential Comparison	29
Figure 2.5 – Diagram of Rotational Branch Structure	42
Figure 2.6 – Franck-Condon Principle Illustration.	44
Figure 2.7 – Vector Diagram of Hund’s Case ($b_{\beta J}$) Coupling Scheme	50
Figure 2.8 – Parity of $^4\Sigma$ Rotational Energy Levels	53
Figure 2.9 – Parity of $^4\Pi$ Rotational Energy Levels	54
Figure 2.10 – Dispersed Fluorescence Diagram	57
Figure 3.1 – Experimental Setup	61
Figure 3.2 – Setup of Gas Board Used to Create Sample Gas Mixture	62
Figure 3.3 – Diagram of the Stainless Steel Rhenium Rod Housing	65
Figure 4.1 – Low Resolution Survey Scan of ReC	72
Figure 4.2 – Dispersed Fluorescence Spectrum of ReC	75
Figure 4.3 – Full Spectrum of the 438 nm Band at High Resolution	76
Figure 4.4 – Diagram of Transitions from a $^4\Sigma^-$ Ground State to a $^4\Pi$ Excited State . .	78
Figure 4.5 – Loomis-Wood Plot	80
Figure 4.6 – Isotope Identification in 438 nm Band	82
Figure 4.7 – Diagram of Transitions from a $^2\Sigma^-$ Ground State to a $^2\Pi$ Excited State . .	84
Figure 4.8 – Compared Hyperfine Structures in the R Branch	85

Figure 4.9 – Compared Hyperfine Structures in the P Branch	87
Figure 4.10 – Diagram Showing All Possible Transitions	88
Figure 4.11 – Diagram Used to Determine a Combination Difference	90
Figure 4.12 – Labelled Hyperfine Components of the $N'' = 3 \text{ } ^1\text{R}_{3e1e}$	92
Figure 4.13 – Labelled Hyperfine Components of the $N'' = 7 \text{ } ^1\text{Q}_{3e4f}$	93
Figure 4.14 – Transition Diagram of the Hyperfine Structure of the R Branch	94
Figure 4.15 – Comparison of Hot and Cold Low-Resolution Spectra.	98
Figure 4.16 – Comparison of Hot and Cold High-Resolution Spectra.	99
Figure 4.17 – Matrix of the Rotational and Hyperfine Hamiltonian for a $^4\Sigma^-$ state . .	103
Figure 4.18 – Decay Curves for the 426 nm Band	112
Figure 4.19 – More Decay Curves for the 426 nm Band	113
Figure 4.20 – Decay Curves for the 438 nm Band	115
Figure A1 – Full Low-Resolution Survey Scan of ReC	123
Figure B1 – Dispersed Fluorescence With Given Laser Frequencies pt.1	125
Figure B2 – Dispersed Fluorescence With Given Laser Frequencies pt.2	126

Chapter 1

Introduction

Spectroscopy is the science of studying the interactions between matter and electromagnetic radiation, where the radiation can come from various sources such as a laser. During this interaction, energy is absorbed by the matter in question, which in turn excites the molecules making up the matter. There is an emission of energy when the molecules return to their unexcited state. This emitted energy can be recorded, and its frequency is specific to the molecules in question. Spectroscopic techniques have been employed for decades as important tools in both research and routine analytical practice. They have often been used for molecular structure determination, unknown compound characterization, chemical process monitoring, and for quantitative analyses of complex solutions and mixtures. The absorption of radiation is the basis of many spectroscopic methods, and a source of either broadband or tunable monochromatic light is usually needed to record a spectrum.

There was a proliferation of spectroscopic applications due to the introduction of tunable light sources such as the dye laser, which were capable of providing high-powered, monochromatic light that can be tuned as desired. Lasers can also be utilized in experiments requiring low-pressure environments, and some

lasers provide the ability to perform high-resolution spectroscopy. High-resolution spectroscopy is necessary for the determination of finer details in a spectrum, such as the observation of hyperfine interactions, because only high-resolution spectroscopy can provide the line widths needed to resolve these finer details. Rotational structure, in molecules more complicated than diatomic hydrides, generally requires high-resolution techniques in order to resolve the structure. Low-resolution lasers only provide a broad range of frequencies, which decreases the resolution possible, and results in these lasers being most suited for survey work and other lower resolution spectroscopic techniques.

The UNB laser lab has as one of its primary research themes the spectroscopic investigations of small gas-phase transition metal bearing molecules. The majority of these small molecules are transition metal diatomics, where the metal is combined with a simple ligand such as B, C, N, O, F, Si, P, S, Cl, or Br. Larger molecules are also studied by the UNB group using ligands such as CCH or OCH₃. The group is most interested in these transition metal containing molecules due to the interesting electronic properties that arise from the large number of valence electrons present. Rhenium, for example, possesses five valence electrons, as compared to the alkaline earth metals, which possess two valence electrons. The electronic properties of rhenium allow rhenium compounds to be used as strong catalysts for certain chemical reactions or to provide extremely hard compounds for use in industry. The UNB group's research goal is to investigate the properties of the specific bond or bonds present in the molecule being studied, in order to determine the molecular constants that determine the structure of the molecule, i.e. the

rotational constant, which is used to find the bond length. The molecular structure and electronic properties of these small transition metal containing molecules may help other researchers to understand the properties of larger more complex molecules. As an example, a catalyst may contain a transition metal bound to one of the simple ligands listed above. It is hoped that spectroscopic information about that particular bond may prove useful in achieving a better understanding of its role in the catalyst's structure and the catalytic cycle with the hope of designing a better catalyst or implementing better ways to use the catalyst.

The compound investigated in this thesis is rhenium monocarbide (ReC). Rhenium containing compounds have been shown to be important in the field of catalysis in organic and organometallic chemistry [1,2,3] due to their interesting electronic properties, and also throughout industry due to the extreme hardness of some rhenium compounds. Even though this is the case, few spectroscopic studies have been performed to understand the bonding interactions between rhenium and non-metal atoms. This is only the fourth study of a rhenium-containing diatomic molecule, where the three previously studied molecules are ReN [4], ReO [5], and ReF [6]. This study will, therefore, add to the study of rhenium-ligand bonding by introducing a diatomic carbide molecule to the list. This work will also add to the growing list of transition metal diatomic carbide molecules studied such as FeC [7], NiC [8], RuC [9], VC [10], NbC [10], MoC [11], PdC [11], CoC [12], and PtC [13]. In addition to contributing to this growing list of diatomic monocarbides, this research will also assist in revealing trends in transition metal monocarbides across the periodic table.

There have been two theoretical studies performed involving rhenium monocarbide. One is from the literature [15], and the other is the result of a collaboration with Dr. Friedrich Grein, UNB Chemistry Department, prior to the current experiments, in order to get a prediction of what type of transition could be expected to occur, what states are expected for the ground and excited states, and the relative energies of these states [14]. An equilibrium bond length of 1.66Å was determined in these calculations. The results can also be used to estimate the lifetime of a given transition by using the calculated oscillator strengths. The calculations were performed for doublet, quartet, and sextet states, and are summarized in Table 1.1.

Table 1.1 – The energies of the ground and excited states of ReC [14].

State	Relative Energy (cm ⁻¹)	Oscillator Strength
Quartet States		
Σ^-	-	-
Δ	16373	0
Δ	16534	0
Σ^-	18309	0.00017
Φ	23229	0
Φ	23229	0
Π	23309	0.01249
Π	23309	0.01249
Π	28875	0.13955
Π	28875	0.13957
Σ^-	38069	0.16963
Π	40005	0.00098
Π	40005	0.00098
Δ	40570	0
Δ	41215	0
Doublet States (3226 cm ⁻¹ higher than quartet Σ^-)		
Σ^-	-	-
Δ	2420	0
Δ	3388	0
Σ^+	6130	0
Δ	6936	0
Δ	7098	0
Σ^-	14760	0.00001
Σ^-	15325	0.00764
Δ	15566	0
Δ	15728	0
Σ^+	16940	0
Σ^+	17986	0
Π	20970	0.11866
Π	20970	0.11879
Sextet States (43957 cm ⁻¹ higher than quartet Σ^- , and therefore not considered)		

The calculations determined that a $^4\Sigma^-$ state is lowest in energy, and that the nearest $^2\Sigma^-$ state is 3226cm⁻¹ higher in energy. The results also show that the sextet states are much higher in energy so they can be ignored as a possible ground state. The most probable transitions, based on the calculations, would be from the lowest

energy $^4\Sigma^-$ state to one of the $^4\Pi$ states, or to another higher energy $^4\Sigma^-$ state. These transitions are shown in Figure 1.1. The lifetimes of a majority of these transitions are expected to be relatively short because most of the $^4\Pi$ states have relatively large oscillator strengths. A large oscillator strength is indicative of a strong transition, and this in turn results in a quick transition back down to the ground state.

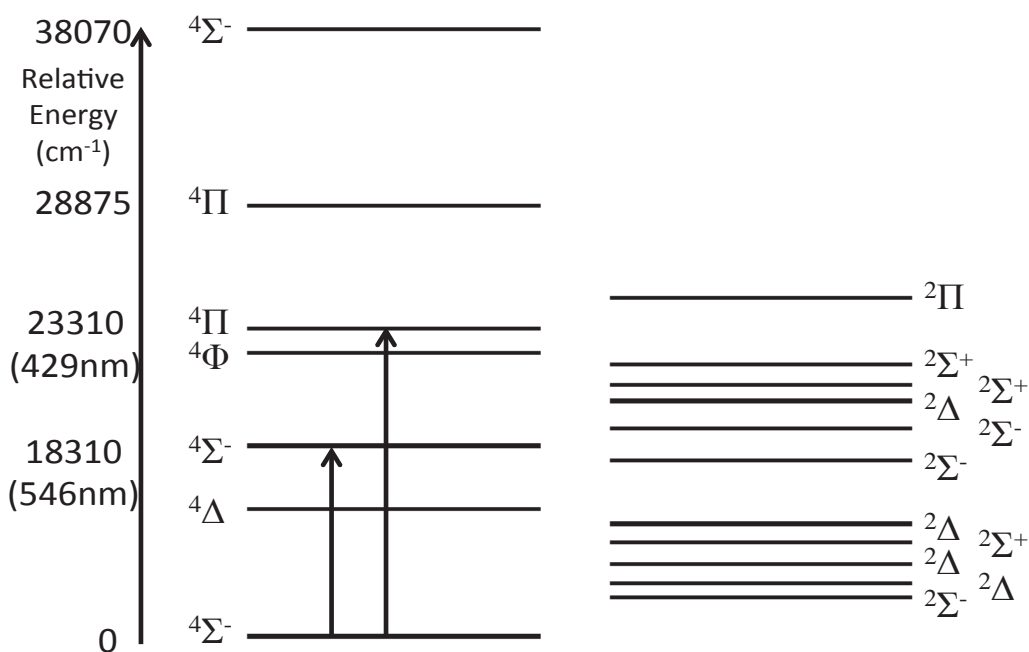


Figure 1.1 – Predicted states and most probable transitions

The theoretical paper [15], which includes rhenium carbide in its calculations, predicts calculated values for the bond length and the vibrational frequency of the ReC molecule in its ground state. The predicted bond length is 1.731\AA as compared with 1.66\AA predicted in the more recent calculations [14], and

the ground state vibrational frequency is 1046 cm^{-1} . A $^4\Sigma^-$ ground state was also predicted.

The current research continues the first experimental spectroscopic study of the ReC molecule by R. Weale [16]. Weale was able to determine that the molecule produced in his experiments was ReC, and optimized the experimental conditions to produce ReC more efficiently with the UNB laser ablation apparatus. The current work's goal is to use high-resolution spectroscopy to resolve the exceedingly complex band structure and identify the transitions in the spectrum. In addition, the presence of both the ^{187}ReC and ^{185}ReC isotopologues, which have relative abundances of 62.6% and 37.4% respectively, must be identified. The rotational constant and other pertinent molecular constants will be determined from a fit to the high-resolution data. A bond length can then be extracted from the rotational constant. The low-resolution technique of dispersed fluorescence will also be employed to determine the ground state vibrational frequency as well as to identify low-lying electronic states.

References

1. Blom, R.H., Kollonitsch, V., Kline, C.H., *Ind. Eng. Chem.* **54** (4), 16-22 (1962)
2. Davenport, W.H., Kollonitsch, V., Kline, C.H., *Ind. Eng. Chem.* **60** (11), 10-19 (1968)
3. Broadbent, H.S., Campbell, G.C., Bartley, W.J., Johnson, J.H., *J. Org. Chem.* **24** (12), 1847-1854 (1959)
4. Balfour, W.J., Cao, J., Qian, C.X.W., Rixon, S.J., *J. Mol. Spec.* **183**, 113-118 (1997)
5. Balfour, W.J., Ram, R.S., *Can. J. Phys.* **62**, 1524-1537 (1984)
6. Launila, O., James, A.M., Simard, B., *J. Mol. Spec.* **164**, 559-569 (1994)
7. Itono, S.S., Taketsugu, T., Hirano, T., Nagashima, U., *J. Chem. Phys.* **115**, 11213-11220 (2001)
8. Brugh, D.J., Morse, M.D., *J. Chem. Phys.* **117**, 10703-10714 (2002)
9. Langenberg, J.D., DaBell, R.S., Shao, L., Dreessen, D., Morse, M.D., *J. Chem Phys.* **109**, 7863-7875 (1998)
10. Hamrick, Y.M., Weltner, W., *J. Chem. Phys.* **94**, 3371-3380 (1991)
11. DaBell, R.S., Meyer, R.G., Morse, M.D., *J. Chem. Phys.* **114**, 2938-2954 (2001)
12. Tzeli, D., Mavridis, A., *J. Phys. Chem. A.* **110**, 8952-8962 (2006)
13. Steimle, T.C., Jung, K.Y., Li, B.Z., *J. Chem. Phys.* **102**, 5937-5941 (1995)
14. Dr. Friedrich Grein, Personal Communication
15. Wang, J., Sun, X., Wu, Z., *J. Cluster Science.* **18**, 333-344(2007)

16. Weale, R., *High Resolution Laser Spectroscopy of Rhenium Carbide*. BSc Honours Thesis, Department of Chemistry, University of New Brunswick (2012)

Chapter 2

Theory

2.0 –Electronic Structure of the Hydrogen Atomic System

Before discussing the electronic structure of a molecular diatomic system, it is reasonable to first discuss the electronic structure of an atomic system to gain an understanding of the principal ideas before applying them to more complex systems. A neutral atom, as is well understood, consists of a positively charged nucleus central to the surrounding electrons, with a total charge equal to that of the nucleus but of negative polarity. These electrons are not stationary, and essentially form an electron ‘cloud’ around the nucleus. Within this simple system, there are various types of energy; both potential and kinetic. The types of potential energies are the Coulombic attraction forces between the electrons and the nucleus, and the Coulombic repulsion forces between electrons. Due to the fact that the electrons are in motion, they are the source of the kinetic energy in the system. Understanding this, we can determine the total energy of the atomic system by taking the sum of these different energies in the form

$$E_{total} = E_{kinetic} + E_{potential}$$

Modern theories have stopped considering the electron as a particle subject to the laws of classical mechanics, which we apply to everyday larger objects, and now treat the electron the same as other entities of sub-atomic size by subjecting it to the laws of quantum mechanics. These quantum mechanical laws are expressed in the Schrödinger equation, which is used to determine various quantities about the system to which it is applied, i.e. the way electrons group themselves around a nucleus, or the way in which a transition may occur between different energy states.

Another important use of the Schrödinger equation is to predict the probability of an electron with a particular energy being at a specific region in space, and this probability is expressed using a special algebraical expression, called a wave function, of the electron. The wave function is represented with the Greek symbol ψ , and is composed of physical constants (such as π , c , h , m , e , etc.), parameters (such as distance from nucleus), and quantum numbers. The quantum numbers arise from the Schrödinger equation, in the sense that the wave function only represents a sensible physical system if the quantum numbers have certain values. The following example is a set of wave functions, ψ_n , which are the solutions to the Schrödinger equation for the hydrogen atom, the simplest atomic system [1].

$$\psi_n = f\left(\frac{r}{a_0}\right) e^{\left(-\frac{r}{na_0}\right)}$$

where r is the radial distance of the electron from the nucleus, $a_0 = h^2 / 4\pi^2 m e^2$, $f(r/a_0)$ is a power series of degree $(n-1)$ in r/a_0 , and n is the principal quantum

number, which has integer values of 1, 2, 3, ..., ∞. The constant a_0 has dimensions of length (approximately 0.5×10^{-8} cm), which means that r/a_0 is a pure number. This results in ψ_n and ψ_n^2 simply being numbers for particular values of r and n , where ψ_n^2 is the probability of finding the electron at a chosen distance r from the nucleus when in the state with the given n value.

It has been determined that the electronic wave function of hydrogen requires four quantum numbers in order to adequately describe the electronic state. These quantum numbers are labelled as n , l , m , and s , and are defined as

$$n = 1, 2, 3, \dots$$

$$l = (n - 1), (n - 2), \dots, 0$$

$$m = \pm l, \pm (l - 1), \dots, 0$$

$$s = +1/2$$

where n is the principal quantum number, l is the orbital (or azimuthal) quantum number, m is the magnetic quantum number, and s is the spin quantum number. The principal quantum number governs the energy and shape of the electronic orbital. The term 'orbital' here is a mathematical function used to calculate the probability of finding an electron in a region around an atom's nucleus. The energy of the orbital is related to the size of the orbital in the sense that the smaller the orbital, the closer an electron will be to the nucleus, and more firmly bound to it. The orbital quantum number, l , governs the shape of the orbital and the electron's angular momentum as it orbits the nucleus within its orbital. The magnetic quantum number,

m , governs how the electrons in an orbital about the nucleus behave when the atom is placed in a magnetic field, and also in what direction a particular orbital is facing. The quantum number, s , is a constant in this case because it governs the spin angular momentum of the electron, which is the same regardless of whether it is in free space or bound to an atom [1,2].

2.1 – Electronic Angular Momentum of Atoms

When an electron is moving in its orbit about a nucleus, it has its own orbital angular momentum, which is measured using the l quantum number corresponding to the orbital. This momentum is quantized and is often expressed in terms of $h/2\pi$ where h is Planck's constant ($6.626 \times 10^{-34} \text{m}^2\text{kg/s}$). $h/2\pi$ is often written as \hbar for the sake of convenience. The orbital angular momentum is represented by the equation

$$|\mathbf{l}| = \sqrt{l(l+1)}\hbar$$

where \mathbf{l} (bold face) is used to show that the orbital angular momentum is a vector quantity. From this point on in this thesis, bold face letters are used to represent vector quantities [1].

In addition to its orbital angular momentum, an electron possesses spin angular momentum due to relativistic effects. This spin is represented by the quantum number s , therefore, the magnitude of the spin angular momentum is given by

$$|\mathbf{s}| = \sqrt{s(s+1)}\hbar = \frac{1}{2}\sqrt{3}\hbar$$

The orbital angular momentum and the spin angular momentum are combined to determine the total angular momentum, written as

$$\mathbf{j} = \mathbf{l} + \mathbf{s}$$

where \mathbf{j} is the total angular momentum. The total angular momentum may also be expressed in terms of the total angular momentum quantum number as

$$|\mathbf{j}| = \sqrt{j(j+1)}\hbar$$

To determine possible allowed values of \mathbf{j} , components of \mathbf{l} and \mathbf{s} are summed along a common direction. Generally the direction chosen is in the z direction. Therefore, the z vector components of \mathbf{l} and \mathbf{s} are summed to get the z vector component of \mathbf{j} . This is shown as

$$j_z = l_z + s_z$$

where the allowed values of l_z are $m = \pm l, \pm (l-1), \dots, 0$, and the allowed values of s_z are $\pm 1/2$. Using these allowed values of l_z and s_z we can determine the allowed values of j_z . As an example, if a p subshell were to be described, the possible values of j_z would be as follows

$$j_z = \left(1 + \frac{1}{2}\right), \left(1 - \frac{1}{2}\right), \left(0 + \frac{1}{2}\right), \left(0 - \frac{1}{2}\right), \left(-1 + \frac{1}{2}\right), \left(-1 - \frac{1}{2}\right)$$

$$= \frac{3}{2}, \frac{1}{2}, \frac{1}{2}, -\frac{1}{2}, -\frac{1}{2}, -\frac{3}{2}$$

All of these components are taken into account when it is stated that the states $j = 3/2$ and $j = 1/2$ are formed with $l = 1$ and $s = 1/2$. For a p electron the total orbital and spin momenta can be combined to give a total momentum of

$$|\mathbf{j}| = \frac{1}{2}\sqrt{15}\hbar \quad \text{or} \quad |\mathbf{j}| = \frac{1}{2}\sqrt{3}\hbar$$

depending on whether \mathbf{l} and \mathbf{s} have the same or opposite direction respectively. This indicates that the total momentum has two different magnitudes and, therefore, has two different energy states depending on the orientation of \mathbf{l} and \mathbf{s} .

It is seen that there are $(2s + 1)$ values of j for every value of l . This relationship is used to describe the multiplicity of the state. When a state is labelled, it incorporates the multiplicity, total angular momentum, and total orbital angular momentum. This is written using a term value which takes the form $^{2s+1}l_j$. Using quantum values from above, the states arising from $l = 1$ and $s = 1/2$ are labelled $^2P_{3/2}$ and $^2P_{1/2}$. Subsequently, states arising from $l = 2, 3,$ and 4 are labelled $D, F,$ and G respectively with the appropriate multiplicity label (doublet for all atomic cases), and j labels [1].

2.2 – Systems of Many-Electron Atoms

Once the atom being described becomes more complicated than a hydrogen atom and gains many more electrons, the picture becomes slightly more complicated. The many electrons in the atoms are still occupying the orbitals with the same type and shape as the s , p , d , ... orbitals that were previously mentioned, but the energies of these electrons vary dramatically depending on the type of atom being described. The energy levels for many-electron atoms are each treated as a different case, where there is no general expression for the energy levels. There are, however, three general rules used to explain how electrons occupy orbitals in large atoms. These rules are generally known as the Aufbau, or building-up rules [1].

The first of these rules is Pauli's principle, which states that each electron in an atom must have a unique set of quantum numbers n , l , l_z , and s_z . This rule results in each orbital of an atom only being able to contain 2 electrons, because to add a third electron would repeat a set of quantum numbers. There can be 2 electrons in the same orbital because they can possess opposite spins, with one electron having $s_z = +1/2$ and the other electron having $s_z = -1/2$.

Once there are more than 3 electrons the second rule comes into play, which states that electrons are likely to occupy the lowest energy orbital possible. After the first and lowest energy orbital is filled with 2 electrons, the next electron is likely to occupy the next lowest energy orbital that is unoccupied or half-vacant. Orbital energies generally increase with an increase in n , as well as an increase in l , as can be demonstrated by the general pattern of energies for various orbitals:

$$1s < 2s < 2p < 3s < 3p < 4s < 3d < 4p < 5s < 4d \dots$$

It must also be recognized that there are degeneracies within this trend. For example, there are actually 3 degenerate $2p$ orbitals, where each is along a different coordinate axis. Therefore, each orbital has $n = 2$, and $l = 1$, but can have $l_z = 1, 0, -1$. This is where we apply the third rule, which determines how electrons are distributed among degenerate orbitals such as the $2p$ orbitals. This third rule is called Hund's rule, and states that when electrons enter degenerate orbitals of the same energy, they first half fill each orbital. This means, for example, that one electron will go into one of the $2p$ orbitals, and the next electron will go into a different $2p$ orbital, etc. Once there is an electron in each of the degenerate orbitals, a fourth electron will pair up with the electron in one of the $2p$ orbitals with the opposite spin of the electron already present. Using these three rules, we are able to construct an electronic configuration for different large atoms [1].

2.3 – The Angular Momentum of Many-Electron Atoms

In larger atoms, there are now multiple electrons having an effect on the total angular momentum of the system, and this must be taken into account. There are two main ways for this to occur, where the methods differ by the way in which the orbital and spin momenta are summed to get the total angular momentum. The first method, known as Russell-Saunders coupling, involves the summation of the orbital and spin contributions separately and then adding the total orbital and total spin contributions to form the total angular momentum as follows:

$$\sum \mathbf{l}_i = \mathbf{L}, \quad \sum \mathbf{s}_i = \mathbf{S}$$

$$\mathbf{L} + \mathbf{S} = \mathbf{J}$$

This first method tends to be most applicable for small to medium sized atoms. The second method involves the summation of the orbital and spin contributions of individual electrons separately to get total angular momentum for each electron, and then summing the total angular momentum of each electron to get the total angular momentum as follows [1]:

$$\mathbf{l}_i + \mathbf{s}_i = \mathbf{j}_i$$

$$\sum \mathbf{j}_i = \mathbf{J}$$

This second method tends to be the most applicable for large atoms.

2.4 – Application of the Schrödinger Equation to Molecules

The previously described atomic models must now be expanded upon by using the Schrödinger equation to describe a molecular situation. The Schrödinger equation may be expressed as

$$\hat{H}\Psi = E\Psi$$

where \hat{H} is the Hamiltonian operator, E is the energy, and Ψ is the wave function [3].

A common approximation used in molecular spectroscopy is the nonrelativistic

molecular Hamiltonian operator, where the motion due to the electrons is separated from the nuclear motion. This Hamiltonian is given by

$$\hat{H} = T_N + T_e + V_{NN} + V_{eN} + V_{ee}$$

where T_N , T_e , V_{NN} , V_{eN} , and V_{ee} are the nuclear kinetic, electronic kinetic, nuclear-nuclear repulsion, electron-nuclear attraction, and electron-electron repulsion energies respectively. V_{NN} is not present in the simple atomic case, because it describes the interaction between nuclei of different atoms.

The Schrödinger equation written with this Hamiltonian is difficult to solve and this leads to the necessity of using further approximations. An appropriate treatment was formulated in 1927 by Born and Oppenheimer, and is now called the Born-Oppenheimer approximation. The approximation makes the assumption that electronic motion can be separated from the nuclear motion due to the large difference in particle size, and speed of motion between electrons and nuclei. This large difference allows us to approximate the nuclei to be stationary (fixed in position), and the nuclear separation utilized as a parameter in describing the electrons in motion around the nuclei. Therefore, the total Hamiltonian can be separated into an electronic and a nuclear Hamiltonian, as represented by

$$\hat{H}_{total} = \hat{H}_{electronic} + \hat{H}_{nuclear}$$

In the same way that electronic motion is much faster than nuclear motion, the vibrations within a molecule are much faster than the rotations in a molecule. This further allows the nuclear Hamiltonian to be separated into vibrational and rotational parts, so that the total Hamiltonian can now be expressed as

$$\hat{H}_{total} = \hat{H}_{electronic} + \hat{H}_{vibrational} + \hat{H}_{rotational}$$

This approximation simplified the calculations of molecular energy levels by stating that the electronic, vibrational, and rotational energies can be considered independent of each other, meaning that the total energy of the molecular system is the addition of the independent energy components as follows:

$$E_{total} = E_{electronic} + E_{vibrational} + E_{rotational}$$

Information about all three of these energy components can be provided by spectroscopy. Multiple electronic transitions can be observed in low-resolution spectra, and these are composed of multiple vibrational bands, which can also be observed. Rotational structure may also be observed in these vibrational bands through the use of high-resolution spectroscopy. A spectrum of this type is referred to as a rovibronic spectrum because it is composed of rotational, vibrational, and electronic components [3]. The effects of these different types of motions on the energy of the molecule will be discussed in later sections in this chapter.

2.5 – Electronic Structure of Diatomic Molecules

The labeling of the electronic states must be understood before moving on to introduce Hund's cases and the states present in ReC. There are three different types of angular momenta present in a diatomic molecule, ignoring nuclear spin, that make up the total angular momentum (**J**); these are the electron orbital (**L**), electron spin (**S**), and molecular rotational (**R**) angular momenta. The orbital angular momentum is used to describe electron motion, and as in the atomic case it is composed of all of the individual electronic angular momenta, l_i , and can be expressed as a sum [4].

$$\mathbf{L} = \sum_i l_i$$

The total spin angular momentum is also like the atomic case and can be expressed as

$$\mathbf{S} = \sum_i s_i$$

where s_i is the electronic spin angular momentum for one electron. The total rotational orbital angular momentum is also expressed as a sum

$$\mathbf{R} = \sum_j r_j$$

where r_j is the rotational angular momentum of nucleus j about the center of mass. **R** describes the end-over-end tumbling motion of a molecule about a centre of mass,

which is not present in the simple atomic case because rotating about the centre of mass of an atom is simply rotation of a nucleus. To get the total angular momentum, \mathbf{J} , the sum of all these angular momenta is performed

$$\mathbf{J} = \mathbf{L} + \mathbf{S} + \mathbf{R}.$$

Each of these momenta have projections along the molecular axis. Λ is the projection of \mathbf{L} onto the internuclear axis, and the quantum number associated with it is given by $\Lambda = |-L, -L + 1, \dots L|$. Σ is the projection of \mathbf{S} onto the internuclear axis, and the quantum number associated with it is given by $\Sigma = -S, -S + 1, \dots S$. The total projection, the sum of vectors Λ and Σ , is denoted as Ω , and the quantum number associated with it is $\Omega = |\Lambda + \Sigma|$ [4].

Electronic states are labeled with respect to their angular momentum quantum numbers that describe them. The label has the general form

$$^{2S+1}\Lambda_{\Omega}$$

where $2S+1$ refers to the multiplicity of the state. Λ has possible values of 0, 1, 2, 3...etc., and these are given the labels $\Sigma, \Pi, \Delta, \Phi$...etc. respectively, similar to the s, p, d, f, labels in atoms. When there are no other interactions present, the multiple electronic states for a given Λ remain degenerate. However, there are small interactions which remove the degeneracy. The electron spin magnetic moment interacts with the magnetic field caused by the orbital motion of the charged

electrons. This causes a spin-orbit coupling between \mathbf{L} and \mathbf{S} . This coupling splits the $2S+1$ components for a given Λ into separate substates labelled by the value of Ω [4]. An example of the $^{2S+1}\Lambda_{\Omega}$ notation for a $^4\Pi$ state is shown in Figure 2.1. Here $S=3/2$, $\Lambda=1$ and Ω can take the values $5/2$, $3/2$, $1/2$, and $-1/2$. The degeneracy of these four substates is lifted by the spin-orbit interaction.

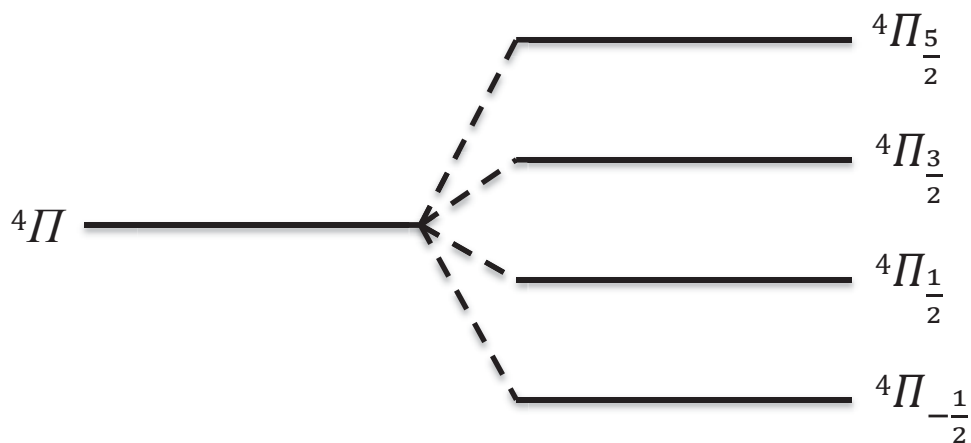


Figure 2.1 – Spin orbit coupling diagram of a $^4\Pi$ electronic state.

2.6 – Hund’s Coupling Cases in Diatomic Molecules

Hund was the first to produce a series of angular momentum coupling cases that can be used to describe diatomic molecules. Each angular momentum coupling case results in a set of quantum numbers that are appropriate for describing a diatomic molecule that follows that particular scheme of adding the momenta together. In each of these cases, the appropriate set, or “good” quantum numbers are the fixed values obtained by projecting various momenta onto the internuclear axis.

The most common scheme for angular momentum coupling in molecules is Hund's case (a). This case is applicable when \mathbf{L} and \mathbf{S} couple strongly to the electric and magnetic fields produced along the internuclear axis. These strong interactions are most probable because the coupling between electronic motion and molecular rotation is very weak. The vector $\mathbf{\Omega}$ that results is well defined as $\mathbf{\Lambda} + \mathbf{\Sigma}$, and couples with the nuclear rotation angular momentum, \mathbf{R} , resulting in the total angular momentum, \mathbf{J} [2]. This is shown in Figure 2.2.

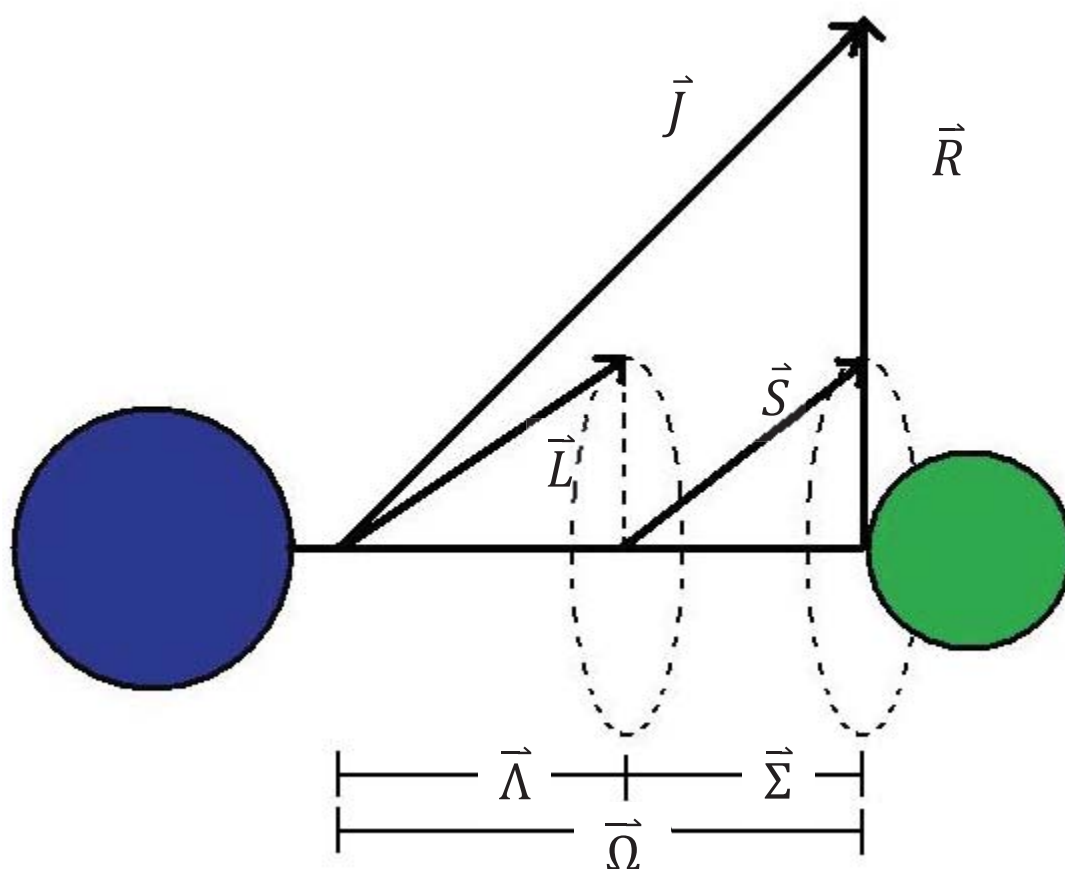


Figure 2.2 – Vector diagram of Hund's case (a) coupling scheme.

Hund's case (b) occurs when the electron spin is coupled more strongly to the total angular momentum without spin, $\mathbf{N} = \mathbf{J} - \mathbf{S}$, than to fields along the internuclear axis. The total angular momentum \mathbf{N} is formed by coupling the orbital angular momentum, \mathbf{L} , and the nuclear rotation angular momentum, \mathbf{R} . \mathbf{N} and \mathbf{S} are added together resulting in the total angular momentum \mathbf{J} . The orbital angular momentum, \mathbf{L} , is still strongly coupled to the intermolecular axis. This coupling scheme is shown in Figure 2.3. Molecules which have a Σ electronic state or a large \mathbf{R} follow the case (b) scheme. This is also true for any case where \mathbf{S} is uncoupled from the fields along the internuclear axis. This coupling scheme means that Ω is no longer well defined as it was in Hund's case (a) [2, 5]. Hund's case (b) is the most appropriate case that best fits the situation for the ground state of rhenium carbide, while Hund's case (a) is most appropriate for the upper Π state in ReC. There are also Hund's cases (c), (d), and (e) [2], but they are not relevant to this thesis.

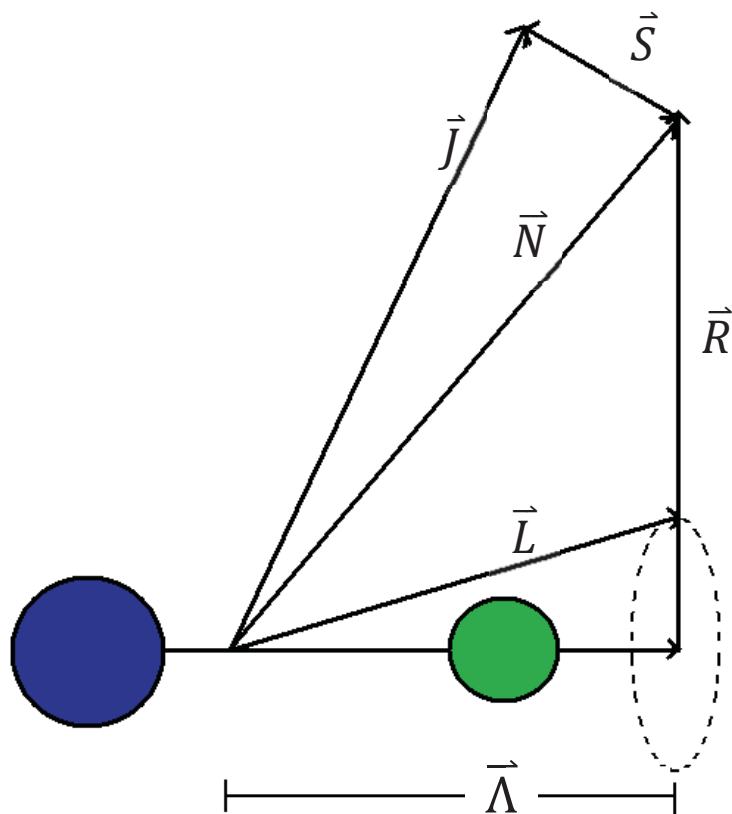


Figure 2.3 – Vector diagram of Hund's case (b) coupling scheme.

2.7 – The Vibrational Structure of Diatomic Molecules

A motion not present in atoms is the vibrational motion between nuclei. When describing a diatomic molecule, there is a balancing of forces that must be considered. There is repulsion between the electrons moving around each of the two nuclei, and also repulsion between the two nuclei as well, plus there is the attraction between the nuclei and the electrons, which is the force responsible for creating bonds between atoms. When these forces are balanced, there is an equilibrium at which the distance between the two nuclei is optimal. The potential energy of the system is at its minimum at this point. If the nuclei are forced closer together, the

repulsive forces increase rapidly, and if the nuclei are drawn apart, the attractive forces resist. To move the nuclei closer or farther apart requires the input of energy into the system. As the bond is distorted more, it requires more energy to do so, and this can be plotted as potential energy against the internuclear bond distance, where the minimum point is referred to as the equilibrium distance r_{eq} . The motion of stretching and compressing the bond may be compared to the motions of a spring, which obeys Hooke's law. Therefore, we can write

$$f = -k(r - r_{eq})$$

where f is the restoring force, k is the force constant, and r is the internuclear distance. In this case the resulting potential energy curve is parabolic and is described by the equation

$$E = \frac{1}{2}k(r - r_{eq})^2$$

This simplistic model of a vibrating molecule is referred to as the simple harmonic oscillator model, which is only an approximation, but provides a good place to start from in order to build a more accurate description of the energy profile for vibrations of a diatomic molecule [1].

As energy increases in the simple harmonic oscillator model, the amount of compression or extension will increase, but the vibrational frequency does not change. The vibrational frequency is dependant upon the masses in the system (the

masses of the two atoms) and the force constant, but independent of the amount that the bond is distorted. This oscillation frequency can be represented by the equation

$$\bar{\omega}_{osc} = \frac{1}{2\pi c} \sqrt{\frac{k}{\mu}}$$

where the units are cm^{-1} . In this equation, c is the speed of light in cm/s , and μ is the reduced mass where the reduced mass is defined as

$$\mu = \frac{m_1 m_2}{m_1 + m_2}$$

with m_1 and m_2 being the masses of atoms one and two respectively.

Utilizing the Schrödinger equation, the allowed quantized vibrational energies may be calculated for any particular molecular system. In the case of the simple harmonic oscillator, these vibrational energies turn out to be defined by

$$\varepsilon_v = \left(v + \frac{1}{2}\right) \bar{\omega}_{osc} \quad (v = 0, 1, 2, 3, \dots)$$

and are shown in Figure 2.4.

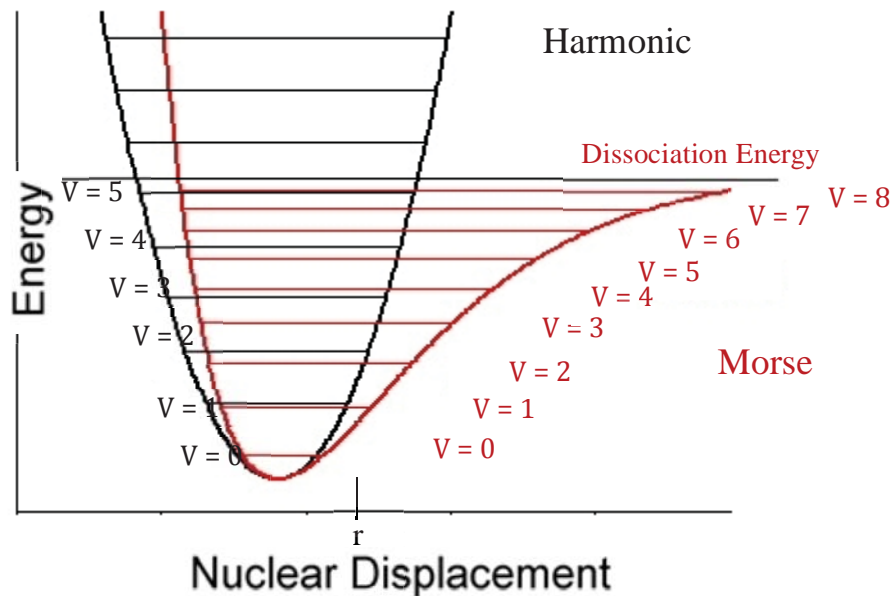


Figure 2.4 – Diagram comparing the harmonic potential energy well to the Morse potential energy well for a diatomic molecule.

One major point to note, is that the energy of the system is never able to reach zero, as the lowest allowed energy in the system is defined as

$$\epsilon_0 = \frac{1}{2} \bar{\omega}_{osc}$$

which cannot be zero. This indicates that the molecule is not able to ever have zero vibrational energy at any given time, and the atoms are never completely stationary with respect to each other. Further, we can state the simple selection rule for the simple harmonic oscillator undergoing vibrational changes [1, 3]

$$\Delta v = \pm 1$$

If we apply this selection rule we get

$$\varepsilon_{v+1 \rightarrow v} = \left(v + 1 + \frac{1}{2} \right) \bar{\omega}_{osc} - \left(v + \frac{1}{2} \right) \bar{\omega}_{osc} = \bar{\omega}_{osc}$$

$$\varepsilon_{v \rightarrow v+1} = \bar{\omega}_{osc}$$

for emission and absorption respectively, regardless of the value of v . This is due to all the vibrational levels being equally spaced as seen in figure 2.4, meaning a transition between any two levels will result in the same change in energy.

While the simple harmonic oscillator helps to begin building a picture, real molecules do not follow the laws of simple harmonic motion, and do not obey Hooke's law. In a real molecule, the bond between atoms may only be stretched so far before it breaks and the molecule dissociates into separate atoms. Therefore, while a molecule may be close to a simple harmonic oscillator at very small vibrations, the picture is much different at larger vibrations and the extremes of the internuclear distance. The differences between the simple harmonic parabola and the curve of a typical diatomic molecule can be observed in figure 2.4. The Morse potential is a function that produces a good approximation of this system by asymptotically approaching the bond dissociation limit as the internuclear distance increases beyond the equilibrium point, and it can be used with the Schrödinger equation to produce analytical solutions. The Morse function is defined as

$$E = D_{eq} [1 - e^{a(r_{eq}-r)}]^2$$

where a is a constant for a particular molecule, and D_{eq} is the dissociation energy [1, 3]. When used in conjunction with the Schrödinger equation, the allowed vibrational energy level pattern is described by

$$\varepsilon_v = \varpi_e \left(v + \frac{1}{2} \right) - \varpi_e x_e \left(v + \frac{1}{2} \right)^2 \quad (v = 0, 1, 2, 3, \dots)$$

where ϖ_e is the oscillation frequency expressed as a wavenumber, and $\varpi_e x_e$ is the corresponding anharmonicity constant. The anharmonicity constant is always small and positive, and defines how the vibrational energy levels get closer together with increasing v . It should be mentioned here that this energy expression is also still only an approximation, and that to have a more precise expression higher order terms with respect to $\left(v + \frac{1}{2} \right)$ would have to be included along with each term's anharmonicity constant ($y_e, z_e, etc.$). These terms are only significant at high values of v , so they shall be ignored during the rest of this section. When solved for the ground state ($v = 0$), we get

$$\varepsilon_0 = \frac{1}{2} \varpi_e \left(1 - \frac{1}{2} x_e \right)$$

which differs from the harmonic oscillator zero point energy by the additional factor.

New selection rules for the anharmonic oscillator are derived to be

$$\Delta v = \pm 1, \pm 2, \pm 3, \dots$$

which introduces the added possibility of larger transitions of more than one vibrational energy level. In practice it becomes increasingly improbable to observe transitions as Δv becomes larger. As an example, the first couple of transitions from the ground state to the first and second vibrational energy levels are described by

$$\begin{aligned}\varepsilon_{v=0 \rightarrow 1} &= \left(1 + \frac{1}{2}\right) \bar{\omega}_e - \left(1 + \frac{1}{2}\right)^2 \bar{\omega}_e x_e - \frac{1}{2} \bar{\omega}_e - \left(\frac{1}{2}\right)^2 \bar{\omega}_e x_e \\ &= \bar{\omega}_e (1 - 2x_e) \\ \varepsilon_{v=0 \rightarrow 2} &= \left(2 + \frac{1}{2}\right) \bar{\omega}_e - \left(2 + \frac{1}{2}\right)^2 \bar{\omega}_e x_e - \frac{1}{2} \bar{\omega}_e - \left(\frac{1}{2}\right)^2 \bar{\omega}_e x_e \\ &= 2\bar{\omega}_e (1 - 3x_e)\end{aligned}$$

Due to x_e being a small positive number, the resulting transitions lie very close to $\bar{\omega}_e, 2\bar{\omega}_e, 3\bar{\omega}_e$, etc. The transition near $\bar{\omega}_e$ is referred to as the fundamental absorption, while the transitions near $2\bar{\omega}_e$ and $3\bar{\omega}_e$ are referred to as the first and second overtones respectively [1, 3].

2.8 – The Rotational Structure of Diatomic Molecules

To begin building a rotational picture for a diatomic molecule, it is easiest to begin with the assumption that the molecule is rigid. This implies that the distance between nuclei remains the same as the molecule rotates through space. Therefore, there is a centre of mass between the two nuclei, about which the molecule rotates. The molecule's moment of inertia for rotation about the centre of mass is defined as

$$\begin{aligned}
 I &= m_1 r_1^2 + m_2 r_2^2 \\
 &= r_1 r_2 (m_1 + m_2)
 \end{aligned}$$

where m_1 and m_2 are the masses of atoms 1 and 2 respectively, and r_1 and r_2 are the distances from atoms 1 and 2 to the centre of mass respectively. If r_0 is to be defined as the total bond length, we may substitute and rearrange to attain the equation

$$I = \frac{m_1 m_2}{m_1 + m_2} r_0^2 = \mu r_0^2$$

where I is now calculated with respect to the reduced mass, μ , and the bond length. When the Schrödinger equation is used to determine allowed rotational energy levels, we get

$$\varepsilon_J = \frac{h}{8\pi^2 I_C} J(J + 1), \quad J = 0, 1, 2, \dots$$

which is usually abbreviated to

$$\varepsilon_J = B J(J + 1), \quad J = 0, 1, 2, \dots$$

where B is the rotational constant, which is given by [1, 3]

$$B = \frac{h}{8\pi^2 I_{BC}}$$

The gap between rotational energy levels can then be determined by taking the difference between consecutive levels with different J values, as follows:

$$\varepsilon_{J=1} - \varepsilon_{J=0} = 2B - 0 = 2B$$

$$\varepsilon_{J=2} - \varepsilon_{J=1} = 4B$$

These energy level gaps show that the gaps become larger as J increases. Generally it can be shown that for a given transition from a level J to a level $J+1$ we get

$$\bar{\nu}_{J \rightarrow J+1} = 2B(J + 1)$$

When dealing with real molecular bonds, however, we know that these bonds are elastic to some extent, which means that they will vary from the rigid model approximation. What is actually observed is that as J increases, classically implying that the speed of rotation is increasing, the centrifugal force acting on the molecule pulls the two nuclei apart. As a result of the centrifugal force, the bond length increases as the value of J increases. We also know, as discussed in the last section, that elastic bonds are able to vibrate. A consequence of changing the bond length during rotations is a change in B as well. This can clearly be seen in the equation for B , because it is proportional to the inverse of the bond length [1, 3]. The rotational constant B can, therefore, be modelled with a changing amount of vibration. This is explained in more detail in section 2.9.

The Schrödinger equation may now be used on the non-rigid molecule to produce

$$\varepsilon_J = BJ(J + 1) - DJ^2(J + 1)^2, \quad J = 0, 1, 2, \dots$$

where D is the centrifugal distortion constant, which is given by

$$D = \frac{h^3}{32\pi^4 I^2 r^2 k c}$$

The rotational selection rule of $\Delta J \pm 1$ is now applied. This rule comes about as a result of a photon being considered to have a single unit of quantized angular momentum, which only allows the angular momentum J to change by one unit during emission or absorption. The expression for a given transition is now written as

$$\varepsilon_{J+1} - \varepsilon_J = \bar{\nu}_J = 2B(J + 1) - 4D(J + 1)^3$$

which shows that the transitions are very similar to a rigid model with the additional term to account for centrifugal distortions of the bond [1].

2.9 – The Rovibrational Structure of Diatomic Molecules

The vibrational energy levels described in the earlier section usually have large energy level separations. For example, HCl and NiC [6] possess energy level spacings of approximately 3000 cm^{-1} and 900 cm^{-1} respectively. Generally diatomic

molecules will have vibrational energy level spacing ranging from about 500 cm^{-1} to 4000 cm^{-1} , depending on the atoms involved. The molecule is also able to rotate through space as discussed in the previous section, and the rotational energy level separations are usually on the order of $<10 \text{ cm}^{-1}$, depending on the size of B. The magnitude of the energy level spacing is significantly different between vibrational levels compared to rotational levels, and this large difference allows us to consider the vibrational and rotational motions separately. We can therefore assume that the total rovibrational energy of the system is equivalent to the sum of the separate vibrational and rotational energies, which is shown as

$$\varepsilon_{total} = \varepsilon_{rot} + \varepsilon_{vib}$$

and if we substitute using the previous equations for vibrational and rotational energy we get

$$\varepsilon_{J,v} = BJ(J + 1) - DJ^2(J + 1)^2 + \bar{\omega}_e \left(v + \frac{1}{2} \right) - \bar{\omega}_e x_e \left(v + \frac{1}{2} \right)^2$$

For the sake of simplicity, the centrifugal distortion term will be temporarily ignored during the following derivation, but is brought back in at the end expression. This energy expression follows the selection rules of both the vibrational and rotational energy expressions, and when the selection rules are applied, we arrive at the general expression for a transition from $v = 0$ to $v = 1$:

$$\begin{aligned}\Delta\varepsilon_{J,v} &= \varepsilon_{J',v=1} - \varepsilon_{J'',v=0} \\ &= \bar{\omega}_0 + B(J' - J'')(J' + J'' + 1)\end{aligned}$$

where $\bar{\omega}_0$ replaces $\bar{\omega}_e(1 - 2x_e)$ and is often called the band origin. It is important to note that B is the same in the upper and lower states only because of the assumption that the rotations of the molecule are not affected by the vibrational changes in the molecule [1]. For transitions of $\Delta J = \pm 1$ we get

$$\begin{aligned}\Delta\varepsilon_{J,v} &= \bar{\omega}_0 + 2B(J'' + 1), \quad J'' = 0, 1, 2, \dots \\ \Delta\varepsilon_{J,v} &= \bar{\omega}_0 - 2B(J' + 1), \quad J' = 0, 1, 2, \dots\end{aligned}$$

respectively. We may combine these equations to make the general expression

$$\Delta\varepsilon_{J,v} = \bar{\omega}_0 + 2Bm, \quad m = \pm 1, \pm 2, \dots$$

where m is positive for $\Delta J = +1$, and negative for $\Delta J = -1$. If we now reintroduce the centrifugal distortion constant term, the expression takes the form

$$\Delta\varepsilon_{J,v} = \bar{\omega}_0 + 2Bm - 4Dm^3, \quad m = \pm 1, \pm 2, \dots$$

It is important to note that relative to the other terms in the expression, the centrifugal distortion term is very small and is often neglected. This expression introduces two patterns of lines in a spectrum, where one is higher frequency

compared to the band origin, and the other is lower frequency. These two patterns correspond to the lines resulting from $\Delta J = \pm 1$, where the lines to higher frequency ($\Delta J = +1$) are referred to as a R branch, and the lower frequency line ($\Delta J = -1$) are referred to as a P branch. This notation becomes clearer later in this chapter with the inclusion of electronic energy.

This picture changes slightly, however, once the Born-Oppenheimer approximation breaks down. As previously discussed, the bond length slightly increases as the vibrational energy increases, and the rotational constant B is inversely proportional to the bond length. This means that a higher vibrational energy level should correspondingly have a slightly smaller value for B [1]. This relationship can be written in the form

$$B_v = B_e - \alpha \left(v + \frac{1}{2} \right)$$

where B_v is the rotational constant at a given vibrational energy level in terms of the equilibrium rotational constant, B_e and a small positive constant, α , for a given molecule. Taking this into account, the transitions for $\Delta J = \pm 1$ respectively are

$$\Delta \varepsilon_{J,v} = \bar{\nu}_R = \bar{\omega}_0 + (B_1 + B_0)(J' + 1) + (B_1 - B_0)(J'' + 1)^2, \quad J'' = 0, 1, 2 \dots$$

$$\Delta \varepsilon_{J,v} = \bar{\nu}_P = \bar{\omega}_0 - (B_1 + B_0)(J' + 1) + (B_1 - B_0)(J' + 1)^2, \quad J' = 0, 1, 2 \dots$$

where B_1 and B_0 are the rotational constants for the upper and lower vibrational energy levels respectively. It may be noted here that the value of B_1 is always

smaller than that of B_0 . These equations may then be combined to form the general equation

$$\Delta\varepsilon_{J,v} = \bar{\nu}_{P,R} = \bar{\omega}_0 + (B_1 + B_0)m + (B_1 - B_0)m^2 - 4Dm^3, \quad m = \pm 1, \pm 2, \pm 3 \dots$$

where the centrifugal distortion term is included. Once again we take the positive m value for the R branch and the negative m value for the P branch [1, 3].

2.10 – The Rovibronic structure of Diatomic Molecules

As mentioned earlier in this chapter, the Born-Oppenheimer approximation allows us to state that the total energy of a diatomic molecular system is the sum of the electronic, vibrational, and rotational energies. Therefore we can write

$$\varepsilon_{total} = \varepsilon_{electronic} + \varepsilon_{vibrational} + BJ(J + 1)$$

$$\Delta\varepsilon_{total} = \Delta\varepsilon_{electronic} + \Delta\varepsilon_{vibrational} + \Delta[BJ(J + 1)]$$

where the second expression represents a change in total energy. We can ignore the centrifugal distortion constant to a very good approximation. A line in a spectrum corresponding to this change in total energy is shown by the expression

$$\bar{\nu}_{spec} = \bar{\nu}_{(v',v'')} + \Delta[BJ(J + 1)]$$

where $\bar{\nu}_{(v',v')}$ is used to represent the wavenumber of a vibronic transition, and the rotational term is separately added to this. The rotational term is the term to be most concerned with at this point.

When determining the selection rule for the possible values of J, we must now consider what electronic states are involved in the transition. To summarize, if both the upper and lower electronic states are $^1\Sigma$ states, the selection rule is $\Delta J = \pm 1$. This is because there is no electronic angular momentum about the internuclear axis in this state. In transitions, where at least one of the states has angular momentum about the internuclear axis, the selection rule becomes $\Delta J = 0, \pm 1$. In all cases, a change in J of 0 is only possible if J is not equal to 0. As a result of these rules we see the appearance of R and P branches as before, as well as Q ($\Delta J = 0$) branches when the appropriate states are involved in the transition [1]. The expression for a rovibronic transition may now be expanded to

$$\bar{\nu}_{spec} = \bar{\nu}_{(v',v')} + B'J'(J' + 1) - B''J''(J'' + 1)$$

where B' and J' refer to the upper electronic state, and B'' and J'' refer to the lower electronic state. Once we apply the selection rules to this expression we gain the expressions for the R, P, and Q branches as follows:

$$\Delta\varepsilon = \bar{\nu}_R = \bar{\nu}_{(v',v')} + (B' + B'')(J'' + 1) + (B' - B'')(J'' + 1)^2, \quad J'' = 0, 1, 2, \dots$$

$$\Delta\varepsilon = \bar{\nu}_P = \bar{\nu}_{(v',v')} - (B' + B'')(J' + 1) + (B' - B'')(J' + 1)^2, \quad J' = 0, 1, 2, \dots$$

$$\Delta\varepsilon = \bar{\nu}_Q = \bar{\nu}_{(v',v')} + (B' - B'')J'' + (B' - B'')J''^2, \quad J'' = 1, 2, 3, \dots$$

where the expression for R and P transitions may be combined to form

$$\bar{\nu}_{R,P} = \bar{\nu}_{(v',v'')} + (B' + B'')m + (B' - B'')m^2, \quad m = \pm 1, \pm 2, \dots$$

with positive m values for a R branch and negative m values for a P branch.

There are selection rules that determine allowed electronic transitions, just as there are for vibrational and rotational transitions. The electronic transition must occur between two electronic state such that $\Delta\Lambda = 0, \pm 1$. The electronic states must also have the same multiplicity, which may be expressed as $\Delta S = 0$. Consequently we also have $\Delta\Omega = 0, \pm 1$ [1, 3]. These selection rules, in combination with the previously mentioned rules, determine what rovibronic transitions are allowed to occur in a given molecule. A diagram showing allowed rovibronic transitions between arbitrary electronic states is available in Figure 2.5.

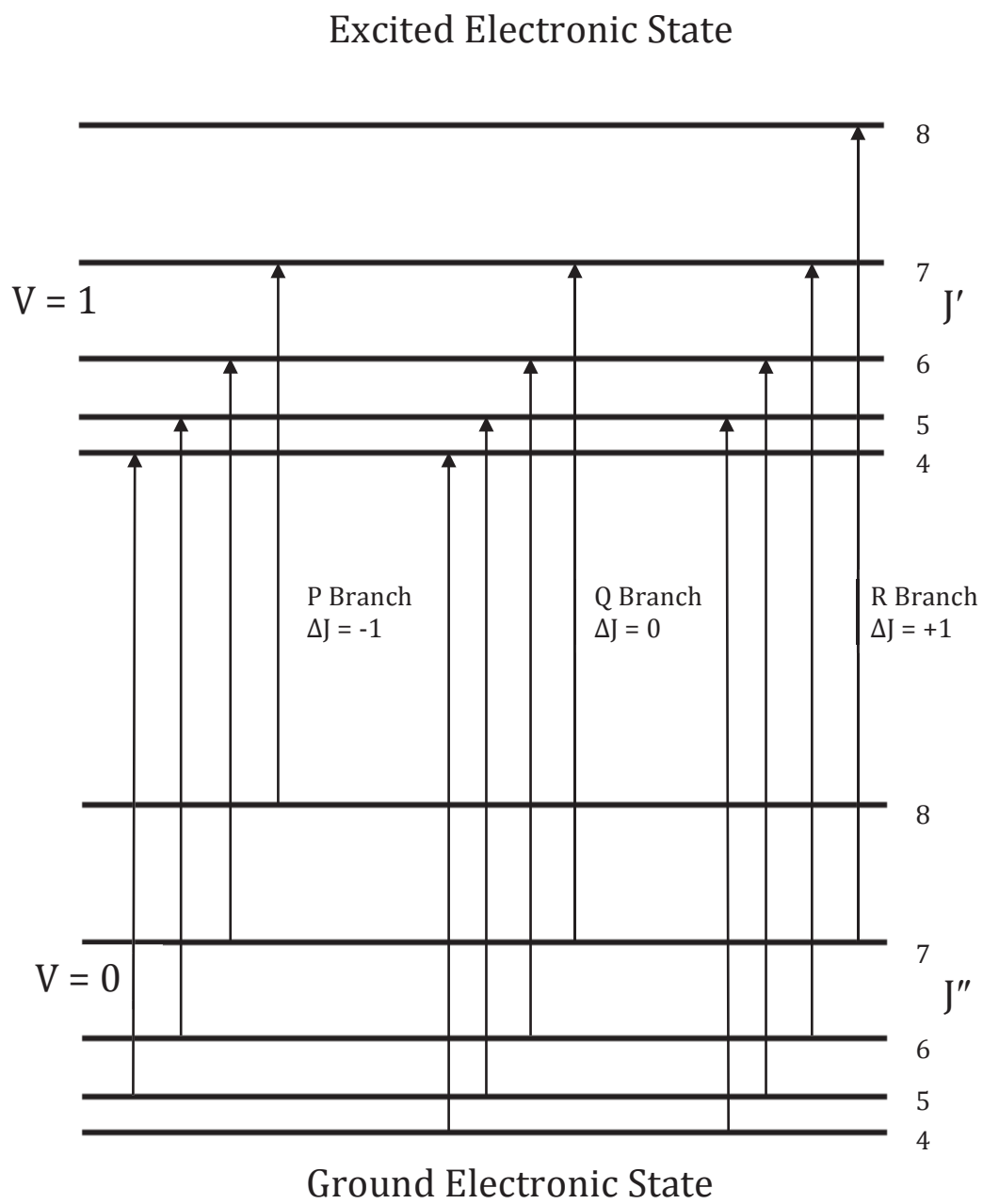


Figure 2.5 – Diagram of rotational branch structure, composed of P, Q, and R branches, for a diatomic molecule.

2.11 – The Franck-Condon Principle

The Franck-Condon principle determines the intensities of the various vibronic transitions. The intensity of a given vibrational transition is proportional to the amount of overlap present between the wavefunctions of the two states involved in the transition [7]. This can be represented as

$$I \propto |\mathbf{R}_{ev}|^2$$

where \mathbf{R}_{ev} is the transition moment, which is given by

$$\vec{\mathbf{R}}_{ev} = \langle \Psi'_{ev} | \vec{\mu} | \Psi''_{ev} \rangle$$

where $\vec{\mu}$ is the electric dipole operator and Ψ'_{ev} and Ψ''_{ev} are the vibronic wavefunctions of the upper and lower states respectively. \mathbf{R}_{ev} may then be separated into \mathbf{R}_e , which is the electronic transition moment, and $q_{v'v''}$, which represents the Franck-Condon factor, and takes the form

$$|\langle \Psi'_v | \Psi''_v \rangle|^2$$

and it is called the overlap integral because it is a measure of the degree that the two vibrational wavefunctions overlap. The Franck-Condon principle is shown in Figure 2.6 where a vibronic transition from the ground vibrational state to an excited vibronic state is indicated by the vertical line.

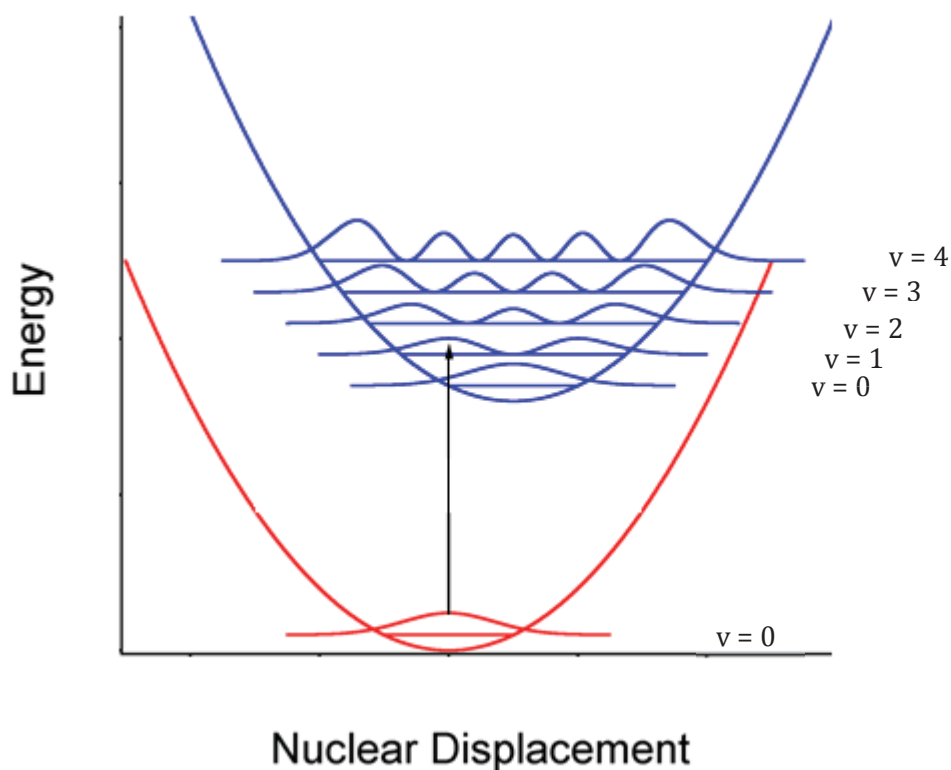


Figure 2.6 – An illustration of the Franck-Condon principle by showing the overlap of vibrational wavefunctions. In this example the $v = 0$ wavefunction best overlaps with the $v = 1$ wavefunction in the excited state.

A simpler way of describing the Franck-Condon factor is to say that it is a measure of how well the vibronic states, between which a transition occurs, are overlapped based on the difference in the internuclear bond distance and the shape of the potential. This is because there may be a significant difference in the equilibrium bond length when comparing the upper excited state to the lower ground state. If the difference is significant it may have a large impact on the resulting spectral intensities [7].

2.12 – Magnetic Hyperfine Structure of Diatomic Molecules

The previously discussed Hund's case pictures are further modified in situations where a molecule contains a nucleus with a non-zero nuclear spin, such as in the case of rhenium. This non-zero nuclear spin brings in the possibility of hyperfine effects, which can result from the nuclear spin, \mathbf{I} , coupling with one or more of the angular momenta within the molecule. In the case of coupling with the orbital angular momentum, the energy is given as

$$H_{II} = \frac{2\mu_0\mu_I}{I r^3} \mathbf{I} \cdot \mathbf{I}$$

where μ_0 is the Bohr magneton, μ_I is the nuclear magnetic moment, \mathbf{I} is the nuclear spin, r is the distance between the electron and the nucleus, and \mathbf{I} is the orbital angular momentum of an electron with respect to the nucleus [2]. In order to determine the actual energy resulting from this, the expression must be averaged over all the electrons contributing to the total orbital angular momentum \mathbf{L} . The average value of \mathbf{L} is expressed as $\mathbf{k}\Lambda$, where \mathbf{k} is a unit vector along the internuclear axis, and Λ is the component of \mathbf{L} along this direction as usual. Therefore, when more than one electron is involved, the energy is given by

$$H_{IL} = \frac{2\mu_0\mu_I}{I} \sum_n \left(\frac{1}{r_n^3} \right)_{av} \Lambda_n \mathbf{I} \cdot \mathbf{k}$$

where the sum is over all electrons contributing to the hyperfine structure, and Λ_n is the average projection of the orbital angular momentum of the n th electron on the internuclear axis.

The case in which the nuclear magnetic moment and an electron spin moment interact is somewhat more complicated. In this case, the interaction between the two dipoles μ_1 and μ_2 of the form

$$W_{\mu_1\mu_2} = \frac{\mu_1 \cdot \mu_2}{r^3} - \frac{3(\mu_1 \cdot r)(\mu_2 \cdot r)}{r^5}$$

becomes

$$(H_{IS})_1 = \frac{-2\mu_0\mu_I}{I} \left[\frac{\mathbf{I} \cdot \mathbf{S}}{r^3} - \frac{3(\mathbf{I} \cdot \mathbf{r})(\mathbf{S} \cdot \mathbf{r})}{r^5} \right]$$

where $(\mu_1 = \frac{\mu_I}{I} \mathbf{I})$ is for the nucleus and $(\mu_2 = -2\mu_0 \mathbf{S})$ for the electron spin. There is also an additional interaction between a nuclear magnetic moment and the sigma electrons in molecules [2]. This can be written approximately as

$$(H_{IS})_2 = \frac{16\pi}{3} \frac{\mu_0\mu_I}{I} \psi^2(0) \mathbf{I} \cdot \mathbf{S}$$

For the common Hund's a and b cases, these three magnetic interactions are summed for a linear molecule as

$$H^1 = a\mathbf{I} \cdot \mathbf{k} + b\mathbf{I} \cdot \mathbf{S} + c(\mathbf{I} \cdot \mathbf{k})(\mathbf{S} \cdot \mathbf{k})$$

where

$$a = \frac{2\mu_0\mu_I}{I} \left(\frac{1}{r^3} \right)_{av}$$

$$b = \frac{2\mu_0\mu_I}{I} \left[\frac{8\pi}{3} \psi^2(0) - \frac{3\cos^2\theta - 1}{2r^3} \right]_{av}$$

$$c = \frac{3\mu_0\mu_I}{I} \left(\frac{3\cos^2\theta - 1}{r^3} \right)_{av}$$

where θ is the angle between the internuclear axis and the vector r from the nucleus to the electron. The constants a , b , and c are referred to as hyperfine parameters. This expression is only applied to the unpaired electrons in the system, as the paired electrons, which have opposite spin, will cancel each other out.

This hyperfine coupling leads to a modification of the Hund's coupling cases (a) and (b). The nuclear spin is able to add to different angular momenta in the molecular system leading to the Hund's cases a_α , a_β , and Hund's cases $b_{\beta J}$, $b_{\beta S}$, and $b_{\beta N}$ [2]. The α indicates that the nuclear spin is most strongly coupled to the molecular axis, the β subscript indicates that the nuclear spin is coupled to a vector other than the molecular axis, and the J, S, and N indicate that the nuclear spin is coupled to \mathbf{J} , \mathbf{S} , or \mathbf{N} respectively. It is extremely unlikely for the nuclear spin to couple along the molecular axis in case b because the electron spin is not coupled

along the molecular axis in case b. Case $b_{\beta J}$ is the most common case to occur and this is the case considered most relevant to the ground state of rhenium carbide.

In Hund's case (a), as in the excited state of rhenium carbide, the previous expression for H^1 becomes

$$H^1 = [a\Lambda + (b + c)\Sigma]\mathbf{I} \cdot \mathbf{k}$$

because $\mathbf{S} \cdot \mathbf{k} = \Sigma$, and $\mathbf{I} \cdot \mathbf{S} = (\mathbf{I} \cdot \mathbf{k})(\mathbf{S} \cdot \mathbf{k})$ when \mathbf{S} precesses about the molecular axis \mathbf{k} . The hyperfine energy for case a_α is given as the sum of a magnetic interaction and a term which depends on the molecular moment of inertia. The effect of Ω_I , or the projection of I on the internuclear axis, $\mathbf{I} \cdot \mathbf{k}$, is given by

$$W = [a\Lambda + (b + c)\Sigma]\Omega_I - hB[\Omega_I + 2(\Lambda + \Sigma)]\Omega_I$$

where Ω_I has the possible values of $I, I - 1, \dots, -I$. The remainder of the expression is a constant for a given electronic energy level. In the case of a_β this becomes

$$W = [a\Lambda + (b + c)\Sigma]\frac{\Omega}{J(J + 1)}\mathbf{I} \cdot \mathbf{J}$$

where $\Omega = \Lambda + \Sigma = \mathbf{J} \cdot \mathbf{k}$, and

$$\mathbf{I} \cdot \mathbf{J} = \frac{F(F + 1) - J(J + 1) - I(I + 1)}{2}$$

In this case, the hyperfine structure becomes less prominent at higher J values, due to I becoming closer to being perpendicular to the intermolecular axis [2].

In case $b_{\beta J}$, the initial picture of the angular momenta and the projections on the internuclear axis remains the same as in figure 2.3, except that now the nuclear spin, \mathbf{I} , is coupled to the total angular momentum, \mathbf{J} , to give a new total angular momentum \mathbf{F} . Therefore, $b_{\beta J}$ coupling can be described by

$$\mathbf{R} + \mathbf{L} = \mathbf{N}$$

$$\mathbf{N} + \mathbf{S} = \mathbf{J}$$

$$\mathbf{J} + \mathbf{I} = \mathbf{F}$$

where the new vector diagram is shown in Figure 2.7.

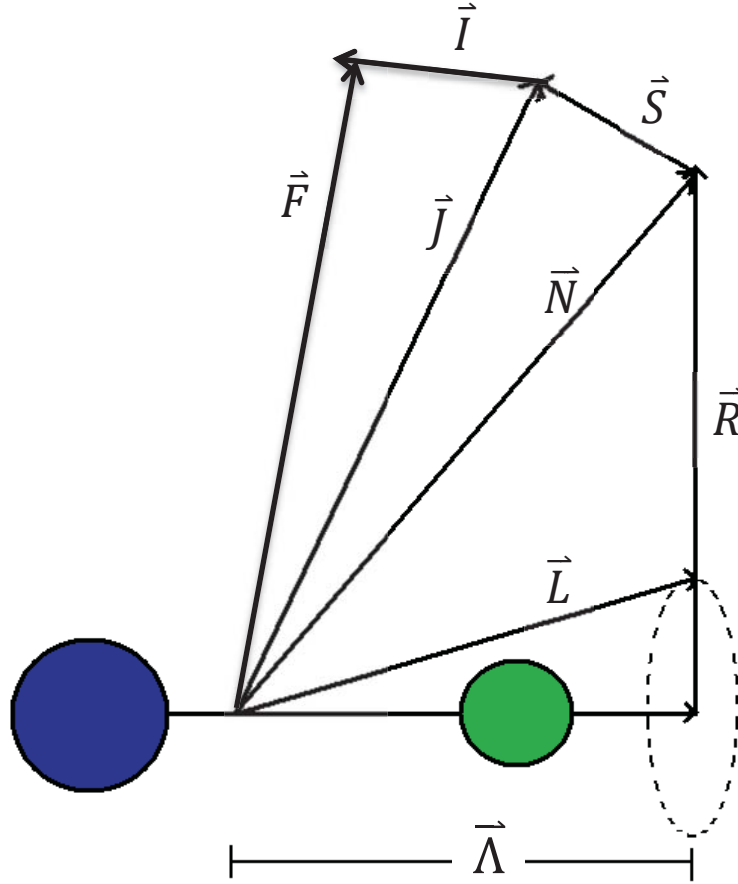


Figure 2.7 – Vector diagram of Hund's case ($b_{\beta J}$) coupling scheme.

The expected energies to arise from case $b_{\beta J}$ are as follows [2]:

When $S = \frac{1}{2}$:

$$W_{J=N+\frac{1}{2}} = \left[\frac{2a\Lambda^2}{(N+1)(2N+1)} + \frac{b}{2N+1} + \frac{c}{(2N+1)(2N+3)} \left(1 + \frac{2\Lambda^2}{N+1} \right) \right] \mathbf{I} \cdot \mathbf{J}$$

$$W_{J=N-\frac{1}{2}} = \left[\frac{2a\Lambda^2}{N(2N+1)} - \frac{b}{2N+1} + \frac{c}{(2N-1)(2N+1)} \left(1 - \frac{2\Lambda^2}{N} \right) \right] \mathbf{I} \cdot \mathbf{J}$$

When $S = 1$:

$$W_{J=N+1} = \left[\frac{a\Lambda^2}{(N+1)^2} + \frac{b}{(N+1)} + \frac{c}{(N+1)(2N+3)} \left(1 + \frac{2\Lambda^2}{N+1} \right) \right] \mathbf{I} \cdot \mathbf{J}$$

$$W_{J=N} = \left[\frac{a\Lambda^2(N^2 + N - 1)}{N^2(N + 1)^2} + \frac{b}{N(N + 1)} + \frac{c}{N(N + 1)} \left(1 - \frac{2\Lambda^2}{N(N + 1)} \right) \right] \mathbf{I} \cdot \mathbf{J}$$

$$W_{J=N-1} = \left[\frac{a\Lambda^2}{N^2} - \frac{b}{N} + \frac{c}{N(2N - 1)} \left(1 - \frac{2\Lambda^2}{N} \right) \right] \mathbf{I} \cdot \mathbf{J}$$

where $\mathbf{I} \cdot \mathbf{J} = \frac{1}{2} [F(F + 1) - J(J + 1) - I(I + 1)]$

Deviations from the above pure coupling cases are possible and to be expected, and there is the possibility of intermediate coupling cases occurring. There is also the possibility of N not remaining a “good” quantum number in all situations, such as when the coupling constant values get rather large. Second order effects may also further alter the above picture.

2.13 – Parity

If the symmetry operator \hat{E}^* is used on the total Hamiltonian, including electric, vibrational, and rotational parts, then total (+/-) parity is obtained [3]. The \hat{E}^* operator inverts all of the coordinates of the particles around the center of mass such that

$$\hat{E}^* \Psi(X_i, Y_i, Z_i) = \Psi(-X_i, -Y_i, -Z_i) = \pm \Psi(X_i, Y_i, Z_i)$$

where X , Y , and Z describe the coordinates of the particles. The \hat{E}^* symmetry operator divides all of the rovibronic energy states into two groups using the expression

$$\hat{E}^* \Psi = \hat{E}^* (\Psi_{el} \Psi_{vib} \Psi_{rot}) = \pm \Psi$$

All rovibronic energy levels in which the upper sign applies have positive (+) total parity, while all of the rovibronic energy levels in which the lower sign applies have negative (-) total parity.

When \pm signs are written as superscripts on the term symbols, Σ^+ and Σ^- , they correspond to

$$\hat{\sigma}_v |\Sigma^\pm\rangle = \pm |\Sigma^\pm\rangle$$

where $\hat{\sigma}_v$ is an ordinary point group operation of reflection in the symmetry plane of the diatomic molecule [3]. The superscript \pm sign in the term symbol for Σ states indicates the effect of $\hat{\sigma}_v$ on only the orbital part of the electronic wavefunction. The effects of total parity are given for the case of $^4\Sigma$ states in Figure 2.8.

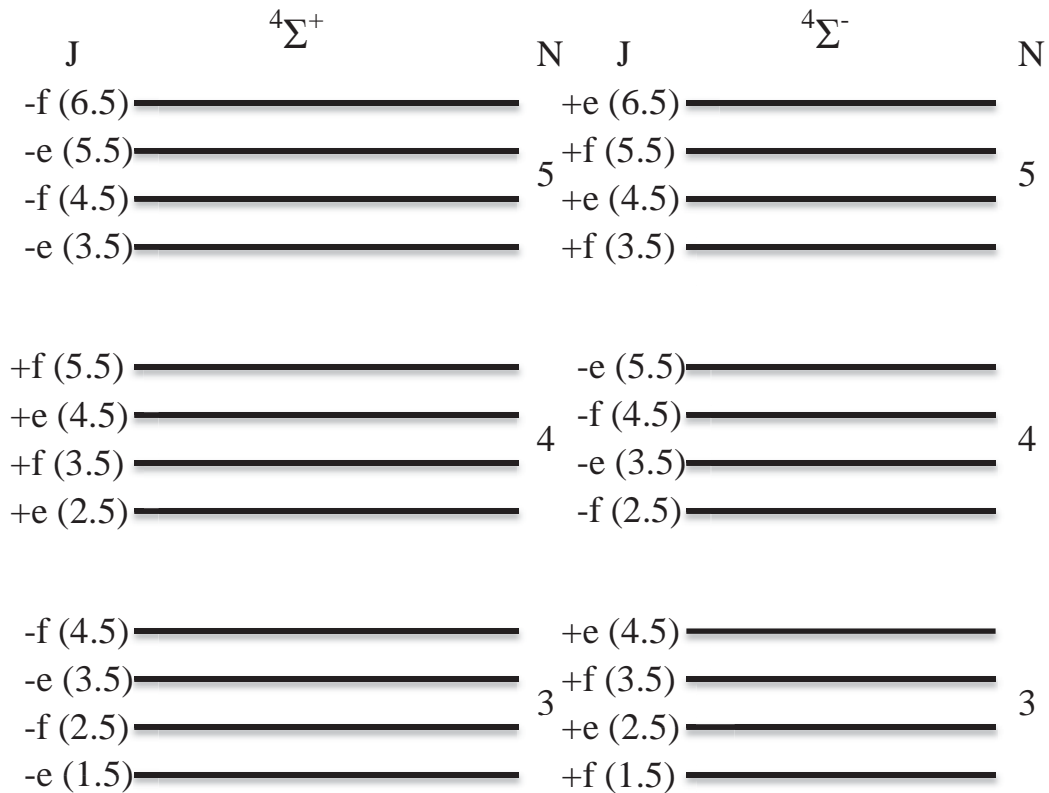


Figure 2.8 – Parity of ${}^4\Sigma$ rotational energy levels

The total parity sign changes with J because of a phase factor $(-1)^J$. The alternation of sign with J is always present, so it is useful to define a new parity, e and f , as

$$\hat{E}^* \Psi = + (-1)^J \Psi \quad \text{for } e$$

$$\hat{E}^* \Psi = - (-1)^J \Psi \quad \text{for } f$$

for integer J , and where Ψ is the total rovibronic wavefunction. e and f parity is similar in cases with half integers values of J , but the exponent is $J - \frac{1}{2}$. An example is given for the case of the ${}^4\Pi_{3/2}$ spin-orbit component of a ${}^4\Pi$ state in Figure 2.9.

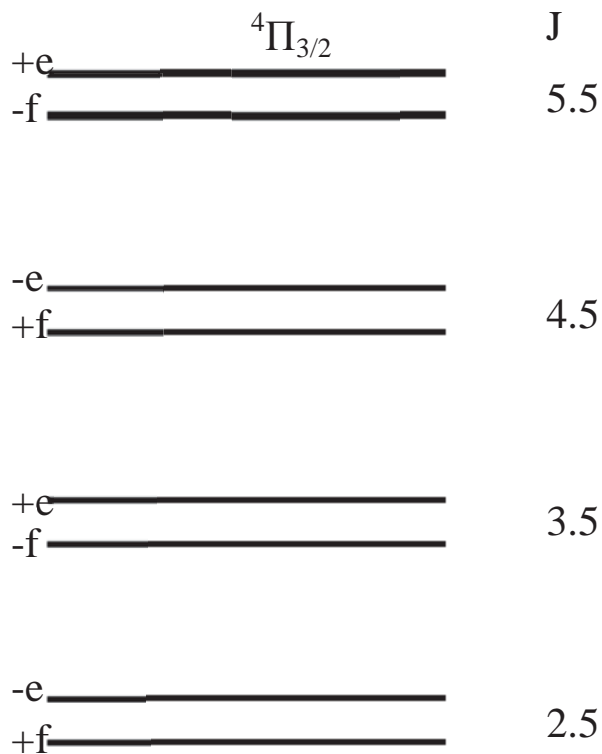


Figure 2.9 – Parity of ${}^4\Pi_{3/2}$ rotational energy levels

In Figure 2.9 the pairs of levels sharing the same J value are degenerate unless interactions between molecular rotation and electronic orbital angular momentum, and between electron orbital and electron spin momenta separate them. This separation appears as a splitting of lines in the spectrum, and is referred to as lambda-type doubling.

2.14 – Isotope Effect

The isotope effect is of importance in this thesis because rhenium has two isotopes with high relative natural abundance, ^{185}Re has an abundance of 37.4% and ^{187}Re has an abundance of 62.6%. Each isotopologue of ReC will have its own unique spectrum of lines with different frequencies because each isotopologue has a different mass. Both the vibrational energy, $G(v)$, and the rotational energy, $F(J)$, depend on the reduced mass, μ , which means that the energies will be different for each isotopologue. The relationship between the two different masses is defined as

$$\rho = \sqrt{\frac{\mu}{\mu^*}}$$

such that $\rho \leq 1$, where μ^* is the reduced mass for the heavier isotopologue. Using this relationship, the relationships for the vibrational and rotational constants can be written as

$$\frac{\omega^*}{\omega} = \sqrt{\frac{\mu}{\mu^*}} = \rho$$

$$\frac{B^*}{B} = \frac{\mu}{\mu^*} = \rho^2$$

respectively [5]. The electronic energy remains the same for each isotopologue, which means that the bond strength, k , and the bond length, r , remain unchanged because they depend on electronic properties.

The relationships for the vibrational and rotational constants can be incorporated into the energy expressions, which then give the energy levels for the heavier isotopologue. The vibrational and rotational energy levels are given by

$$\begin{aligned}
 G(v)^* &= \omega_e^* \left(v + \frac{1}{2}\right) - \omega_e x_e^* \left(v + \frac{1}{2}\right)^2 \\
 &= \rho \omega_e \left(v + \frac{1}{2}\right) - \rho^2 \omega_e x_e \left(v + \frac{1}{2}\right)^2 \\
 F(J)^* &= B^* J(J + 1) - D^* [J(J + 1)]^2 \\
 &= \rho^2 B J(J + 1) - \rho^4 D [J(J + 1)]^2
 \end{aligned}$$

respectively [9]. The vibrational isotope separation can also be determined by using

$$\begin{aligned}
 \Delta E_v &= \Delta G(v) - \Delta G(v)^* \\
 &= (1 - \rho) \left[\omega_e' \left(v' + \frac{1}{2}\right) - \omega_e'' \left(v'' + \frac{1}{2}\right) \right]
 \end{aligned}$$

which gives the difference in the band origins of the two isotopologues.

2.15 – Dispersed Fluorescence

Dispersed fluorescence is a technique in which a lower state is excited into an upper state, and then the upper state fluoresces back down to various lower energy levels, including levels in the ground state; a monochromator is used to monitor the fluorescence with some resolution that allows the individual vibronic (or in some cases rovibronic) transitions to be observed. This is illustrated in Figure 2.10. Observation of the vibrational transitions allows for the determination of

vibrational spacing. This technique is also useful in determining whether the correct molecule is being analysed if the vibrational frequency is known.

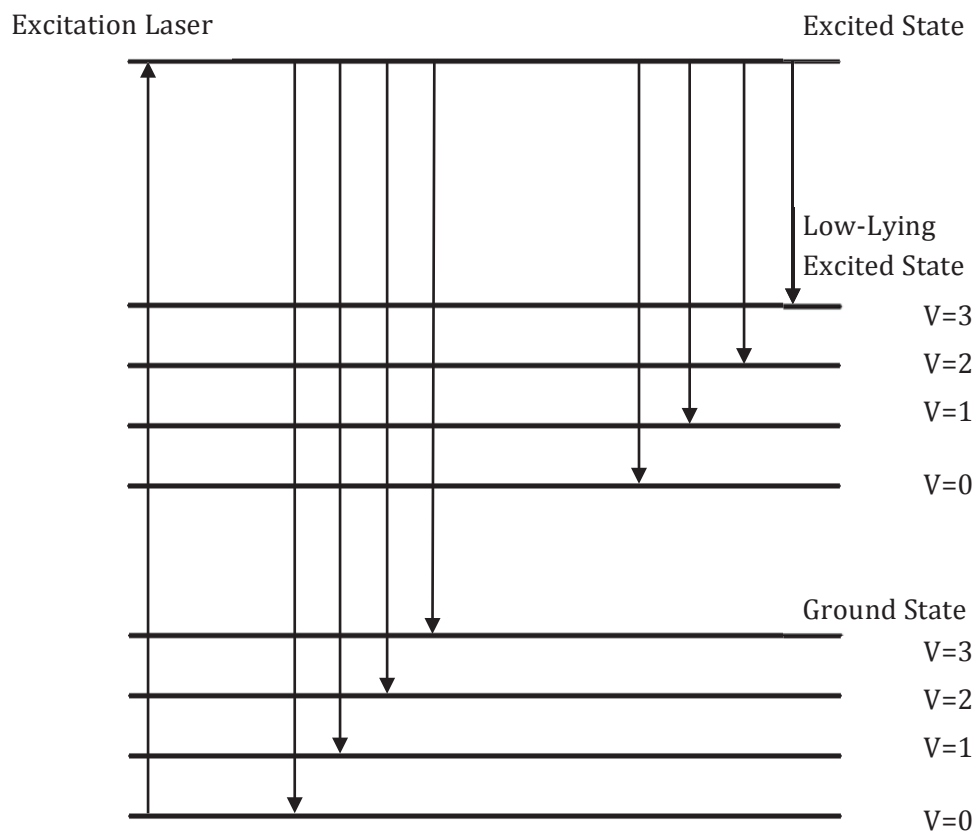


Figure 2.10 – Dispersed fluorescence diagram showing fluorescence from an excited state down to various energy levels in a low-lying excited state and the ground state.

References

1. Banwell, C.N., Fundamentals of Molecular Spectroscopy. New York: McGraw-Hill Publishing Co., 1966
2. Townes, C.H., Schawlow, A.L., Microwave Spectroscopy. New York: McGraw-Hill, Inc., 1955
3. Bernath, P.F., Spectra of Atoms and Molecules. New York: Oxford University Press, Inc., 1995
4. Hollas, J.M., High Resolution Spectroscopy. London: Butterworth & Co Ltd., 1982
5. Herzberg, W.S., Molecular Spectra and Molecular Structure Vol.1, Spectra of Diatomic Molecules, Second Edition. Princeton: Van Nostrand Reinhold Co., 1950
6. Brugh, D.J., Morse, M.D., *J. Chem. Phys.* **117**, 10703-10714 (2002)
7. Hollas, J.M. Modern Spectroscopy. Chichester: John Wiley & Sons Ltd., 1987
8. Steinfield, J.I. Laser Coherence Spectroscopy. New York: Plenum Publishing Corp., 1978
9. Downie, L., *High Resolution Laser Spectroscopy of Iridium Monofluoride*. BSc Honours Thesis, Department of Chemistry, University of New Brunswick (2008)

Chapter 3

Experimental Setup

3.0 – The Ablation Source

This chapter will outline the overall laser ablation experimental apparatus as well as the individual procedures used for data collection in various experiments. The key experimental procedures to be outlined are: low-resolution survey scans, dispersed fluorescence spectra, lifetime measurements, as well as high-resolution scans. Figure 3.1 summarises the main components of the general experimental setup required for the experiments.

The ablation source may also be referred to as a supersonic expansion molecular jet apparatus, due to the molecular jet, or beam, produced by the newly formed molecules inside the reaction chamber, as explained in section 3.2. The reaction chamber is kept under a vacuum of approximately 5×10^{-6} Torr (or $\sim 7 \times 10^{-9}$ atm) before introduction of the ligand precursor gas, and the vacuum is achieved by making use of a diffusion pump and a turbo pump, each backed by a rotary vane mechanical pump. The operating pressure rises to approximately 5×10^{-5} Torr once the gas is being injected into the chamber. Operating at this low vacuum pressure significantly reduces the number of collisions between the ReC molecules produced in the jet and background molecules in the vacuum chamber; collisions which would

impede the forward translational motion of the ReC molecules and produce sideways velocity components in the jet. Therefore all of the ReC molecules essentially move straight down through the chamber.

Another benefit of this low background pressure is the supersonic expansion that occurs as a result of the difference between the pressure in the vacuum chamber and the pressure of the precursor gas as it is pulsed in. The precursor gas is pulsed in at a pressure of approximately 3 atm, into a chamber held at approximately 7×10^{-9} atm. This large difference in pressures causes the introduced gas to immediately start expanding at a supersonic rate into the chamber. This supersonic expansion, which converts random room temperature motion into forward translational movement through collisions, also causes the molecules to be rotationally very cold, at temperatures of approximately 50 kelvin. These collisions also quench vibrational energy. As a result, the cold molecules have fewer energy levels populated. Therefore only absorptions occur from the electronic ground state, usually out of the lowest vibrational level, and from a couple of tens of rotational levels. This works well for a high-resolution spectral analysis, because with fewer levels populated, the spectrum is much less complex and congested than it would otherwise appear with many more levels populated. Another important benefit of limited collisions is that it allows for unstable radicals, such as ReC, to exist for longer periods of time, which enables us to detect them before they cease to exist.

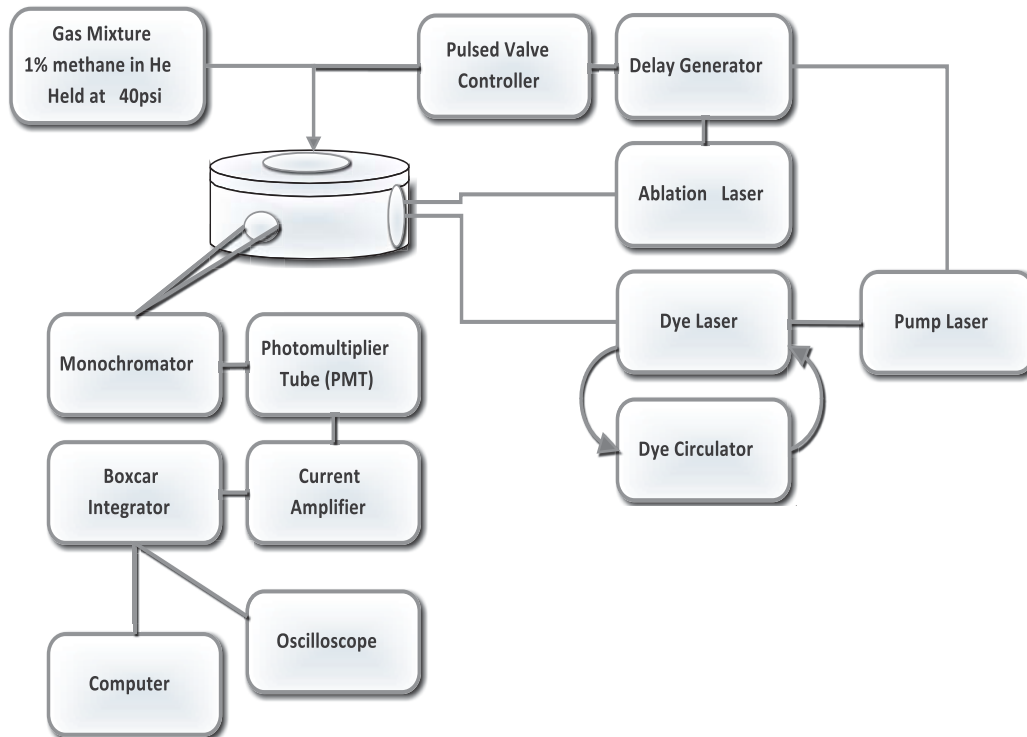


Figure 3.1 – Experimental setup of the laser ablation apparatus showing the precursor gas introduction, laser systems, and signal/data collection equipment.

3.1 – Preparation of the Precursor Gas Mixture

Before experimentation may begin, the appropriate gas precursor mixture must be produced. For the formation of ReC, the precursor is methane gas (CH_4), which is inert and inexpensive. A carrier gas is required to create a supersonic expansion with the required forward velocity, but also with minimal off-axis velocity components. The mixture has been previously optimized as a 1% mixture of methane in helium [1]. This sample gas mixture is made by using the gas board setup shown in Figure 3.2.

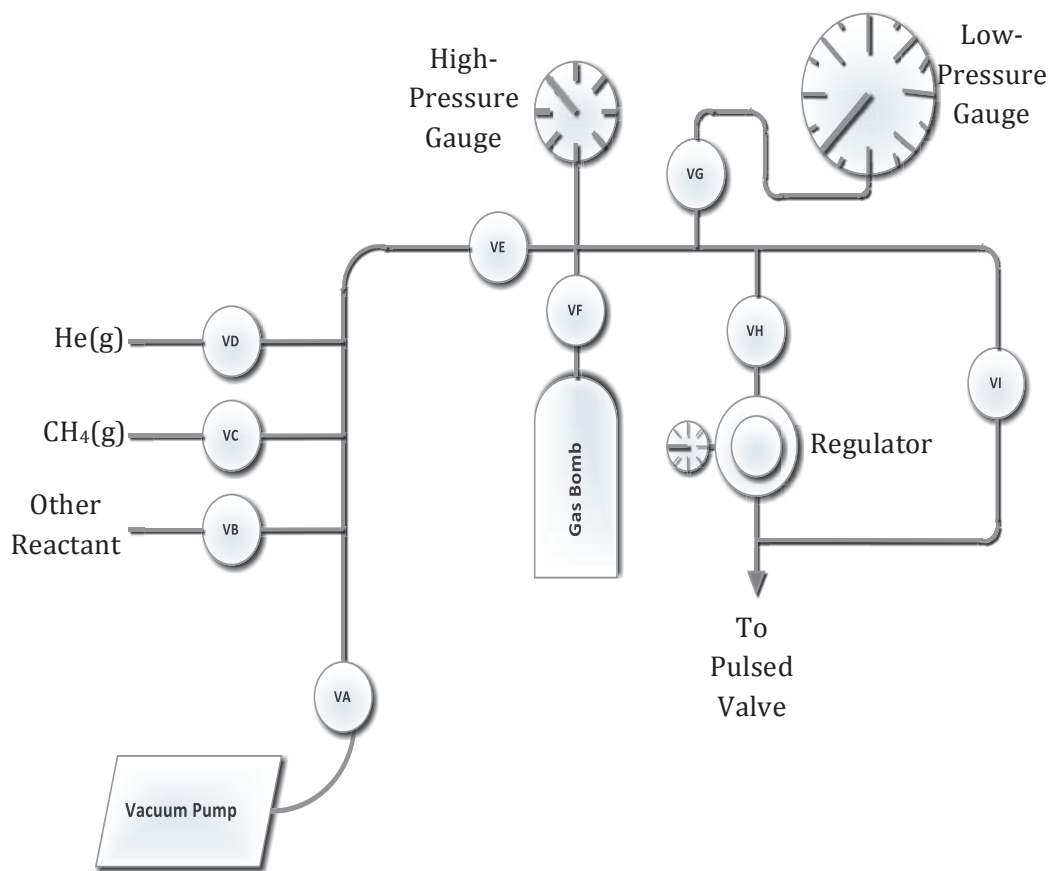


Figure 3.2 – Setup of gas board used to create sample gas mixture. V's represent valves.

The gas board must first be evacuated using a vacuum pump before the appropriate gas mixture can be added for experimentation. Everything must be evacuated including the gas bomb, the tubing to the pulsed valve, and the tubing to the individual gas cylinders. After the gas board is evacuated completely and the valve to the pump, VA, closed, the methane gas is added through its valve (VC) while making sure that the valves (VH, VI) connecting the gas board to the reaction chamber are closed. Methane gas is added up to a pressure of 1.5 psi, as measured using the low-pressure gauge through valve VG. The methane valve VC is then

closed along with valve VG. The helium gas valve VD is then opened, and helium is added to the gas bomb until a pressure of 150 psi is reached, as measured with a high-pressure gauge. To ensure that the gas is properly mixed, it is left to settle for 10-15 minutes before sending the mixture to the reaction chamber through valve VH, after which a regulator (set to a constant pressure of 40 psi -- about 3 atm) controls the gas pressure delivered to the pulsed valve. The pulsed valve adds the gas mixture into the reaction chamber in a controlled and consistent way using short pulses at a set constant rate.

3.2 – The Rhenium Rod and Formation of Rhenium Monocarbide

Before experimentation can begin, ReC molecules must be formed. The methane gas is introduced as described in the previous section. The rhenium atoms are produced by the use of a solid 1/4-inch diameter rhenium metal rod, but the rhenium is not reactive in this form. A laser pulse of high energy must ablate the rhenium rod in order to produce reactive excited atoms of rhenium. The source of ablation in our experiment is a focused beam of UV radiation from a Lumonics HY400 Nd:YAG (neodymium-doped yttrium aluminum garnet; $\text{Nd:Y}_3\text{Al}_5\text{O}_{12}$) laser, which strikes the rhenium rod vaporizing rhenium atoms from the surface of the rod. The methane/helium gas mixture is being introduced into the source at the same time as the ablation process, and the methane molecules are broken into fragments when they interact with the hot metal atoms as they pass over the exposed/ablated portion of the rhenium metal rod. One possible fragment resulting from the break up of methane molecules is a carbon atom. ReC is then formed by the collision between

the hot rhenium atoms and the carbon fragments. The whole ablation/collision process takes place in a stainless steel housing attached to the front end of the pulsed gas valve. The housing controls how the precursor gas comes into contact with the rhenium rod, as well as how much of the rod is exposed to the laser, and how the ablation laser hits the rhenium rod. This setup is shown in figure 3.3. In order for consistent vaporization of hot rhenium atoms, the rhenium rod is attached to the shaft of a translation/rotation stepping motor called a Motor Mike. This motor causes both translation of the rod in both directions as well as constant rotation as shown in Figure 3.3 A. This is necessary to prevent the ablation laser from burning a hole in one spot on the rod, and causes the laser to ablate the rod's surface as evenly as possible. Finally, after the ReC molecules have been formed, the molecules are swept along with the carrier helium/methane gas mixture and expand into the chamber by being channelled out through the bottom of the housing through the small hole as seen in Figure 3.3 B. The expansion into the vacuum chamber causes the formation of the molecular beam, as previously described.

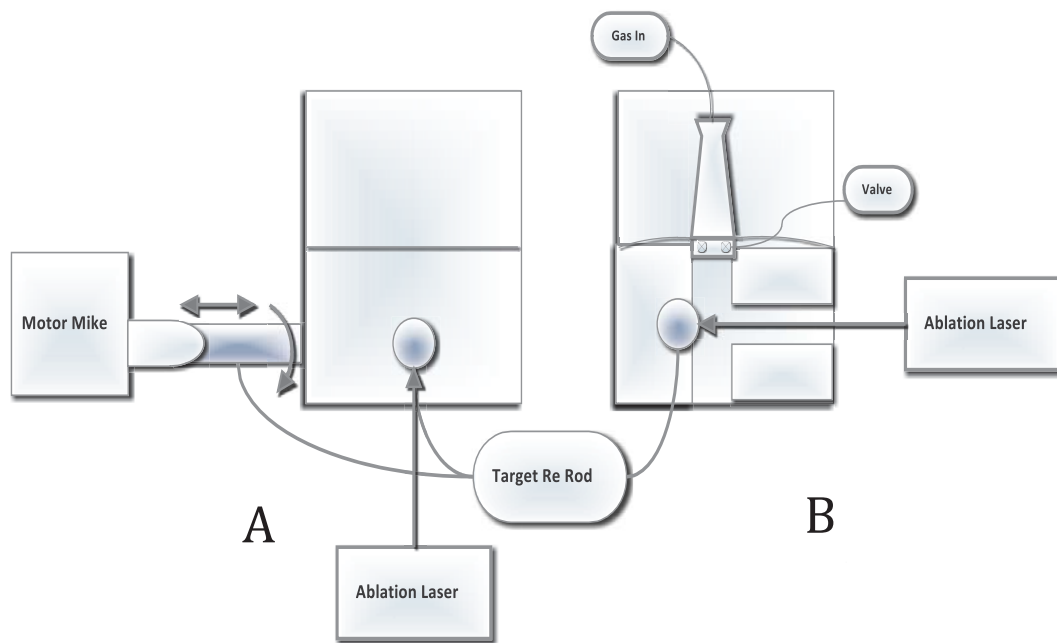


Figure 3.3 – Diagram of the stainless steel rhenium rod housing as seen (A) parallel, and (B) perpendicular to the ablation laser.

3.3 – Electronic Components

As mentioned previously, a Lumonics HY400 Nd:YAG laser was used for ablation of the rhenium metal rod for production of excited rhenium atoms. The HY400 produces UV light with a wavelength of 355 nm for a duration of 10 ns at a rate of 10 Hz. Tunable dye lasers were utilized to probe the molecular beam approximately 5 cm from the source orifice inside the vacuum chamber in order to obtain spectroscopic data. For low-resolution work a Lumonics HD500 pulsed dye laser was used, which was pumped by a Lumonics YM600 Nd:YAG laser. For high-resolution work a continuous wave (CW) Coherent CR699-29 ring laser was used, which was pumped by a Coherent Sabre Inova R25 argon ion laser.

The laser-induced excitation of a molecular transition causes laser-induced fluorescence (LIF), which is measured using a 0.25 m Jarrell Ash monochromator that has a bandwidth of ± 15 nm to filter out any background radiation. Attached to the output side of the monochromator is a thermoelectrically cooled Hamatsu R943-02 photomultiplier tube (PMT), which detects the fluorescent signal and converts it into a small current. This weak current must be put through a current amplifier (Keithley model 428) to amplify the current so that it is usable. This amplified signal is directed into a boxcar integrator, triggered by the same delay generator used to trigger the rest of the lasers and equipment, which averages the signal over a chosen time constant to produce functional data. The time constant used is usually 3 or 10 seconds in our experiments. The output of the current amplifier is sent to an oscilloscope to be displayed for observation and for use when optimizing the desired signal. The output of the boxcar integrator is also sent through an A/D converter to convert the data to a digital signal that can be read on a computer for low-resolution work, or an Autoscan A/D collection system for high-resolution work.

3.4 – Optimization

There are various components of the experimental setup that can be carefully adjusted to maximize the LIF signal from ReC. It had been previously established that the optimized gas mixture is 1.5 psi of CH₄ in 150 psi of He [1]. A delay generator (Stanford Research Systems, DG535), set at a rate of 10 Hz, is used to optimize the timing between the ablation laser and the injection of the gas pulse. This delay takes into account the time it takes for the injected gas to travel from the

valve nozzle to the rod, approximately 500 μ s. The timing of the pulsed dye laser was optimized at approximately 103 μ s, found by adjusting the timing while sitting the laser wavelength on top of a strong LIF feature in the spectrum.

The alignment of the equipment must be adjusted to maximize the signal produced. The pump laser must be properly aligned with respect to the dye laser to maximize the strength of the beam leaving the dye laser. Steering mirrors are also used to direct the laser beam into the reaction chamber. The mirrors must be adjusted so that the UV ablation beam is properly hitting the Rhenium rod in order to create a consistent source of rhenium atoms for molecule formation. This alignment is confirmed by the appearance of a stable plume of plasma exiting the stainless steel housing. The mirrors must also be adjusted to ensure that the beam from the dye laser is properly passing through the center of the reaction chamber. The monochromator must be flush with the reaction chamber, and the PMT must similarly be flush with the monochromator. The monochromator and the PMT can be slightly moved in different directions to maximize the signal produced. The oscilloscope, which displays a strong LIF feature, is used to monitor the effect of adjusting the various aspects of the experimental setup.

3.5 – Experimental Techniques

Vibronic transitions were located by performing a broad low-resolution scan from 415 – 535 nm. The dye in the pulsed dye laser is excited by the output of the pump Nd:YAG laser, which is being directed into the pulsed dye laser. A variety of dyes were used because each dye is only useful for a small given range of

wavelengths. A list of pulsed laser dyes used and their useful wavelength ranges is given in Table 3.1. When performing the scans, the dye laser is scanned through a range of 10 nm while the monochromator is fixed at a value in the middle of the scanned range. The range is scanned at a rate of 0.0125 nm/step while the LIF is being detected. The PMT is adjusted to an optimized voltage and multiplied by 10^6 V/A with the Keithley amplifier. The time constant, τ , for these scans was set to 3 s. After scanning the desired range, several intense bands of interest were seen. No slits were used in the monochromator so the bandpass of the monochromator was the maximum ± 15 nm.

Table 3.1 – List of pulsed laser dyes used, and the frequencies at which they are the most useful.

Dye	Maximum of Dye (nm)	Useful Range of Dye (nm)
S420	420	415-455
C440	435	422-459
C450	452	436-467
LD466	465	446-500
C480	477	458-507
C500	504	481-550

Vibrational intervals were determined using a technique called dispersed fluorescence (DF), which is also useful for the detection of low-lying electronic states. With the dye laser fixed at a particular LIF transition frequency, the monochromator is scanned over a range of about 400 nm at a rate of 0.1 nm/step.

This technique is used to detect the fluorescence from the excited state back to ground state vibrational levels, or to vibrational levels in a low-lying electronic state. When performing a DF scan, the PMT is adjusted to an optimized voltage and multiplied by 10^7 V/A with the Keithley amplifier. The time constant for these scans is 10 s. 500 μm slits are placed on entrance and exit of the monochromator in order to reduce the bandwidth from ± 15 nm to ± 0.5 nm.

High-resolution spectra were also taken to resolve rotational structure for bands of interest. Rather than using a pulsed dye laser, a CW ring dye laser was used in conjunction with an argon ion laser. The dye used for the scan must have a useful range, which includes the band of interest. The laser dyes used to cover the range from 415 nm to 520 nm were s420 and c480, which were dissolved in ethylene glycol. The useful ranges are 400-470 nm and 465-506 nm for s420 and c480 respectively, with max lasing wavelengths of 449 nm and 490 nm. The dye laser output power was between 200 and 290 mW on average. The spectra were collected in 30 GHz, or 1 cm^{-1} , segments at a rate of 10 GHz/300 s. The boxcar time constant typically used was 3 s, but was changed to 10 s for scans with larger amounts of noise and the laser was scanned more slowly.

The lifetimes of ReC excited states were determined by sending the LIF signal from the PMT to a digital oscilloscope instead of the Keithley amplifier. The voltage of the LIF signal was averaged and plotted against time on the oscilloscope. The data gave an exponential decay that could be fit to extract the lifetime of the excited state.

References

1. Weale, R., *High Resolution Laser Spectroscopy of Rhenium Carbide*. BSc Honours Thesis, Department of Chemistry, University of New Brunswick (2012)

Chapter 4

Spectral Results and Analysis

4.0 – Low-Resolution Survey

A low-resolution survey scan of ReC was obtained over a range from 415 – 535 nm, and several rovibronic bands were found. A representative low-resolution spectrum is shown in Figure 4.1. Five bands have been labelled within the spectrum, which correspond to the bands that have been scanned using high-resolution techniques. The four bands ranging from 426 to 462nm are the bands that are extensively analyzed in this thesis, whereas the band at 500nm has not been analyzed at this time. The former four bands are considered to be the four spin orbit components of a $^4\Pi$ excited state due to the similarity in band structure between the four bands, and due to the calculations performed by Dr. Grein, which predict transitions between quartet states to be present. This was, however, only based on predictions and speculation before high-resolution spectra were taken to get a more detailed picture of the structure within these bands. For the full low-resolution spectrum, see Appendix A.

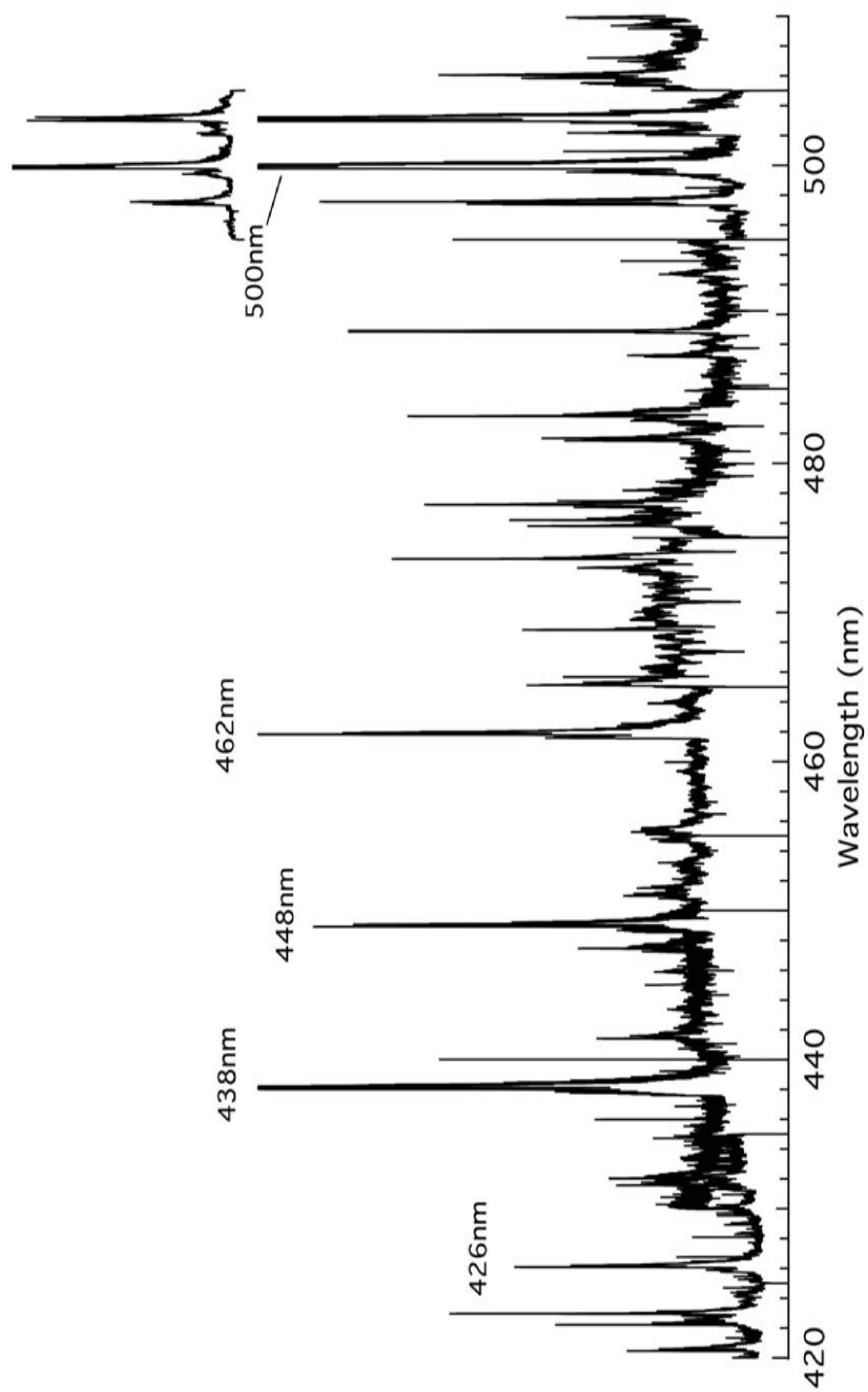


Figure 4.1 – Low resolution survey scan of ReC with a 1% CH₄ reactant gas mixture

4.1 – Dispersed Fluorescence Analysis

Dispersed fluorescence spectra were taken for thirteen observed transitions, and these assisted in confirming that the molecule being studied was ReC. This was done by comparing the vibrational spacing of ReC with known carbides, oxides, nitrides, and chlorides [1]. This assists confirmation of ReC production because different ligand types, such as carbides and chlorides, produce characteristic vibrational frequencies. A carbide molecule, therefore, would produce a different vibrational frequency than a chloride molecule, and this can be clearly observed in a dispersed fluorescence spectrum. Some of the peaks present in the dispersed fluorescence spectra were in the exact same location in all of the spectra, which is indicative of the presence Re atomic lines. A line was placed through these peaks in each spectrum in order to readily identify peaks specific to ReC. A representative DF spectrum of ReC is given in Figure 4.2. The complete set of DF spectra can be found in appendix B.

It should be noted that during DF analysis, there were peaks present, other than the ones representing the ground state vibrational progression. These extra lines indicate the presence of a low-lying excited state. The low-lying excited state peaks in the DF occur when the molecule is excited to the upper state, and fluorescence down to the low-lying excited state occurs rather than back to the ground state. This results in a vibrational progression for the low-lying excited state, which has a different vibrational frequency of its own.

Once the transition frequencies were determined, they were fit to the equation

$$G(v', v'') = T_e + \omega_e'(v' + \frac{1}{2}) - \omega_e x_e'(v' + \frac{1}{2})^2 - \omega_e''(v'' + \frac{1}{2}) + \omega_e x_e''(v'' + \frac{1}{2})^2$$

where $v'' = 0$ for the ground state. The determined values of the parameters are given in Table 4.1.

Table 4.1 – Vibrational parameters for the ground and low-lying excited states, as determined by fitting the DF data.

Parameters	Ground State (cm ⁻¹)	Excited State (cm ⁻¹)
T_e	0	1128.1 ± 0.2
ω_e	1006.17 ± 0.08	990.0 ± 0.7
$\omega_e x_e$	4.49 ± 0.02	5.9 ± 0.2

The obtained vibrational frequency for the ground state compares well with the theoretical frequency of 1046 cm⁻¹ as predicted in literature[9]. The determined vibrational frequency is of an appropriate value for diatomic transition metal monocarbides, which may be seen when compared to other studied carbides from literature such as NiC[10], PdC[11], MoC[11], and RuC[11]. These carbides have vibrational frequencies of 875.1, 847.6, 1008.3, and 1100.0 cm⁻¹ respectively, and the fact that our value falls in this range gives further confirmation that we have made the carbide as opposed to some other diatomic.

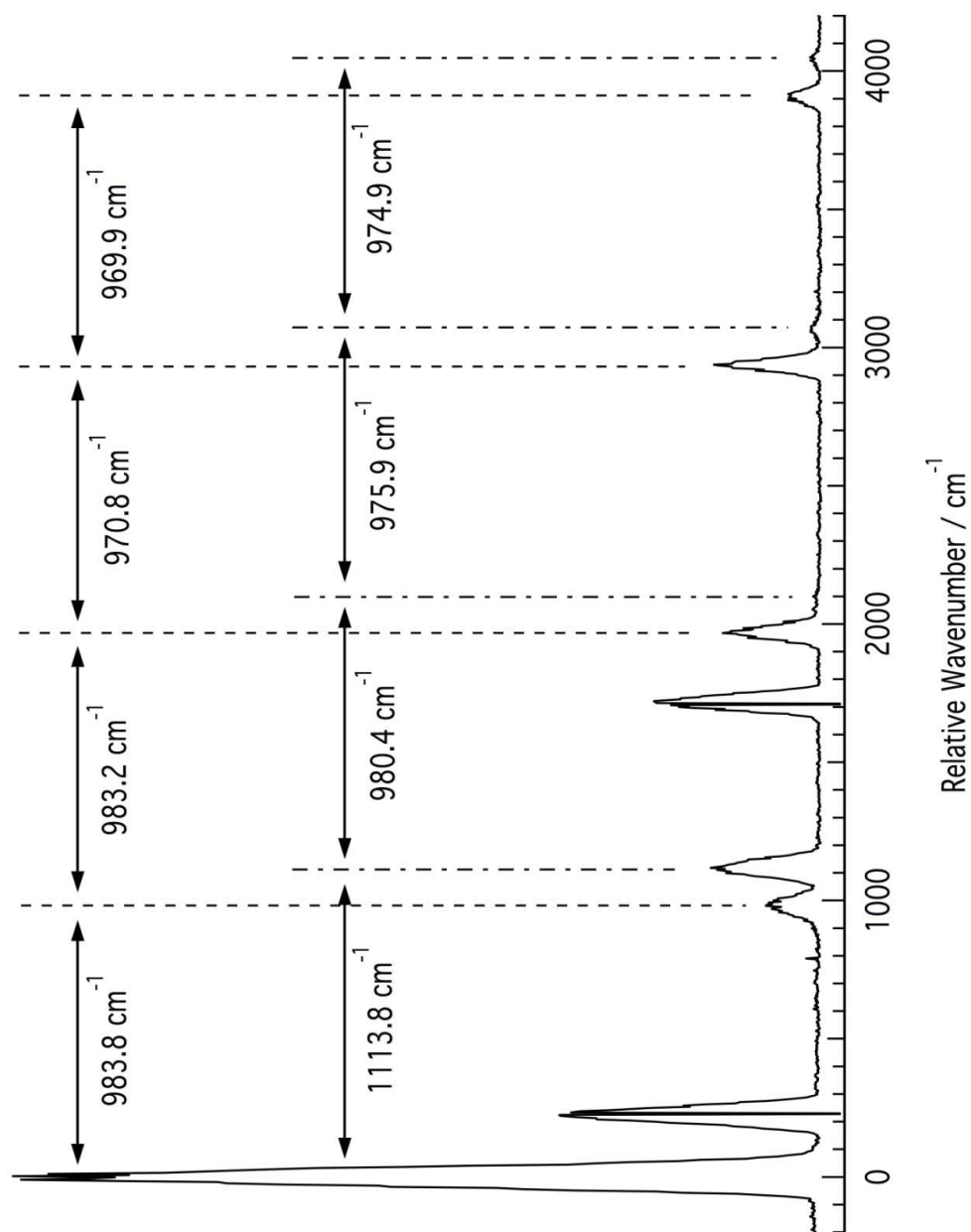


Figure 4.2 – Dispersed fluorescence spectrum of ReC, where the frequencies are measured relative to the excited transition at 20691.40 cm^{-1} .

4.2 – High Resolution Spectral Analysis

One of the first notable observations, once a full band was scanned at high resolution, was the significant congestion of the spectrum. To demonstrate this congestion, the full spectrum of the 438nm band is given in Figure 4.3.

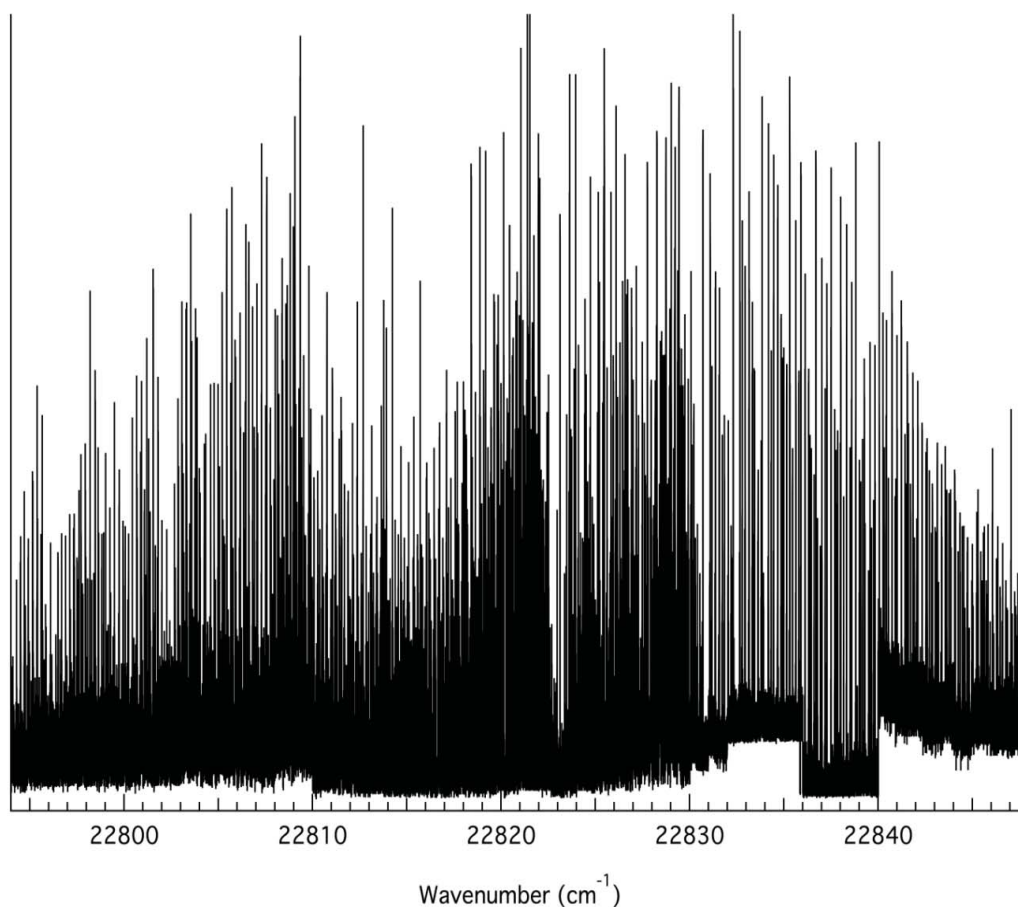


Figure 4.3 – Full spectrum of the 438nm band at high resolution

The spectra were divided into four regions to make analysis of the high resolution spectra more manageable. The first region is from the low frequency side of the band to 22815 cm⁻¹, the second region is from 22815 – 22823 cm⁻¹, the third region is from 22823 – 22831 cm⁻¹, and the fourth region is from 22831 cm⁻¹

onwards to higher frequency. Dividing the spectrum into four regions is useful later on when trying to determine which R, P, or Q branches correspond to each other. For example, the assigned P branch in region one is not the same P branch that exists in region two.

It can be noted, in the high resolution spectra, that the four bands observed at high resolution generally have very similar structures, but the 438 and 448 nm bands have better signal-to-noise than the 426 and 462 nm bands. The 438 and 448 nm bands will be primarily discussed in the remainder of this chapter, but the other two bands were analyzed in the same way.

Based on the calculations performed by Dr. Friedrich Grein, the predicted electronic transition is from a $^4\Sigma^-$ ground state to a $^4\Pi$ excited state [2]. Looking at all possible rotational transitions, there should be three branches present in each region of the spectrum. This is demonstrated in Figure 4.4.

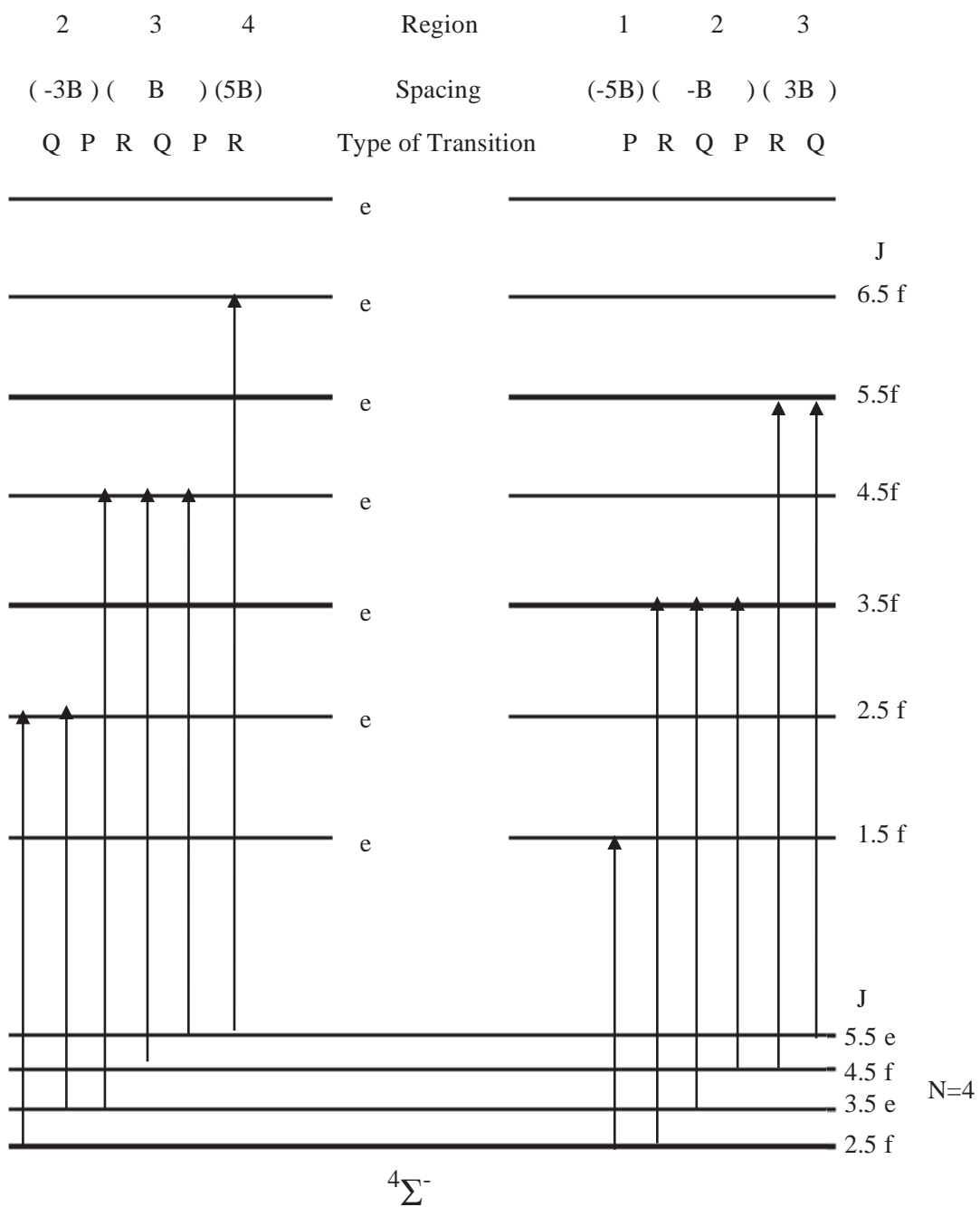


Figure 4.4 – Diagram of transitions from a single rotational level in the $4\Sigma^-$ ground state to all allowed levels of the upper 4Π excited state for a single spin orbit component.

Figure 4.4 summarizes the types of transitions allowed from a $^4\Sigma^-$ state to a single $^4\Pi$ state spin orbit component. Each type of transition has a label indicating the spacing between peaks in that type of branch, as well as a label indicating which region of the spectrum that type of transition occurs in. The negative sign that is present on some of the spacing estimates indicates that that branch will be heading towards lower wavenumber as J increases. If looking at region four, for example, the diagram shows we should expect to see only a single R branch within this region with a branch spacing of about $5B$. We can make similar assumptions about other regions in the spectrum with different numbers and types of branches.

As the high-resolution spectra were recorded, they were processed with a software package called Igor Pro [3]. This program allowed us to plot the data on the computer, as well as allowing us to pick which transitions were to be considered in the analysis and which were going to be considered negligible (too weak/noisy). Another facet of this program, called Loomis-Wood, allowed us to plot all of the picked transitions as points in a two-dimensional array. This allowed us to try to see patterns in the points, where the patterns showed up as a line of transitions. The program also allowed the creation of several series of points and these series were fit to a polynomial to see if the chosen points were indeed part of the series. This tool was especially useful when trying to find the R and P branches in regions four and one respectively. Once one branch was found, it became easier to find the other branches in that region because they tended to be a pattern of lines in the same direction.

Once the patterns in region four were identified using Loomis-Wood, it became obvious that there were many more branches present in region four than were expected. We observed 12 branches in region four instead of the expected 1. This is shown in Figure 4.5.

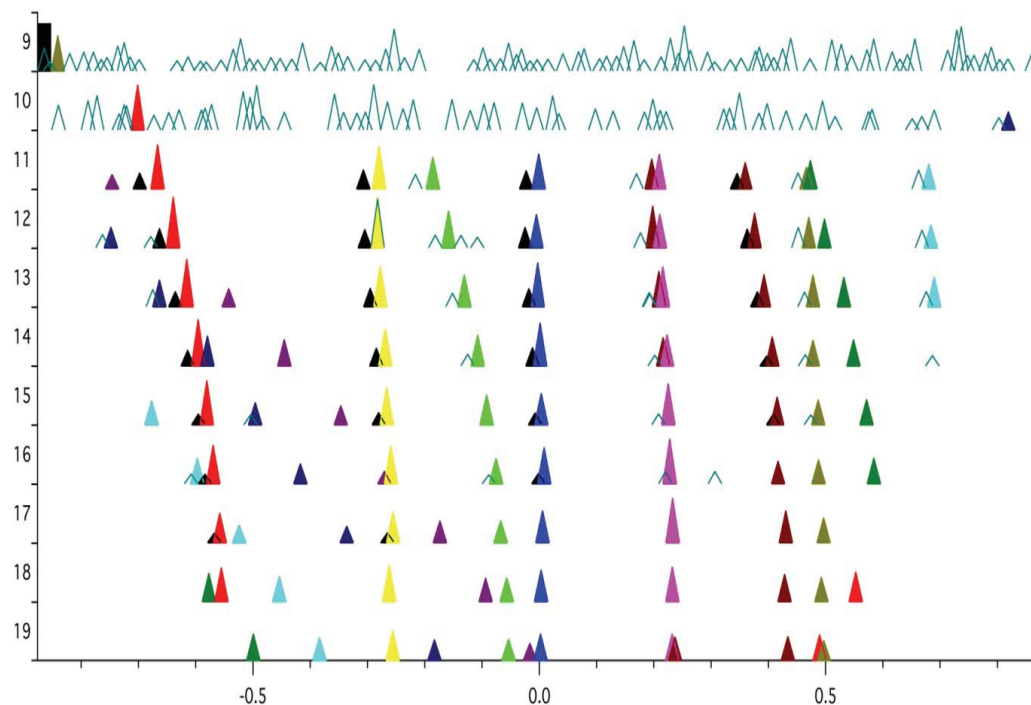


Figure 4.5 – Loomis-Wood plot of selected series in region four of the 438nm band with relative wavenumber on the x-axis, and arbitrary index number on the y-axis.

To determine possible causes of the unexpected number of branches, the high-resolution spectrum was examined in more detail. The easiest region to analyse was region four, because the R branches were most easily identifiable and uncongested. It was noticed that there was a pattern in the intensities and spacing of the R branches in this region. There appeared to be two sets of six peaks, where one set generally had higher intensity than the other set. There was also a pattern of

intensity within each set of six peaks, where the peak with the lowest frequency had the highest intensity and the peak with the highest frequency had the lowest intensity. It should be noted here that there are two isotopes of rhenium with high abundance. The 187 isotope of rhenium has a relative abundance of 62.6%, while the 185 isotope has a relative abundance of 37.4%. It was assumed that the set of six peaks with the higher intensities was due to the ^{187}ReC isotopologue, and the other set of six peaks is from the ^{185}ReC isotopologue. We can also, therefore, state that one of the reasons for more transitions than expected is the presence of both isotopologues of ReC. This isotopologue difference can be observed in Figure 4.6.

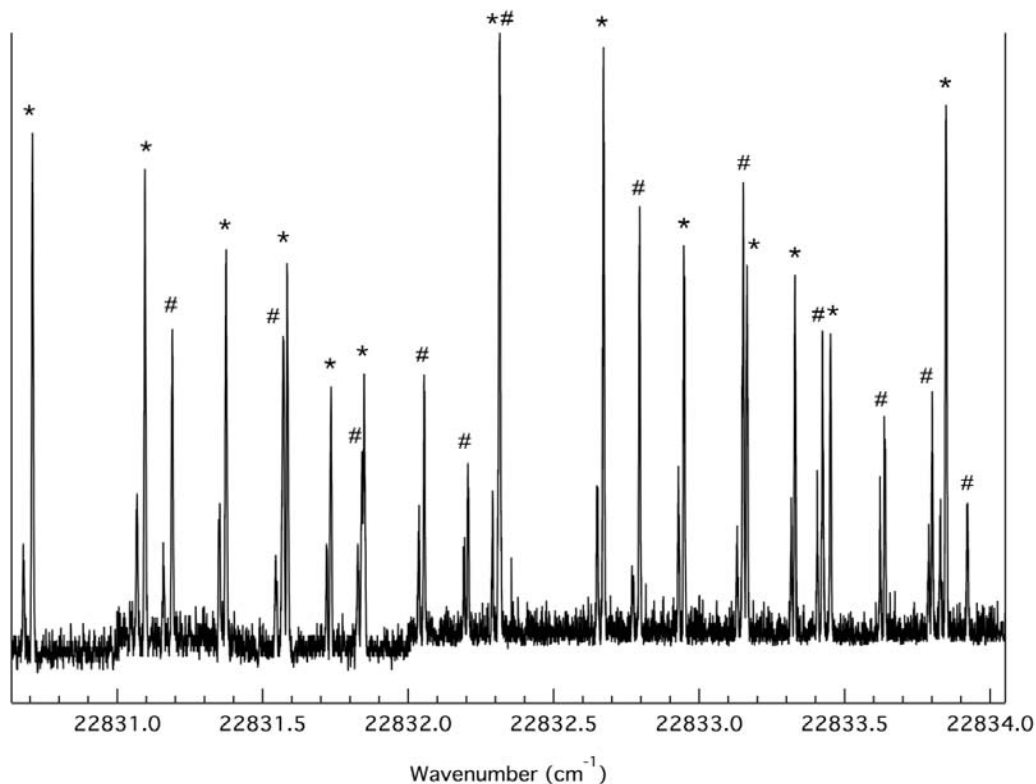


Figure 4.6 – A segment of the R branches from the 438 nm high-resolution band, showing a distinction between the two isotopologues. The ^{187}ReC isotopologue is labelled with *, and the ^{185}ReC isotopologue is labelled with #. Note that there is overlap occurring between the two isotopologues in some places.

The next step was to determine why there was still six times the predicted number of lines present. It was previously mentioned that there was an interesting intensity pattern of six lines present for each isotope in region four. The intensity pattern observed is common for situations where hyperfine splitting is observed [4]. Both the ^{187}Re isotope and the ^{185}Re isotope have a nuclear spin of $I = 5/2$, and each would produce very similar hyperfine splitting patterns, but at slightly different frequencies. There are $2I + 1$ possible orientations of the nuclear angular

momentum, and there will, therefore, be $2I + 1$ components produced in a hyperfine structure with a given I . In our case $2(5/2) + 1$ gives six hyperfine components, which is what is observed in our spectrum. Therefore, there is only a single R branch in region four for each isotopologue, which is being split into its six hyperfine components, and this is exactly what was predicted in Figure 4.4.

This picture is consistent with the predicted $^4\Pi-X^4\Sigma^-$ electronic transition, but the possibility of a $^2\Pi-X^2\Sigma^-$ transition exists. A comparison to a doublet transition can be made by inspecting the overall structure present in each band. The complex structure and the corresponding large number of lines present is more in line with what is expected of a quartet transition than what would be expected of a doublet transition. Figure 4.4 shows that there are twelve branches expected, which we now know are split into six lines for each rotational transition, and then doubled due to the presence of both isotopologues. In a doublet transition, however, we would only expect six branches. This would result in half the current number of lines. This result is demonstrated in Figure 4.7.

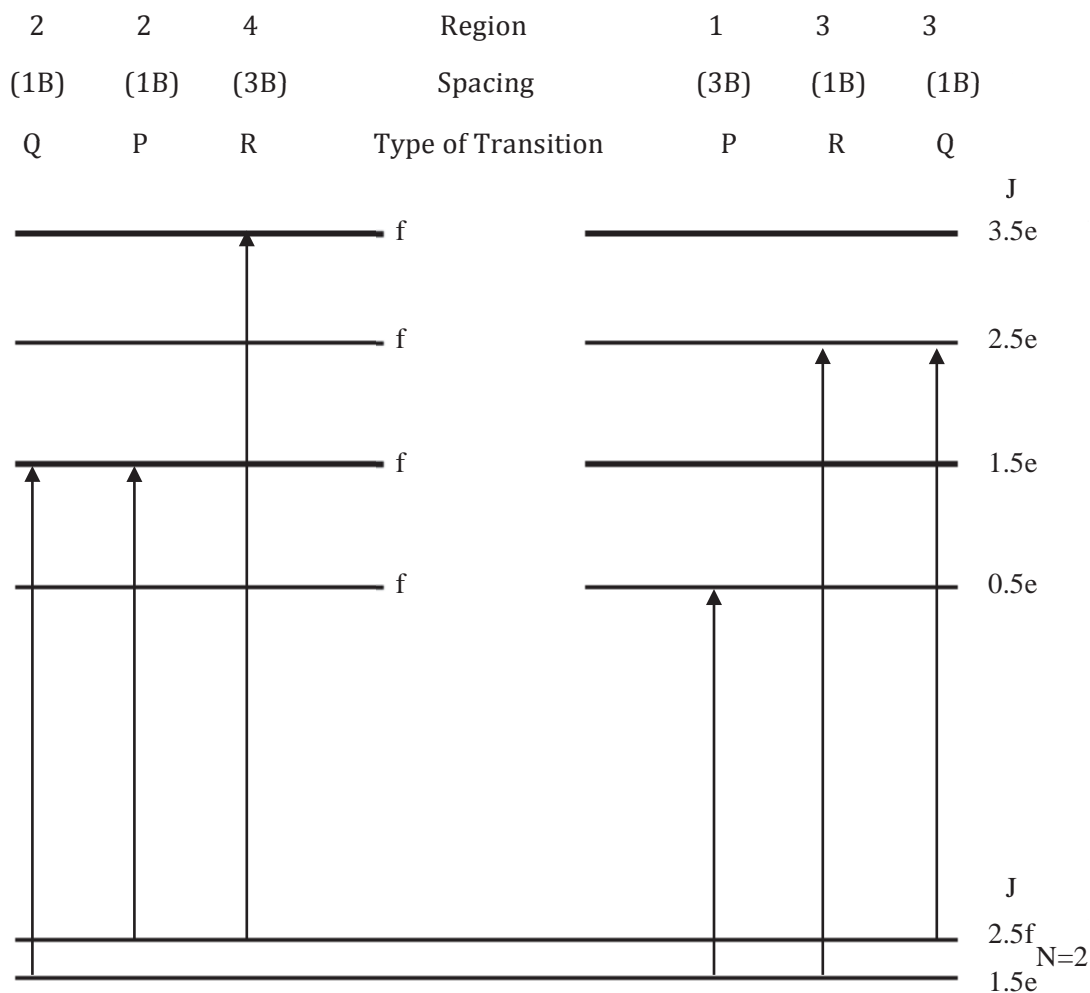


Figure 4.7 – Diagram of transitions from a single rotational level in the $2\Sigma^-$ ground state to all allowed levels of the upper 2Π excited state

The hyperfine structures in the 438nm band were then compared with the hyperfine structures in the 448nm band to see if the splitting pattern had the same spacing between peaks in the pattern. The best way to align the bands was with the use of Igor Pro, which allowed us to plot both high-resolution bands atop one another, and to line up a peak in one band with a peak in the other band. With one of the peaks in both bands being perfectly aligned, we could see if the other peaks in

the hyperfine structure also align. It was found that for a particular hyperfine structure with a given N'' , the different $2I + 1$ hyperfine components were aligned between the two bands. This is shown in Figure 4.8. At this point it should be noted that the shift between the two isotopologues is different between the two bands.

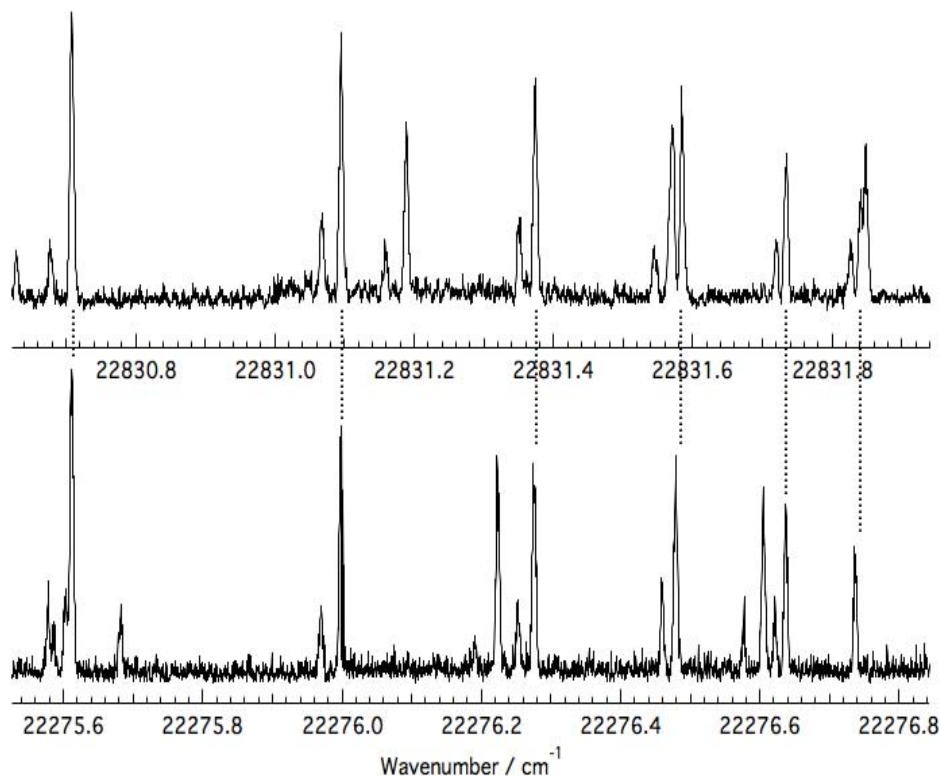


Figure 4.8 – Compared hyperfine structures in the R branch of the 438 and 448 nm bands, where the ^{187}ReC peaks are aligned. The aligned peaks are at 22830.708 cm^{-1} in the 438 nm band, and at 22275.612 cm^{-1} in the 448 nm band.

The spacing between peaks for both bands in the above figure was calculated in order to show the numerical difference between the spacing between both bands. This is given in Table 4.2.

Table 4.2 – Comparison of spacing between the 438 and 448 nm bands, and an absolute difference between the spacing in each

Band	Spacing (cm ⁻¹)				
438 nm	0.387	0.279	0.211	0.150	0.114
448 nm	0.387	0.277	0.204	0.158	0.100
Absolute Difference	0	0.002	0.007	0.008	0.014

The spacing between the rotational hyperfine structures are very similar between bands. When the hyperfine structure in figure 4.8 is lined up between bands, however, the next rotational hyperfine structure is not lined up between the two bands. This can be taken advantage of, because this indicates that while one R branch hyperfine structure is lined up between bands, there should be a corresponding branch hyperfine structure that lines up in another region of the spectrum. After aligning the one specific R branch hyperfine structure in each band, we then found a corresponding hyperfine pattern that was aligned between the two bands in region one. This is shown in Figure 4.9. After finding this we also aligned other R branch hyperfine structures between the two bands, and found other hyperfine structures that corresponded to the aligned R branch each time. Overall, this identified the successive hyperfine structures within a Q branch in region one.

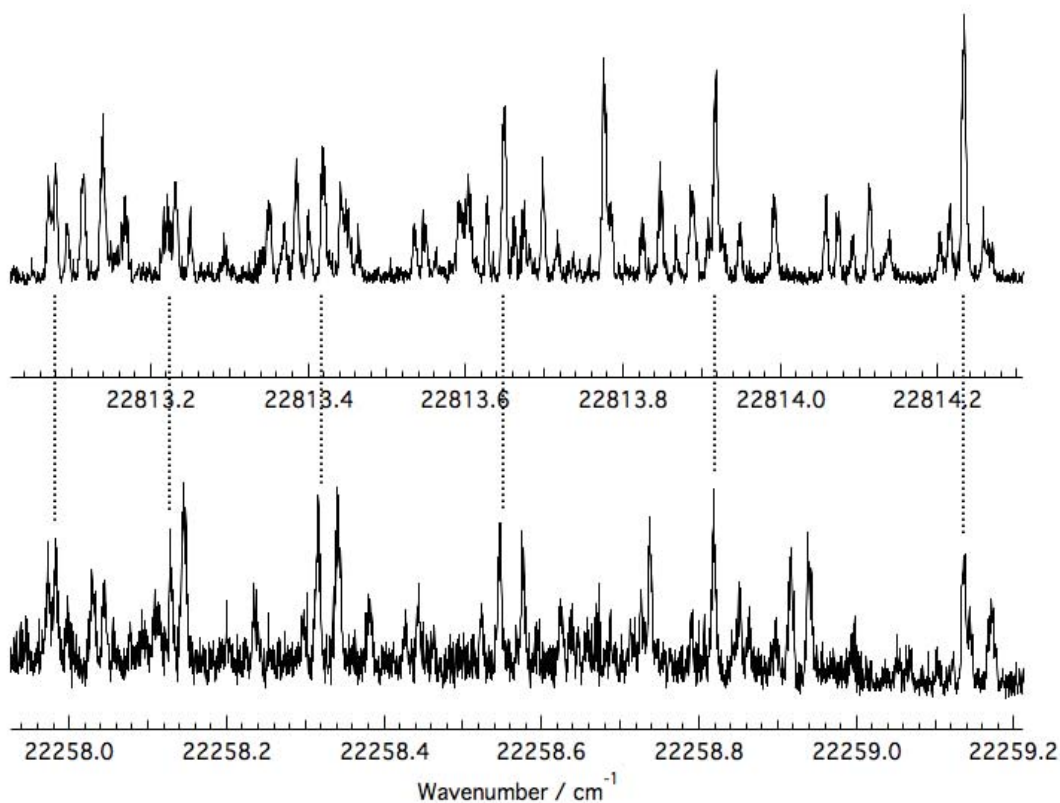


Figure 4.9 – Compared hyperfine structures in the Q branch of the 438 and 448 nm bands.

An R transition is between two specific energy levels, while a Q transition is between two other energy levels. It can be inferred that the upper energy levels of the R and Q transitions are degenerate, because when the R transition is lined up, a corresponding Q transition also lines up. It can also be inferred that the two bands share a common ground state. This can be more easily understood in a diagram illustrating all the possible transitions that may occur from various energy levels in the ground state to a single energy level in the upper excited state. This is illustrated in Figure 4.10.

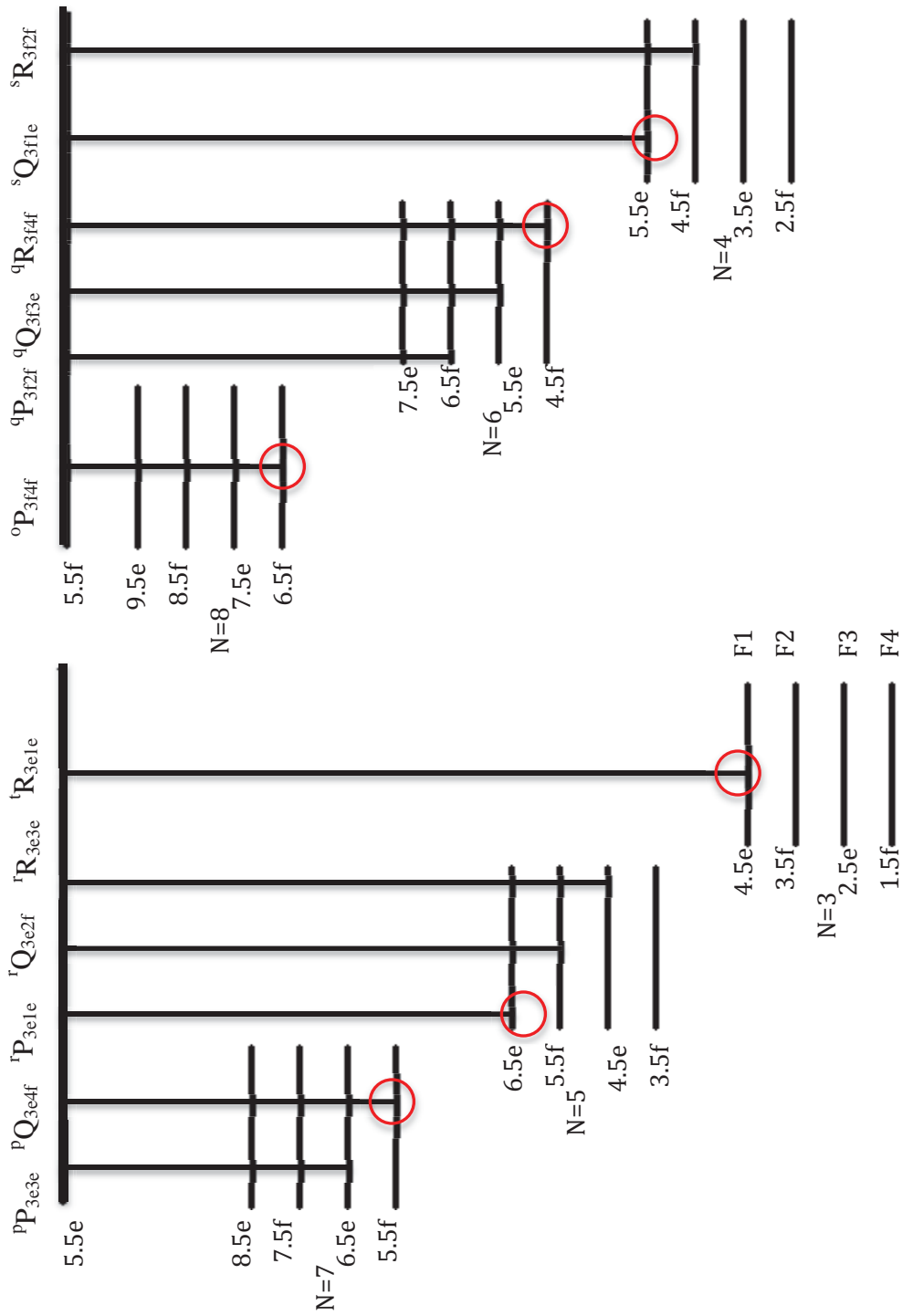


Figure 4.10 – Transition diagram showing all possible transitions from the ground state to a single level in the upper excited state, and identifying which branches have been successfully labelled.

The diagram in Figure 4.10 illustrates the relative energies of the various possible branches within the spectrum, and identifies which branches have been clearly labelled. The diagram also introduces new labelling schemes, which have as yet not been mentioned within this thesis. The various J levels for a given N level in the ground state are labelled with an F-number from 1-4, where F1 identifies the highest J level, and F4 identifies the lowest J level. When identifying which branches have been labelled, a label was placed above the given transition, such as ${}^tR_{3e1e}$, which describes a few aspects of the labelled transition. The large capital letter identifies the change in J, such as a change of +1 for an R branch. The lower-case superscript letter identifies the change in N, such as a change of +3 for a t-type transition. The first number/letter combination in the subscript indicates which spin-orbit component the transition occurs in, and what the parity of the upper excited state is that is involved in the transition. Label 3e, for example, indicates the transition occurred in the 438nm band, and that the upper excited state involved has e parity. The second number/letter combination in the subscript indicates which J level is involved from a certain N level in the ground state, and what parity it has. 1e, for example, indicates that the transition occurs from the F1 level for a given N in the ground state, and that it has e parity.

The previously identified R and Q branches in regions four and one were actually determined to be the ${}^tR_{3e1e}$ and ${}^pQ_{3e4f}$ transitions. Upon further inspection, using a similar method of analysis, an ${}^oP_{3f4f}$ branch was identified. This was an interesting find because the upper excited state involved in this transition has f parity, which is different than the ${}^tR_{3e1e}$ branch that was used to identify it. This

indicates that there is very little, if any, separation between the two parities in the upper excited state, meaning they are essentially degenerate. We were, therefore, able to utilize combination differences as determined from these three branches to assist in identifying more branches, such as those labelled in figure 4.10. An example combination difference is shown in Figure 4.11.

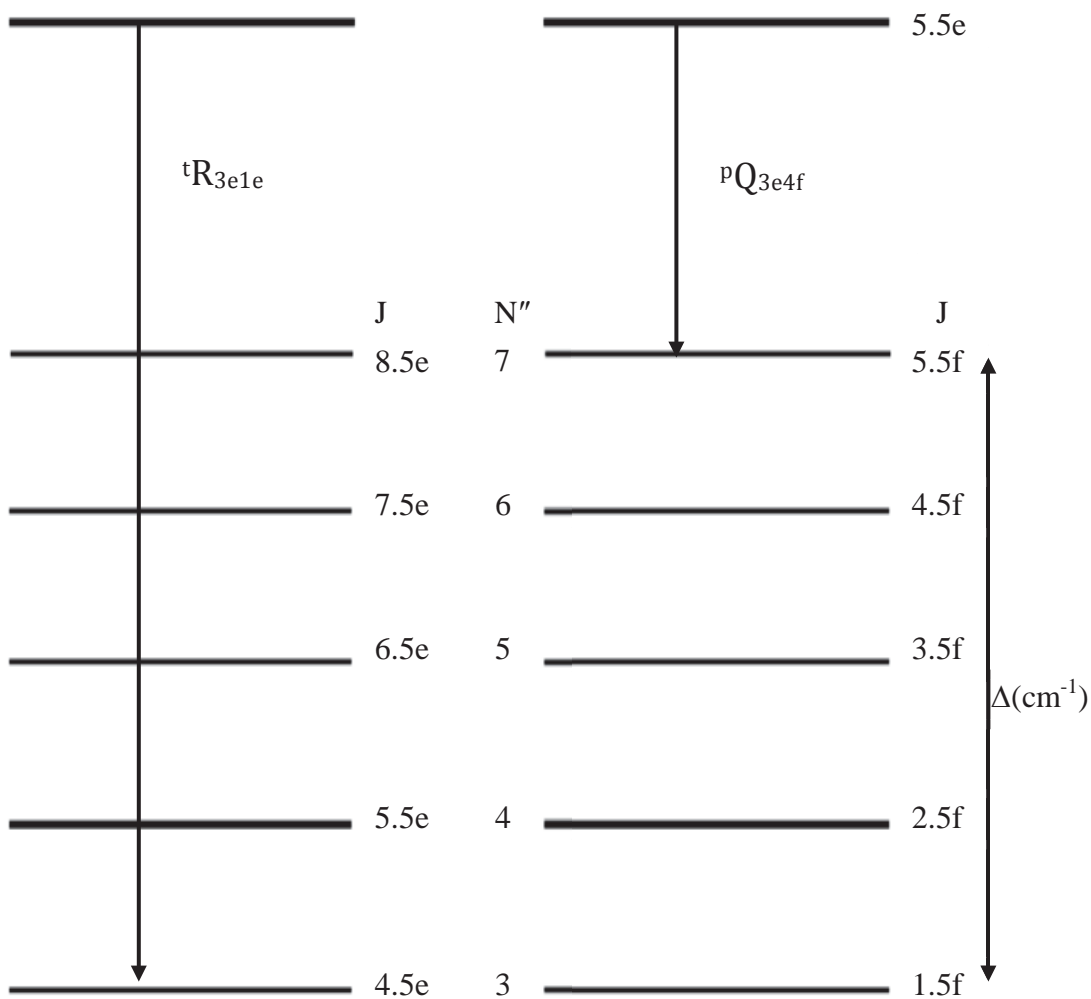


Figure 4.11 – Diagram showing how the R and Q transitions can be used to determine the combination difference between two energy levels in the ground state.

We are able to use the combination differences between corresponding peaks in the ${}^tR_{3e1e}$ and ${}^pQ_{3e4f}$ branches to predict where transitions in other branches should be. For example, once we have the combination differences between the ${}^tR_{3e1e}$ and ${}^pQ_{3e4f}$ branches for one set of transitions, they should be the same as the differences between the ${}^oP_{3f4f}$ and ${}^sQ_{3f1e}$ branches for the same values of N'' . This works because the combination difference is actually between the exact same two energy levels in both cases. This can be seen visually by looking at Figure 4.10. The ${}^oP_{3f4f}$ and ${}^pQ_{3e4f}$ are both on the F4 level within a given N'' , and the ${}^sQ_{3f1e}$ and ${}^tR_{3e1e}$ are both on the F1 level. One major down side to using combination differences is that they require you to have more than just the two branches labelled. You must be able to take the calculated difference and add or subtract it from another branch to find an unidentified branch.

Once we have identified a certain number of branches and peaks within the spectrum for a band, we must come up with appropriate labels for all of the transitions. To assist us in deciding which labels correspond to which transitions, we made use of a program called Pgopher [5]. The program is a line fitting and spectral simulation program, where one is able to input constants for a particular type of transition, and predict a corresponding spectrum. It also allows for the input of spectral data, and once certain peaks are tentatively labelled, it will fit a simulated spectrum to your experimental spectrum. Once it has done this simulation, one may click on any peak in the simulated spectrum and the program identifies its quantum number labels (N, J, F), as well as the parity (e/f) for both the upper excited and lower ground states. The program also identifies which branch a given transition

occurs in, and this is where the labels such as ${}^t\text{R}_{3e1e}$ were decided for our spectrum. It is a trial and error process of labelling a small number of peaks with what is suspected to be their labels, and having the program fit the spectrum, until we arrived at the fit that works best and most accurately fits the whole spectrum. An example of how each transition is labelled is given in Figures 4.12 and 4.13.

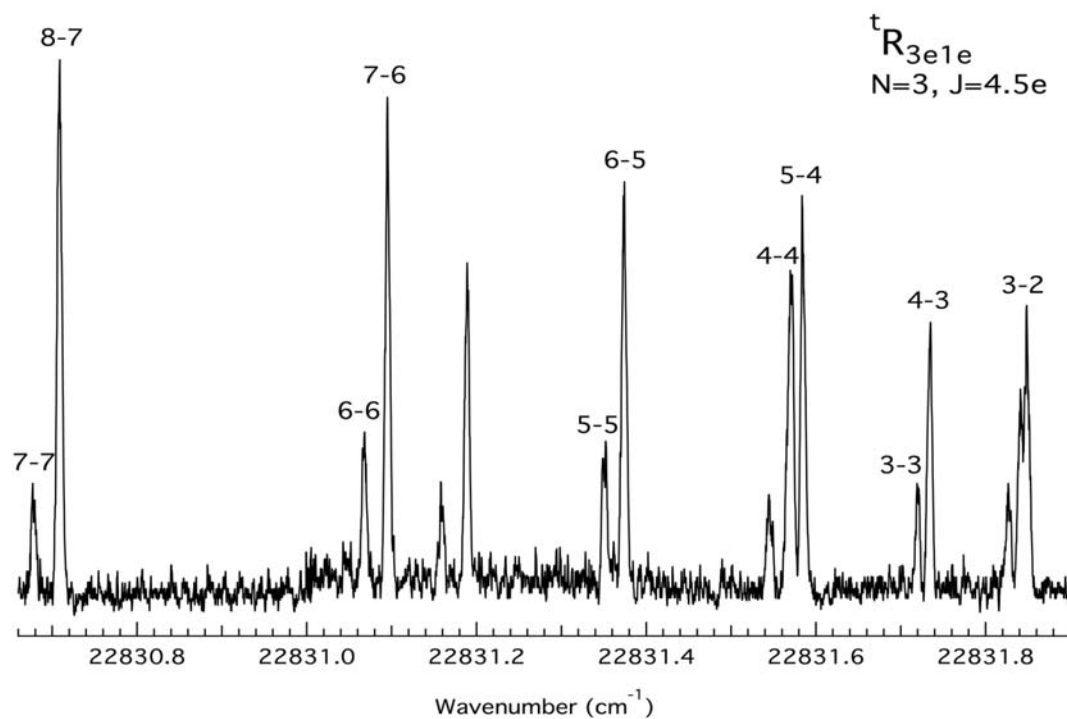


Figure 4.12 – Labelled hyperfine components of the $N'' = 3$ transition of the ${}^t\text{R}_{3e1e}$ branch for the ${}^{187}\text{ReC}$ isotopologue. Each peak is labelled with the upper state F first, followed by the ground state F.

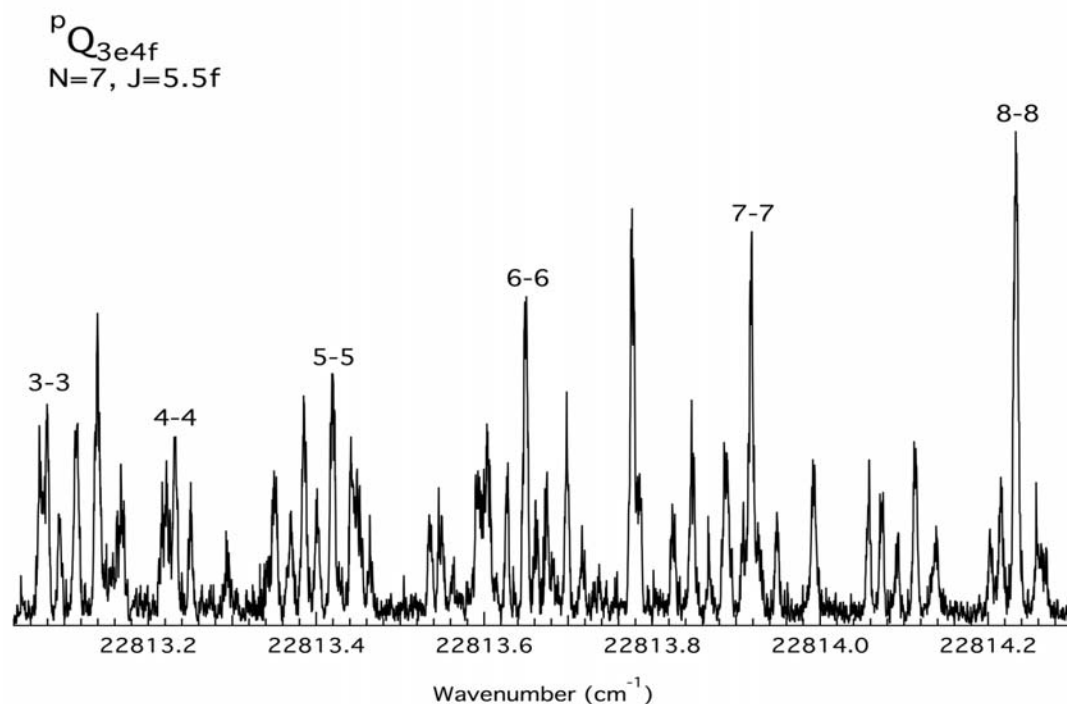


Figure 4.13 – Labelled hyperfine components of the $N'' = 7$ transition of the ${}^P Q_{3e4f}$ branch for the ${}^{187}\text{ReC}$ isotopologue. Each peak is labelled with the upper state F first, followed by the ground state F.

The less intense satellite peaks in the hyperfine structure have not been explained up to this point in the chapter. These peaks have been observed most obviously in the R branch because region four is the least congested of the spectrum. These satellite peaks can be explained as being less intense transitions where $\Delta F \neq \Delta J$. Only five of the six hyperfine components have a satellite peak, because the last peak does not have another upper state energy level to which it can make a transition. This is demonstrated in Figure 4.14. The satellite peaks also always appear at lower frequency in the R branch, and higher frequency in the P branch.

Although the satellite peaks are in the P branch, they are more difficult to identify because of overlap due to congestion.

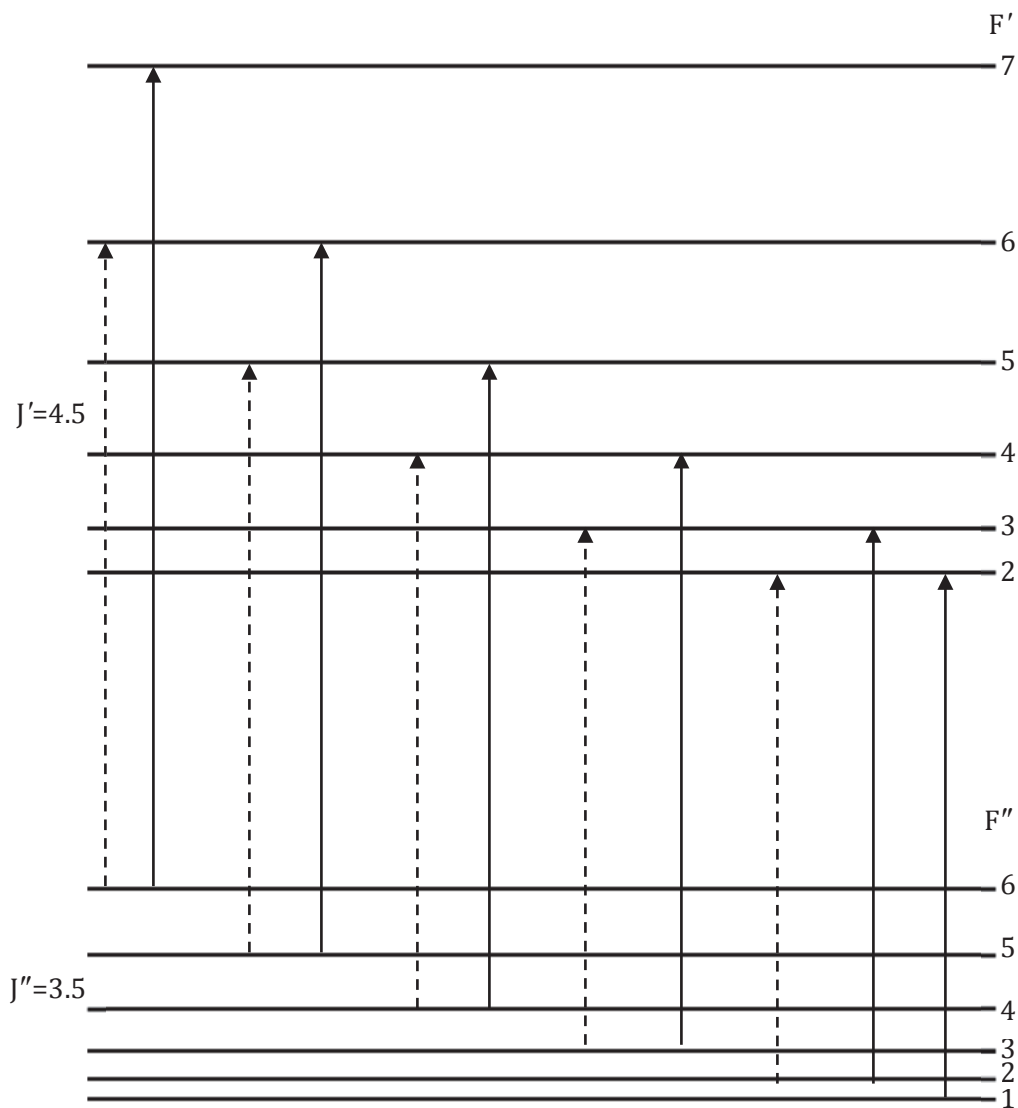


Figure 4.14 – Transition diagram of both the high intensity transitions and the low intensity satellite transitions that comprise the hyperfine structure of the R branch.

Solid lines are $\Delta F = \Delta J$ and dashed lines are $\Delta F \neq \Delta J$.

4.3 – Selective Detection

Up to this point in the analysis, the only branches to be identified and labelled involve the F1 and F4 J levels in the ground state. There have not been any branches found to be coming from the F2 and F3 levels. This poses a problem because the F1/F4 branches cannot be used to calculate combination differences that would help identify missing F2/F3 levels. An experiment was designed to help us identify which transitions in the congested regions of two and three involve either e parity or f parity. The monochromator was set with narrow slits to ensure that it only observes a small region of one particular branch at a time. This was first done by setting the monochromator to only observe the ${}^tR_{3e1e}$ branch in region four since it is the only branch in that region and, therefore, easy to isolate. Once the monochromator was set, the high-resolution laser was scanned across the congested regions. The only transitions that should be observed, are the transitions that involve the same upper excited state as the ${}^tR_{3e1e}$ branch, which is the upper excited state with e parity. This means that half of the spectrum should not appear, as half of the spectrum involves the upper excited state with f parity.

Unfortunately, there are a few main difficulties inherent in this kind of selective detection experiment. The signal strength of the ReC spectrum is strong in low-resolution, but at high-resolution the strong intensity of the band is spread between two isotopes and amongst all of the hyperfine components in the spectrum. This results in the intensity of individual hyperfine transitions being relatively weak. We therefore need a relatively high amount of light to be let through the monochromator in order to get significant signal-to-noise ratio. This amount of light

throughput is massively reduced once slit size is reduced. The main problem with this experiment is that we must be sure that the only branch within the bandpass of the monochromator is the ${}^tR_{3e1e}$ branch. In order to do this we must use a very small slit width, or adjust the monochromator further to higher wavenumber. Both of these options cause signal to decrease, and a balance must be found between these two adjustments such that there is a decent signal-to-noise ratio and only the ${}^tR_{3e1e}$ branch is observed.

We found the appropriate balance between these two factors, but were ultimately unsuccessful. We achieved an acceptable signal-to-noise ratio, but we observed all branches. We scanned over both congested regions two and three, but all peaks made an appearance. There are two possible reasons for this. It is possible that we were still allowing a small part of other branches through the band pass of the monochromator, either by too large of a slit width, or by not moving to high enough wavenumber. It is also possible that all branches still appear because the e and f parities in the upper excited state seem to be essentially degenerate, which we can observe by the utilization of combination differences that cross this ‘barrier’. This technique did not work out for us in the end, and was not able to separate between the two upper state parity levels, and was not able to help identify the F2 and F3 branches.

4.4 – ReC Molecular Jet with Argon Carrier Gas at Higher Pressure

Another technique used to gain more insight into the branch structure of the ReC spectrum, was to change the carrier gas from helium to argon, and to increase

the backpressure of the gas being pulsed into the reaction chamber from 40psi to 115psi. The reasoning behind these changes was to create a colder molecular beam. The reason a molecular jet is formed is that there is a high density of gas in the pulsed valve when a pulse of gas is shot into the reaction chamber. This high density causes a large number of collisions between the gas molecules, which accelerates the flow of the gas, and increases the directionality of the flow. When the carrier gas is changed from helium to argon, the size of the atoms is increased dramatically. This large increase in atom size increases the number of collisions, and the amount of energy transferred per collision, resulting in more rotational energy transfer into translational motion and, therefore, a more rotationally cold jet of molecules. In the same line of thought, increasing the pressure of gas going into the chamber has a similar effect. These changes result in a kinetically cooler molecular beam.

When the molecular beam is colder, this results in fewer of the higher J levels being populated, which in turn means that the lower J levels are more populated. This causes a reduction or complete disappearance of intensity for the higher J transitions, whereas the lower J transitions will become more intense. In effect, the structure of an entire band will change such that the beginning of each branch should be more obvious, and the trailing ends of the branches fade away. This means that there will also be less congestion in areas with mostly higher J transitions. For a visual example of how the overall band structure changed for the 438nm band in the low-resolution spectrum, see Figure 4.15.

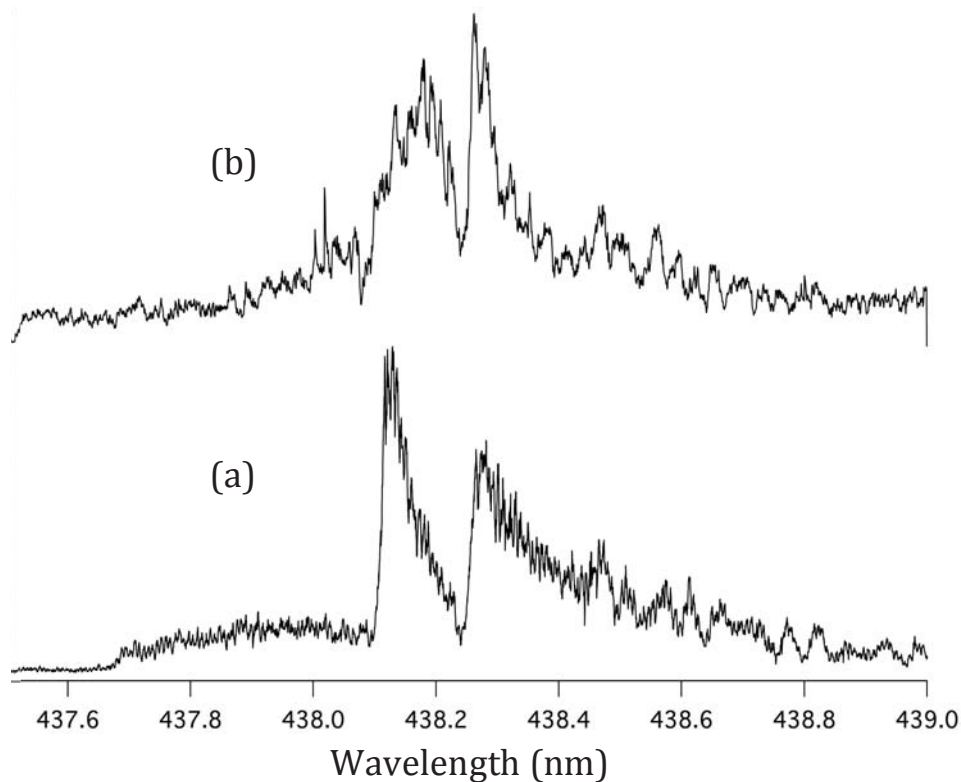


Figure 4.15 – A comparison between the low-resolution 438nm band taken with (a) Helium and (b) Argon as the carrier gas.

It is possible to see in low-resolution that the structure of regions 2 and 3 has changed significantly. It is also easy to see that the higher J transitions in regions 1 and 4 have decreased intensities, while the lower J transitions have become more noticeable. Once we had taken this low-resolution survey to show that this change of carrier gases made a significant difference, we switched to the high-resolution system to scan over the most congested regions 2 and 3. We did not need to scan over all of regions 1 or 4 using this technique because these regions were mostly uncongested and previously assigned. It was also expected for the F2/F3 branches to

all begin in regions 2 and 3. For an example of how the high-resolution branch structure changed in regions 3, see Figure 4.16.

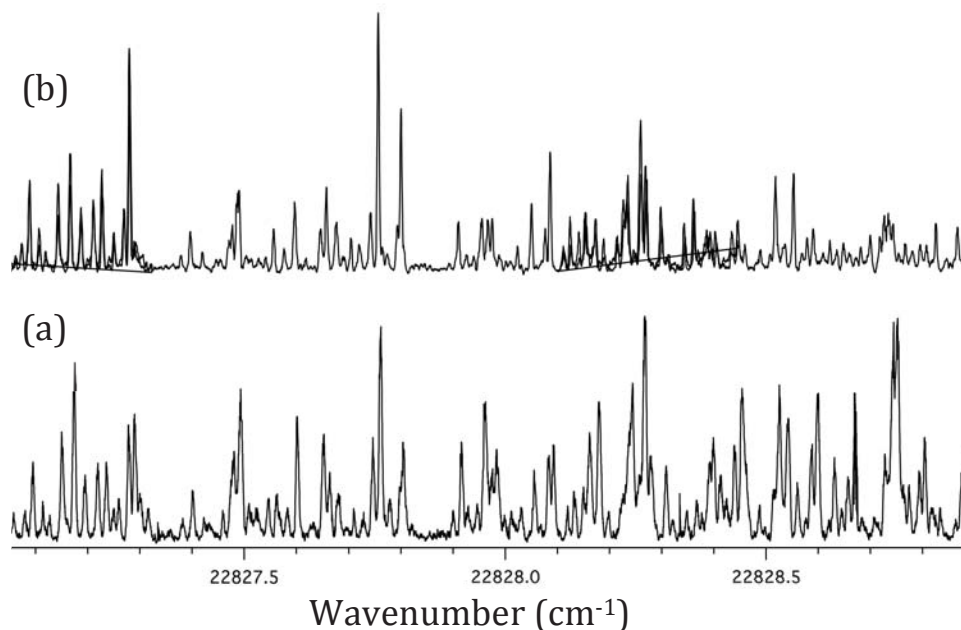


Figure 4.16 – A comparison between the high-resolution 438nm band in region 2 taken with (a) Helium and (b) Argon as the carrier gas.

4.5 – Strategies Utilized to Help Identify F2/F3 Branches Using the Cold Spectra

Once the cold spectrum was produced, we turned to regions 2 and 3 to try to identify the F2/F3 branches. We started by working to assign the lower J lines in these branches because they are now more prominent than the higher J lines in the more congested areas. As discussed previously, we could not use combination differences to find the F2/F3 components without first identifying at least one branch of each type. Therefore, we started off by lining up known transitions between the 438nm band and the 448nm band, except this time both bands were

taken with Argon. We did this using Igor Pro by stacking the two spectra on top of each other and offsetting the 448nm band such that a specified peak was aligned between bands. We then searched throughout regions 2 and 3 to see what other peaks were in common. As seen earlier in this section, when this is done, we should observe all transitions that correspond to the same upper state as the transition that was lined up between the two bands. For example, if we lined up on the ${}^tR_{3e1e}$, $N''=0$, $J''=1.5$, $F''=4$, then we expect to see the corresponding transitions in all the other branches in the spectrum. This is assuming that the F2/F3 branches behave in a similar manner to the F1/F4 branches, and that the previous assumption of the different upper state parity levels being essentially degenerate holds true. This technique was performed various times on various different branches and hyperfine components, and what resulted was a rather large number of peaks lining up between the two bands. It was, in fact, too many lines lining up between bands because the congestion of regions 2 and 3 was causing too many coincidental overlaps.

To try to eliminate this coincidental overlap problem, we decided to try a four-way line up of spectra. To accomplish this we had to duplicate the 438nm and 448nm bands so that there were two versions of each, all stacked on top of one another. This is because these are the only two bands for which we had a cold spectrum taken. The two spectra of the same band are lined up between two lines that correspond to one another, such as the ${}^tR_{3e1e}$, $N''=0$, $J''=1.5$, $F''=4$ transition in one 438nm band, and the ${}^sQ_{3e1e}$, $N''=1$, $J''=2.5$, $F''=5$ in the other 438nm band. The same is done for the 448nm band, and these lined up transitions are aligned between all four spectra. In effect, this technique should result in lines that line up between

all four spectra due to common combination differences between the transitions lined up on, and other transitions in the spectra. As an example, when the above lines are lined up between all the spectra, we should also see transitions aligned corresponding to the ${}^pQ_{3e4f}$, $N''=4$, $J''=2.5$, $F''=5$ transition and the ${}^oP_{3e4f}$, $N''=5$, $J''=3.5$, $F''=6$ transition. This should work for all of the branches, however, we only observed a four-way line up for the transitions corresponding to F1/F4 levels. In this case, rather than there being too many coincidental lines lined up between bands, these were the only line-ups at all. One explanation for why no F2/F3 branches were found in this four-way line up is that if one of the F2/F3 branches is too weak, we would not see it where we should. This explanation, however, does not make sense when looking at the intensities of the other branches in our spectrum, and the amount of unlabelled lines of decent intensity.

Another, more likely, explanation is that the hyperfine structure of the F2/F3 branches may be significantly different from the F1/F4 structure. One example of such a difference in hyperfine patterns is found in the molecule VO [6]. This study shows that it is possible that the hyperfine structure for the F2/F3 branches may rapidly get closer together and switch direction, while the F1/F4 hyperfine patterns are similar to the ${}^tR_{3e1e}$ branch in the ReC spectrum. This would make it significantly harder to properly identify the hyperfine patterns for these branches within the congested regions of 2 and 3. Currently, there are transitions, which have been tentatively labelled as the beginning of the ${}^sR_{3e2f}$ and the ${}^qQ_{3e2f}$ branches, but it is unclear how the branches continue from them, or what the hyperfine

patterns will be. Unfortunately, as of yet, the F2/F3 branches have not been fully identified or labelled.

4.6 – Spectrum Fitting and Constant Determination

The end goal of this thesis is not to simply label the peaks in the spectrum, however. We must utilize the labelled spectrum to determine the parameters that determine the spacing of the molecular energy levels. Pgoher [5] can be used for this purpose by fitting a simulated spectrum to an experimental spectrum, but it has difficulty when the spectrum gets too complex. We were able to use Pgoher to roughly fit our spectrum such that we could determine which labels belong on which branches, but it is not able to fit the whole spectrum with any degree of precision. This is likely due to the difficulty Pgoher has when it comes to dealing with large hyperfine splitting. This necessitated the need to design our own fitting program, which would be better able to handle our particular situation. To simplify this process, we utilized a previously written computer program that was designed to fit a spectrum with a $^4\Pi - ^4\Sigma^-$ transition, and it was made using software called Xcode [6]. The spectrum that it had been used for, however, did not contain the same hyperfine and parity issues that the ReC spectrum has. This resulted in the need to modify the existing program for our needs.

The first step in the modification process required us to input a new Hamiltonian matrix that includes hyperfine parameters for the ground state, which is where the majority of the hyperfine splitting occurs in ReC. This matrix already exists in literature[8], and each matrix element was written into the program. Once

input into the program, these matrix elements were all thoroughly tested using the appropriate set of quantum numbers to ensure that the output corresponds to the correct wavenumber for a given transition. The matrix used can be seen in Figure 4.15.

	$\left J \frac{1}{2} e \right\rangle$	$\left J \frac{3}{2} e \right\rangle$
$\left\langle J \frac{1}{2} e \right $	$-2\lambda - \frac{7}{2} \gamma + B(x+4) - \gamma_D(7x+16) - \frac{9}{4} \gamma_S - 2\lambda_D(x+4)$ $- D[(x+4)^2 + 7x + 4] + \frac{W}{2J(J+1)} \left[c_I + \frac{1}{4} (b+c-9b_S) \right]$ $\frac{e^2 Q q_0 [3W(W+1) - 4I(I+1)J(J+1)]}{8I(2I-1)J(J+1)(2J-1)(2J+3)}$ $\mp 2 \left(J + \frac{1}{2} \right) \left[B - \frac{1}{2} \gamma - 2D(x+4) - 2\lambda_D \right]$ $+ \frac{3}{2} \gamma_S - \frac{1}{2} \gamma_D(x+11) - (b-3b_S) \frac{W}{4J(J+1)}$	Symmetric
$\left\langle J \frac{3}{2} e \right $	$-\sqrt{3x} \left\{ B - \frac{1}{2} \gamma - 2D(x+2) - \frac{1}{2} \gamma_D(x+7) \right.$ $\left. - \gamma_S - (b+2b_S) \frac{W}{4J(J+1)} \right\}$ $\pm \left[-\sqrt{3x} \left(J + \frac{1}{2} \right) (2D + \gamma_D) \right]$	$2\lambda - \frac{3}{2} \gamma + Bx - 3\gamma_D x + 2\lambda_D x - D(x^2 + 3x)$ $+ \frac{9}{4} \gamma_S + \left[c_I + \frac{9}{4} (b+c+b_S) \right] \frac{W}{2J(J+1)}$ $+ \frac{e^2 Q q_0 (6-x) [3W(W+1) - 4I(I+1)J(J+1)]}{8I(2I-1)J(J+1)(2J-1)(2J+3)}$
$\left\langle J-1 \frac{1}{2} e \right $	$-\frac{Y}{8J} \left\{ b+c-9b_S + \frac{3e^2 Q q_0 [W+J+1]}{4I(2I-1)(J-1)(J+1)} \right\}$ $\mp \frac{Y}{4J} (b-3b_S)$	$\frac{Y}{8J} \sqrt{3(2J+3)/(2J-1)(b+2b_S)}$
$\left\langle J-1 \frac{3}{2} e \right $	$-\frac{Y}{8J} \sqrt{3(2J-3)/(2J+1)(b+2b_S)}$	$-\frac{3Y}{8J} \sqrt{(4J^2-9)/(4J^2-1)} \left\{ (b+c+b_S) \right.$ $\left. + \frac{3e^2 Q q_0 [W+J+1]}{4I(2I-1)(J-1)(J+1)} \right\}$
$\left\langle J-2 \frac{1}{2} e \right $	$e^2 Q q_0 \sqrt{J^2 - (1/4)} \sqrt{(J-1)^2 - (1/4)} Z$	0
$\left\langle J-2 \frac{3}{2} e \right $	0	$e^2 Q q_0 \sqrt{J^2 - (9/4)} \sqrt{(J-1)^2 - (9/4)} Z$

where

$$x = J(J+1) - \frac{3}{4}, \quad W = F(F+1) - I(I+1) - J(J+1), \quad Y = \sqrt{(I+J+F+1)(J+I-F)(F+J-I)(F+I-J+1)},$$

and

$$Z = Y \times \frac{3\sqrt{(F-I+J-1)(F+I+J)(J-F+I-1)(F+I-J+2)}}{16I(2I-1)J(J-1)(2J-1)\sqrt{(2J+1)(2J-3)}}$$

Figure 4.17 – Matrix of the rotational and hyperfine Hamiltonian for a $4\Sigma^-$ state,

where one spinning nucleus is present [6].

The program calculates every possible energy level of quantum number F by diagonalizing the Hamiltonian matrix, producing its eigenvalues and eigenvectors. However, the program does not know how to choose the eigenvalue requested by a given input. We must devise a way to determine which eigenvalue we want the program to give us. For a given input, up to 12 eigenvalues are produced, and the program labels them one through twelve. In the absence of hyperfine splitting, it is easy to select the eigenvector requested by looking for the maximum magnitude of probability amplitude for the basis vector(s) associated with the requested input. Further, one can find the energy order of the selected eigenvector. This energy order will not change when hyperfine coupling is introduced, even though the eigenvalues are changed and the eigenvectors will show strong mixing from this interaction. So, to select the requested eigenvalue one needs only to locate the value at the same position in the ordered list after hyperfine effects are introduced.

We also had to ensure that the program would properly interpret a given input and treat it as the appropriate energy level the input is intended to describe. Energy levels had to be specified with a certain combination of quantum numbers (N, J, F), and the parity as either e or f . It also had to be defined that certain levels are arranged in a specific way relative to one another. For example, it had to be defined that for a given N , there are four J values, and for each J there are six F values, and that the J and F levels are labelled with the lower number on the lowest energy level and the higher number on the highest energy level. It also had to be defined that the higher J energy level has e parity, and the parity alternated between J levels until the lower J level has f parity.

In order for the program to be used, a file must be made containing all of the labelled transitions that are to be fitted. This was done using a text-editing program, and the peaks must be written in this file in a specific format or the program will not recognize them. An example of the format is given below in Table 4.3:

Table 4.3 – Sample Program Input

2	5.5	1	7	1	4.5	3	7	22830.677
2	5.5	1	8	1	4.5	3	7	22830.7083
2	5.5	1	6	1	4.5	3	6	22831.0675
2	5.5	1	7	1	4.5	3	6	22831.095
2	5.5	1	5	1	4.5	3	5	22831.3518
2	5.5	1	6	1	4.5	3	5	22831.3737
2	5.5	1	4	1	4.5	3	4	22831.571
2	5.5	1	5	1	4.5	3	4	22831.5842
2	5.5	1	3	1	4.5	3	3	22831.7201
2	5.5	1	4	1	4.5	3	3	22831.7344
2	5.5	1	3	1	4.5	3	2	22831.8483

where the first and fifth columns indicate that the first set of numbers are for the upper excited state and the second set of numbers are for the ground state. The second and sixth columns indicate the J levels in the upper excited state and the ground state respectively. The third column indicates the N level for the upper excited state although N is not a ‘good’ quantum number in the upper excited state. Therefore, for the purpose of fitting, we just identify the upper state N as 1 for the e parity upper state, and -1 for the f parity upper state. The seventh column identifies the N level for the ground state. The fourth and eighth columns identify the F level for the upper excited state and the ground state respectively. Finally, the ninth column gives the wavenumber, in cm^{-1} , of the transition being described. The list

above identifies the hyperfine pattern, including satellite peaks, for the $N'' = 3$ transition of the ${}^tR_{3e1e}$ branch in region four.

During the input process, we must also identify any parameters that we wish to use in our fit. In the program itself, we included various parameters from the Hamiltonian matrix given in Figure 4.15, but we are not required to use all of them. If we find that a parameter does not have a significant impact on the fit, we may turn this parameter off. We set these parameters in the input file by numbering them in the same order as they are identified within the program. We then give them an approximate value to start with, based on a reasonable value to be expected, and set them as either fixed or free. This indicates whether the program fitting process may change this value or not. If we decide that we do not want to include a certain parameter in our fit, we may set its value to zero, and fix the parameter. In this way we may make use of the entire Hamiltonian matrix, or pick and choose which parts of it we want to use at any given time. Ultimately, once enough data has been entered into the program it should be able to both predict where unassigned lines are within a small deviation, and produce the appropriate constants with small standard deviations, by utilizing a nonlinear least squares fitting routine.

4.7 – Results of the Fitting Process

The labelled transitions for the ${}^tR_{3e1e}$, ${}^sQ_{3e1e}$, ${}^pQ_{3e4f}$, and the ${}^oP_{3e4f}$ branches were input into the program and fitted. The ${}^qR_{3e4f}$ and the ${}^rP_{3e1e}$ branches were not included in the fit because when their transitions were included the program was not able to handle them very well yet. This is likely due to a

combination of misassigned lines, because of the transitions being in the congested region, as well as the program not being able to handle hyperfine structure very well. The primary reason that the program is not able to properly handle the hyperfine structure or give a satisfactorily small deviation in the fit is due to there not being any F2/F3 branches input into the program. The reasons for this omission were discussed in the last section. Without these branches, the program cannot properly adjust to account for the possible changes that are affecting those branches. As an example of how the program is struggling to handle the hyperfine structure, Table 4.4 shows a portion of the output from the program.

Table 4.4 – Sample Program Output

22799.7409	22799.7428	-0.0019.	. . *	. . .
22799.4854	22799.4871	-0.0017.	. . *	. . .
22799.2479	22799.2471	0.0008.	. .	* . . .
22799.0219	22799.0227	-0.0008.	. . *	. . .
22798.8172	22798.8137	0.0035.	. .	* . .
22798.6260	22798.6203	0.0057.	. .	. * . .
22797.6085	22797.6111	-0.0026.	. . *	. . .
22797.3566	22797.3586	-0.0020.	. . *	. . .
22797.1183	22797.1204	-0.0021.	. . *	. . .
22796.8988	22796.8963	0.0025.	. .	*. . .
22796.6907	22796.6865	0.0042.	. .	.* . .
22796.4954	22796.4910	0.0044.	. .	.* . .

The first column is the experimentally identified wavenumber, the second column is the calculated wavenumber, the third column is the difference, and the diagram on the right plots the errors.

This segment of the output file shows the full hyperfine structure for 2 values of J for the ${}^PQ_{3e4f}$ branch. In the plot of the differences, it is possible to observe that for these two hyperfine patterns, the beginning of the pattern is calculated to be at lower wavenumber than experimental, and the end of the pattern is calculated to be higher than experimental. This indicates that the program is not yet properly fitting the hyperfine components. Even though the fitting program is not fully capable of describing the whole situation as yet, it does produce a very close approximation of the constants to describe the ReC molecule. The overall error of the fit is given as 0.0039 cm^{-1} , which is approximately twice as high as we would prefer it to be. This is because we would like for the error to be significantly smaller than the width of a line, which is roughly 0.0040 cm^{-1} in the cold 438 nm spectrum. The results of the fitting program in its current state for the 438 nm band are summarized in Table 4.5.

Table 4.5 – List of parameters as determined by our fit, with the values and associated errors given for both the ground and excited states in the 438nm band.

Parameters	Ground State (cm ⁻¹)	Excited State (cm ⁻¹)
B	0.51774 ± 0.000081	0.47989 ± 0.000080
10 ⁷ D	6.8 ± 0.53	-21.1 ± 0.38
λ _{ss}	0.111 ± 0.0074	-
γ	0.3207 ± 0.00021	-
b	0.1853 ± 0.00051	-
c	-0.117 ± 0.0048	-0.00041 ± 0.000017
e ² Qq ₀	-0.097 ± 0.0010	-0.032 ± 0.0072
b _s	0.066 ± 0.0010	-
T _o	-	22821.24 ± 0.051
h	-	0.084 ± 0.0023
o	-	-0.018 ± 0.0015

We were able to use the obtained ground state rotational constant, B , to determine the bond length of ReC in the ground state. This was done using the following equations:

$$I = \frac{h}{8\pi^2 c B}$$

$$R = \sqrt{\frac{I}{\mu}}$$

When our values were substituted into these equations we obtained a bond length of 1.699Å, which compares very well with the theoretical value of 1.731Å obtained from literature[9], and with Dr. Grein's predicted value of 1.66Å[2]. The obtained centrifugal distortion constant is positive with a reasonable value, which is indicative of not having a perturbed ground state. The hyperfine parameters obtained were

exceptionally large when compared to many molecules with prominent hyperfine splitting such as NbO[8], which possesses hyperfine parameters that differ by a factor of 10.

Using the B value obtained for the excited state, we determined a bond length of 1.764\AA , which indicates that the bond becomes looser when in the excited state. We also observed a large negative centrifugal distortion constant in the excited state, which indicates that there is some large perturbation affecting the excited state. It is also important to note that the hyperfine constants for the excited state were much smaller than the constants obtained for the ground state. This confirms that there is very little splitting occurring in the excited state.

After these approximate constants were determined, we decided to try using these numbers in Pgofer to see if it could simulate a close approximation of our spectrum. The spectrum produced is similar in structure, but when Pgofer is used to fit the data, the result still has an error of roughly 0.03cm^{-1} at best. While the Pgofer simulation is still useful to help label identified branches, and give approximate locations of where to find missing branches, it still is not accurate enough to reveal the locations of specific F2 or F3 transitions. It must also be noted that Pgofer seems to have a similar problem when trying to fit the hyperfine structures in the branches, because it will calculate some components to be either higher or lower than experimental within the same hyperfine structure. This is essentially the same as the result from our own fitting program except the Pgofer fit overall is less accurate by an approximate factor of 10.

4.8 – Lifetime Determination

The lifetimes for the 426 and 438 nm bands were measured. The term “lifetime” is used to express how long the excited state of ReC lives before decaying back to the ground state. A lifetime is measured by exciting the molecule and then recording the resulting fluorescence, monitored by a PMT, with an appropriate oscilloscope (one that has a good sensitivity and time base resolution). For each lifetime, there were various experimental curves produced, and each curve was averaged over 100 pulsed laser excitations. For the 426 nm band, there were four different curves recorded. One was with the ablation laser off with no dye laser scattering (recorded at $v=1$ and not $v=0$), another was with the ablation laser on with no dye laser scattering, another was with the ablation laser off with scattering (recorded at $v=0$), and another was with the ablation laser on with scattering. The purpose of recording lifetimes without dye laser scattering is because it removes noise from the decay curve. The curves with dye laser scattering were considered on a separate plot from the curves without dye laser scattering. In each of the two plots, another curve was generated by taking the difference. The resulting decay curve was less noisy, and easier to fit to produce a lifetime. The plots for the 426 nm band are given in Figures 4.13 and 4.14.

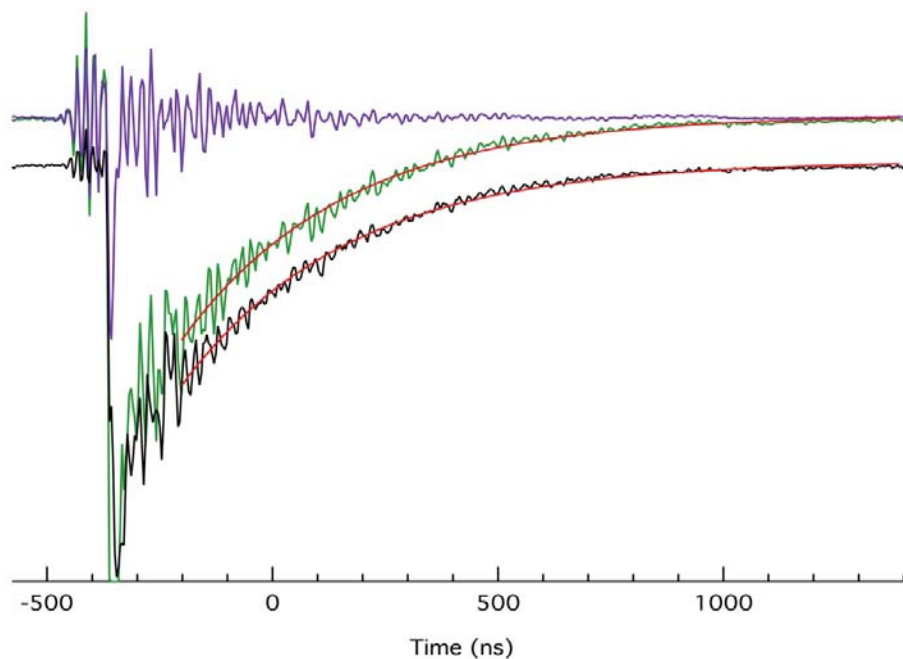


Figure 4.18 – Decay curves for the 426 nm band where the purple curve is with the ablation laser off with no scattering, the green curve is with the ablation laser on with no scattering, and the black curve is the difference between them. The red lines are from the exponential fit.

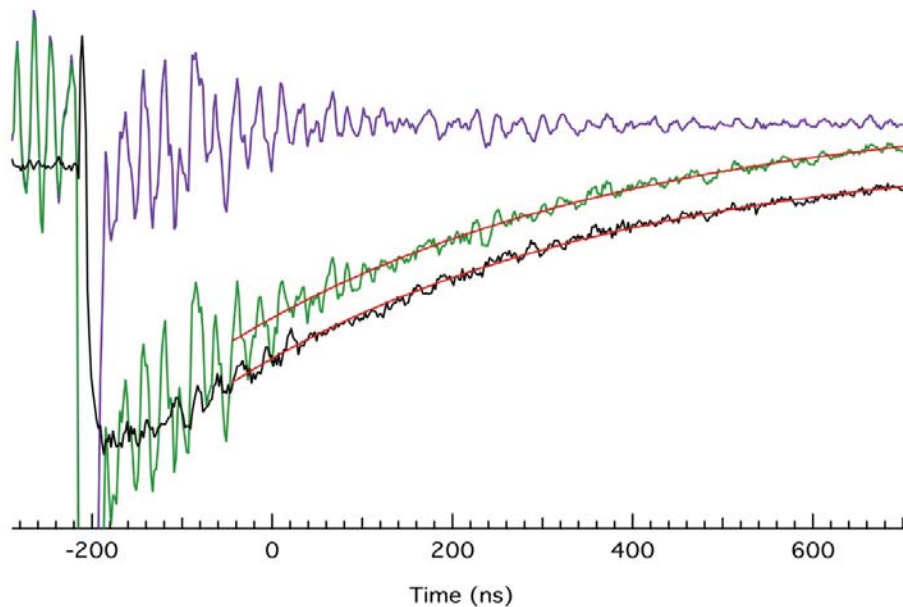


Figure 4.19 – Decay curves for the 426 nm band where the purple curve is with the ablation laser off with scattering, the green curve is with the ablation laser on with scattering, and the black curve is the difference between them. The red lines are from the exponential fit.

An exponential fit was done to both the curves with the ablation laser on (green), as well as the curves of the difference (black), and this directly gave the approximate lifetime of ReC for that band. The results are given in Table 4.6.

Table 4.6 – Lifetimes of ReC resulting from exponential fits to decay curves

Band	Curve	Lifetime (ns)
426 nm	Ablation laser on with no scattering	371 ± 6.7
	Difference curve with no scattering	369.4 ± 4.6
	Ablation laser on with scattering	419 ± 17.3
	Difference curve with scattering	398 ± 9.0

The obtained lifetimes are only approximate, but they are enough to see that ReC has a very long lifetime on the order of 400 ns in the 426 nm band. This is not what we expected to get, because Dr. Friedrich Grein's calculations [2] predicted that the lifetime would be short for a $^4\Pi - ^4\Sigma^-$ transition. There are other factors that could result in a long lifetime, which the calculations do not take into account, such as the Franck-Condon factor or perturbed excited states.

The lifetime for the 438 nm band was also determined from an exponential fit in the same manner as the 426 nm band. The curves with scattering were not considered in this band. There was also no difference taken, due to less noise in this band. The plot is given in figure 4.15. The lifetime resulting from the fit for the 438 nm band was 552 ± 12.5 ns, which is even longer than the lifetime found for the 426 nm band.

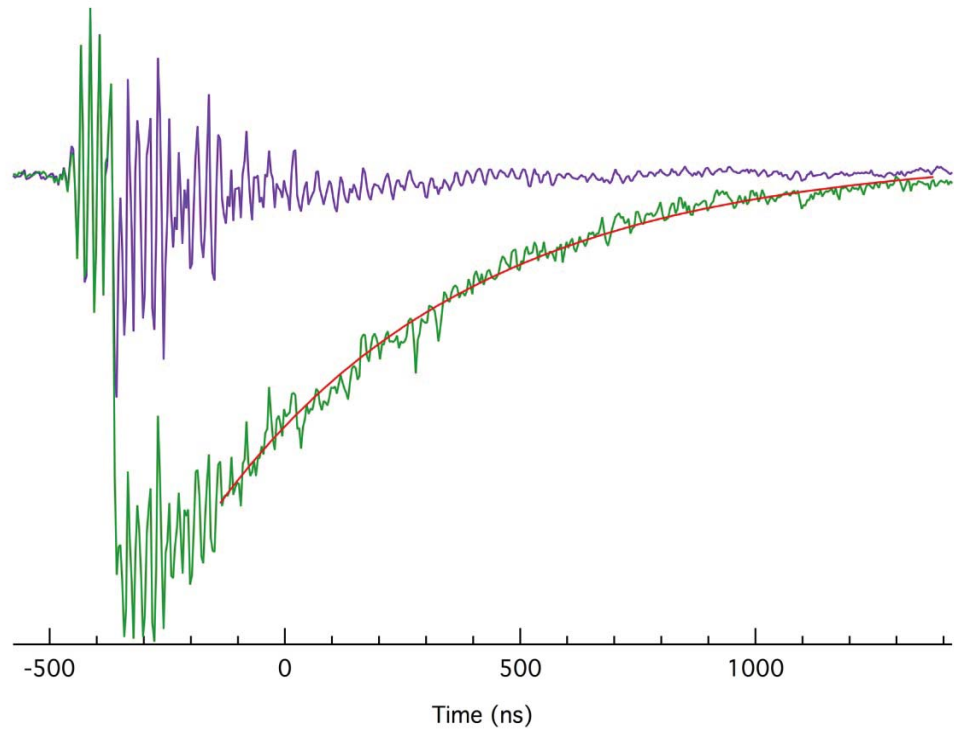


Figure 4.20 – Decay curves for the 438 nm band where the purple curve is with the ablation laser off with no scattering, and the green curve is with the ablation laser on with no scattering. The red line is from the exponential fit.

References

1. Weale, R., *High Resolution Laser Spectroscopy of Rhenium Carbide*. BSc Honours Thesis, Department of Chemistry, University of New Brunswick (2012)
2. Dr. Friedrich Grein, Personal Communication
3. Igor Pro, A Technical Graphing and Data Analysis Software, Wavemetrics, 2016, <https://www.wavemetrics.com/products/igorpro/igorpro.htm>
4. He, S.G., Tam, W.S., Leung, J.W-H., Cheung, A.S-C., *J. Chem. Phys.*, **117**, 5764-5769 (2002)
5. PGOPHER, A Program for Simulating Rotational, Vibrational and Electronic Spectra, C. M. Western, University of Bristol, 2016, <http://pgopher.chm.bris.ac.uk>
6. Xcode, An Integrated Development Environment, Apple Canada, Inc., 2016, <https://itunes.apple.com/ca/app/xcode/id497799835?mt=12>
7. Cheung, A.S-C., Hansen, R.C., Merer, A.J., *Journal of Molecular Spectroscopy*, **91**, 165-208 (1982)
8. Adam, A.G., Azuma, Y., Barry, J.A., Merer, A.J., Sassenberg, U., Schröder, J.O., *J. Chem. Phys.*, **100**, 6240-6262 (1994)
9. Wang, J., Sun, X., Wu, Z., *J. Cluster Science*. **18**, 333-344(2007)
10. Brugh, D.J., Morse, M.D., *J. Chem. Phys.* **117**, 10703-10714(2002)
11. DaBell, R.S., Meyer, R.G., Morse, M.D., *J. Chem. Phys.* **114**, 2938-2954(2001)

Chapter 5

Conclusions

5.0 – Conclusions

The high-resolution work completed for rhenium monocarbide was the first experimental study of this molecule, with the exception of the 426 nm band, for which the preliminary analysis had been started by a previous group member. This study introduced the large steps taken towards a better understanding of the rhenium monocarbide energy level structure. The study of the four ${}^4\Pi-X^4\Sigma^-$ bands revealed the complex hyperfine structure resulting from the rhenium atom's nuclear spin of $I=5/2$. The high-resolution spectra also made the obvious distinction between the two isotopologues of ${}^{187}\text{ReC}$ and ${}^{185}\text{ReC}$, which were both prominent in the spectrum with an approximate intensity ratio of 3:2. These discoveries allowed us to account for the vast number of transitions present in the spectra, and clarify that our spectrum was consistent with the predicted ${}^4\Pi-X^4\Sigma^-$ transition. There is also the observation that the spin-orbit components are not equally spaced as expected, which is an indication of perturbations affecting the excited state.

The analysis of the four band systems recorded at high-resolution allowed for the determination of six branches present in each band. The labelled transitions from

the 438 nm band were used to determine a number of molecular parameters. This was done using a computer program written to incorporate the appropriate Hamiltonian from the literature [1], and modifying it to account for the complexity of the hyperfine structure and parity present in the ReC spectrum. These parameters describe various aspects of the molecular system such as the rotational constant, and the centrifugal distortion and hyperfine constants. From the ground state rotational constant, we were able to obtain a bond length, which agreed well with the values predicted by Dr. Grein [2] and literature [3]. We also obtained an excited state rotational constant, from which we determined a larger bond distance than that of the ground state. We were also able to observe evidence of strong perturbations in the excited state due to the large negative centrifugal distortion parameter determined. It is also evident that the large hyperfine splitting is present in the ground state with very small hyperfine in the excited state.

However, a complete assignment of the rotational/hyperfine transitions in the four band systems was not achieved. While it was possible to assign the F1/F4 transitions, the F2/F3 transitions remain unassigned (or tentatively assigned at best). This resulted in the program not being able to completely handle the hyperfine splitting, and that the produced constants, while reasonably close, are not the final constants to properly describe the system.

Low-resolution dispersed fluorescence spectra were taken using a half-meter monochromator, and a clear vibrational progression was identified for both the ground state, and a low-lying excited state. A fit was performed on all dispersed fluorescence spectra and the vibrational frequency and anharmonicity constants were

determined and well defined for both states. The ground state vibrational frequency compared well with literature[3], and was also consistent with other carbides known in literature[4,5].

The lifetimes were also determined for both the 426 and 438nm bands, which indicated that ReC is longer lived than expected based on predictions [2]. This may be due to other factors such as the Franck-Condon factor or very perturbed excited states.

5.1 – Future Considerations

The largest obstruction to completely characterizing the structure of the ${}^4\Pi$ - $X^4\Sigma^-$ bands is the current inability to identify the F2/F3 branches. This, therefore, would be the primary objective to be solved next in future work on rhenium monocarbide. One technique that may still prove useful is the alignment between different bands. If we take cold spectra of the 426nm and 462nm bands as well, we can then get a four-way alignment between four different bands. This may help eliminate much of the coincidental peak alignments, and produce more useful results. There is also the trial-and-error process of labelling a line as a suspected transition, and calculating combination differences, and performing alignments to see if the suspected label is correct. This will be a time consuming process. However it is achieved, once an F2 branch is successfully assigned, the other F2 branches should be easily calculated using combination differences between the labelled F2 branch and the already assigned F1/F4 branches. The same can be said for the F3 branches. It must be noted, however, that finding a F2 branch does not necessarily

help find a F3 branch and vice versa, except by eliminating some of the congestion by the assignment of the F2 or F3 lines.

There are also other bands to take in high-resolution. The band at 499nm, which has already been taken, has not yet been extensively studied because it possesses a structure very different to that of the four bands reported in this thesis. The branches form a very congested head to the high wavenumber end of the spectrum and it will be difficult to analyse before the combination differences are all known for the current ${}^4\Pi-X^4\Sigma^-$ bands. It is currently suspected that the 499nm band corresponds to a ${}^4\Sigma^- - X^4\Sigma^-$ transition, but this has not yet been studied. As seen in the low-resolution survey, however, there are other bands yet to be explored.

References

1. Adam, A.G., Azuma, Y., Barry, J.A., Merer, A.J., Sassenberg, U., Schröder, J.O., *J. Chem. Phys.*, **100**, 6240-6262 (1994)
2. Dr. Friedrich Grein, Personal Communication
3. Wang, J., Sun, X., Wu, Z., *J. Cluster Science*. **18**, 333-344(2007)
4. Brugh, D.J., Morse, M.D., *J. Chem. Phys.* **117**, 10703-10714(2002)
5. DaBell, R.S., Meyer, R.G., Morse, M.D., *J. Chem. Phys.* **114**, 2938-2954(2001)

Appendix A
Full Low-Resolution Spectrum

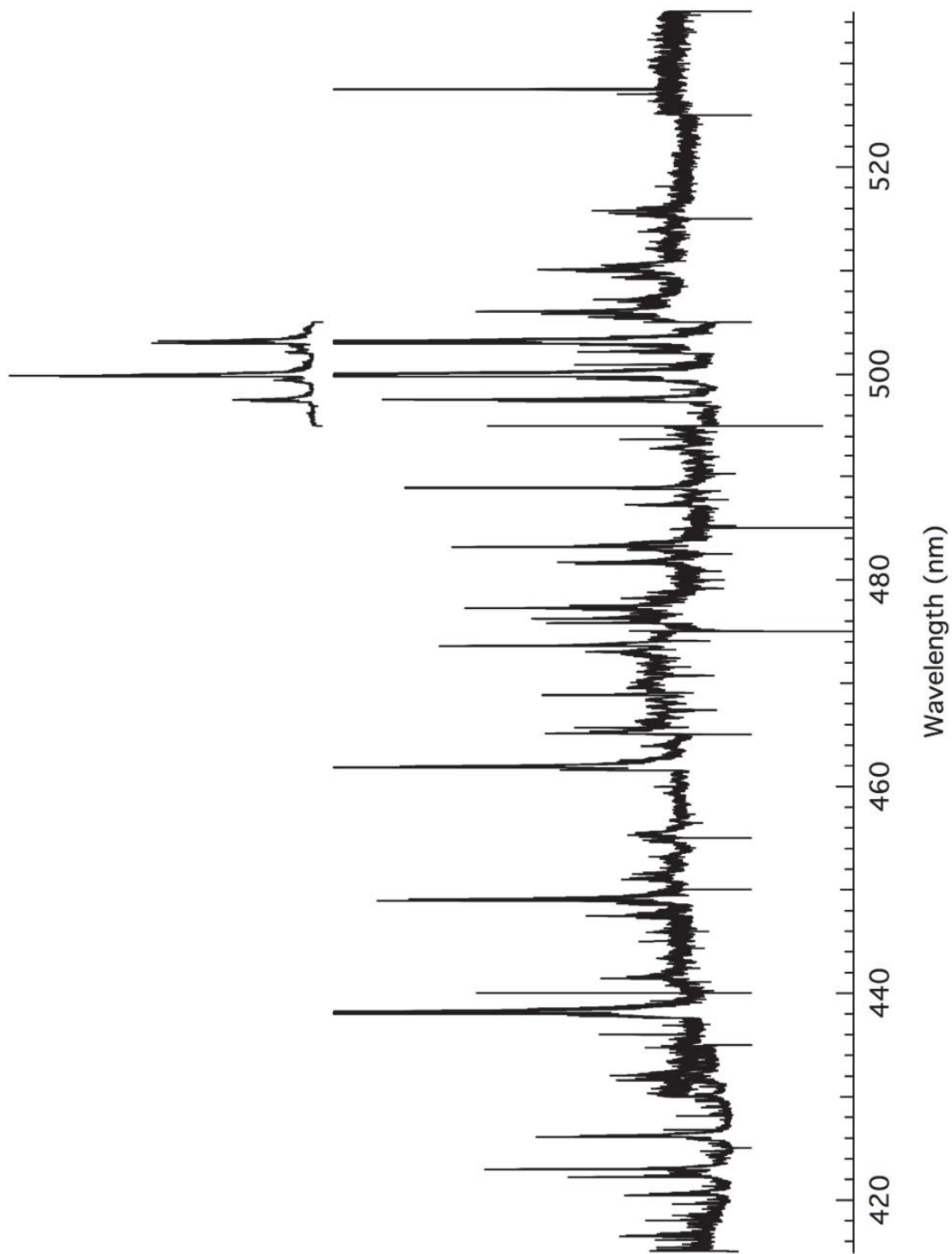


Figure A1 – Full Low-Resolution Survey Scan of ReC

Appendix B

DF Spectra With Wavelength Setting of Dye Laser

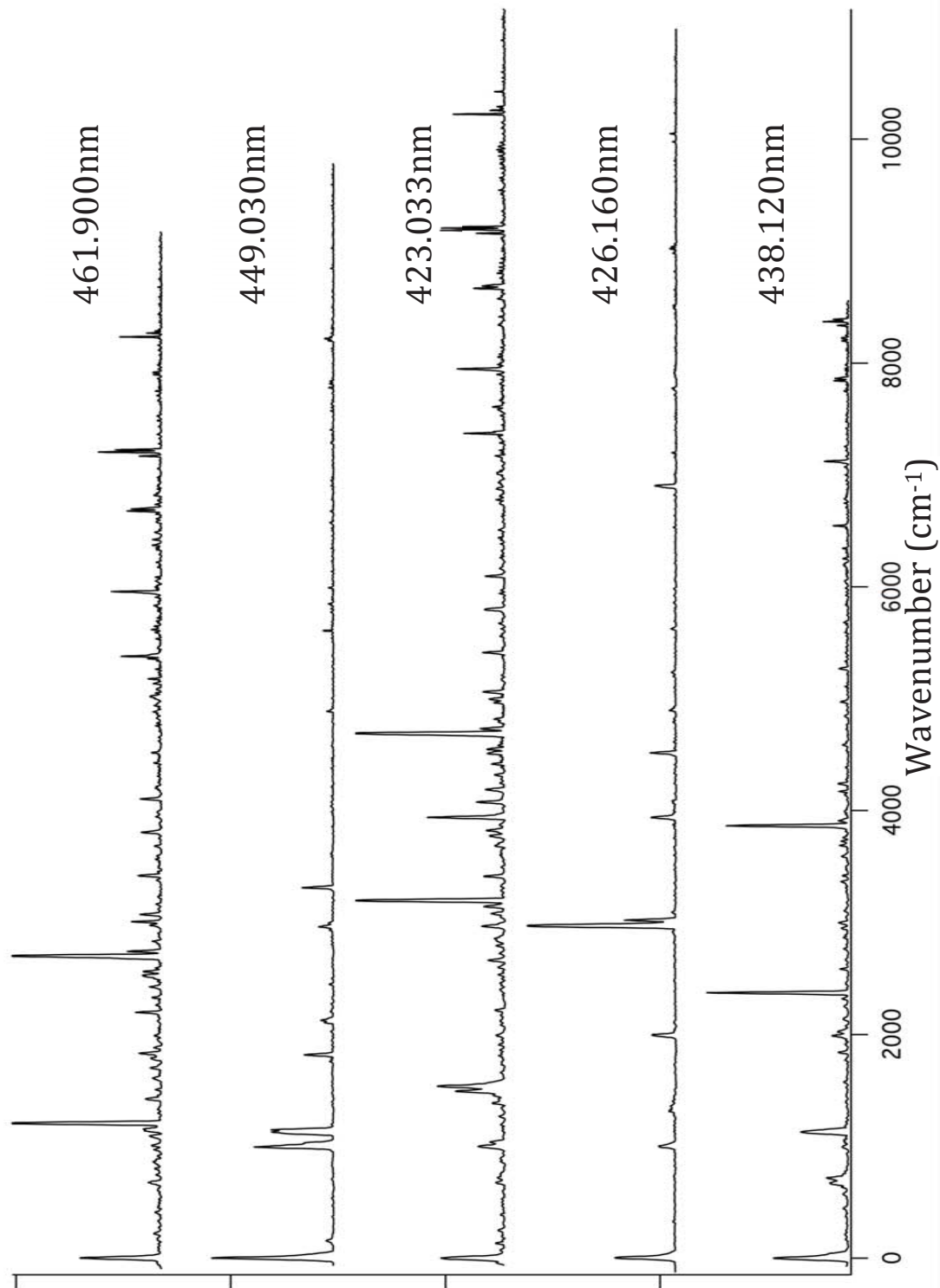


Figure B1 – Dispersed Fluorescence With Given Laser Frequencies pt.1.

*From bottom to top: DF26 – DF30

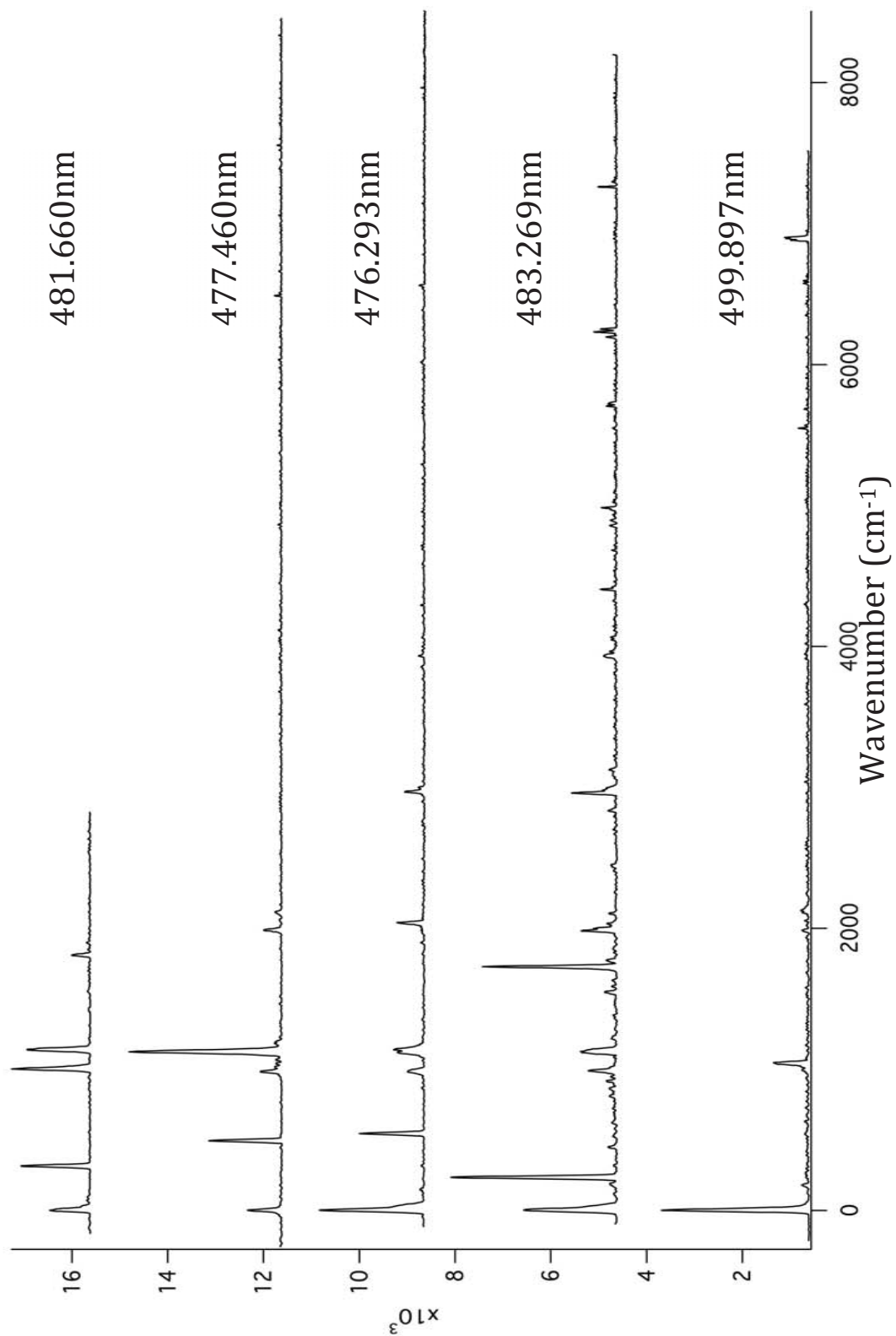


Figure B2 – Dispersed Fluorescence With Given Laser Frequencies pt.2.

*From bottom to top: DF31 – DF34 & DF36

Appendix C

Assignments for the ^{187}ReC Isotopologue in the 426nm Band

Table C1 – ${}^1R_{3e1e}$ Assignments for the ${}^{187}\text{ReC}$ Isotopologue in the 426nm Band

N''	J''	$F'-F''$	Peak Frequency (cm^{-1})
2	3.5	6-6	-
		7-6	23472.1445
		5-5	-
		6-5	23472.6289
		4-4	-
		5-4	23472.9648
		3-3	-
		4-3	23473.2070
		2-2	-
		3-2	23473.3730
3	4.5	7-7	-
		8-7	23473.8438
		6-6	-
		7-6	23474.2734
		5-5	-
		6-5	23474.5957
		4-4	-
		5-4	23474.8379
		3-3	-
		4-3	23475.0215
4	5.5	8-8	-
		9-8	23475.4570
		7-7	-
		8-7	23475.8516
		6-6	-
		7-6	23476.1582
		5-5	-
		6-5	23476.4043
		4-4	-
		5-4	23476.5957
4-3	23476.7539		

Table C1 cont. – ${}^1R_{3e1e}$ Assignments for the ${}^{187}\text{ReC}$ Isotopologue in the 426nm Band

N''	J''	$F'-F''$	Peak Frequency (cm^{-1})
5	6.5	9-9	-
		10-9	23476.9844
		8-8	-
		9-8	23477.3457
		7-7	-
		8-7	23477.6504
		6-6	-
		7-6	23477.8926
		5-5	-
		6-5	23478.0918
		5-4	23478.2539
6	7.5	10-10	-
		11-10	23478.4141
		9-9	-
		10-9	23478.7617
		8-8	-
		9-8	23479.0527
		7-7	-
		8-7	23479.3008
		6-6	-
		7-6	23479.5020
		6-5	23479.6680
7	8.5	11-11	-
		12-11	23479.7480
		10-10	-
		11-10	23480.0860
		9-9	-
		10-9	23480.3711
		8-8	-
		9-8	23480.6152
		7-7	-
		8-7	23480.8223
		7-6	23480.9961

Table C1 cont. – ${}^1R_{3e1e}$ Assignments for the ${}^{187}\text{ReC}$ Isotopologue in the 426nm Band

N''	J''	$F'-F''$	Peak Frequency (cm^{-1})
8	9.5	12-12	-
		13-12	23480.9961
		11-11	-
		12-11	23481.3203
		10-10	-
		11-10	23481.5977
		9-9	-
		10-9	23481.8398
		8-8	-
		9-8	23482.0449
		8-7	23482.2383
9	10.5	13-13	-
		14-13	23482.1406
		12-12	-
		13-12	23482.4590
		11-11	-
		12-11	23482.7305
		10-10	-
		11-10	23482.9766
		9-9	-
		10-9	23483.1836
		9-8	23483.3906
10	11.5	14-14	-
		15-14	23483.1934
		13-13	-
		14-13	23483.5000
		12-12	-
		13-12	23483.7676
		11-11	-
		12-11	23484.0176
		10-10	-
		11-10	23484.2168
		10-9	-

Table C2 – ${}^{\text{P}}\text{Q}_{3\text{e}4\text{f}}$ Assignments for the ${}^{187}\text{ReC}$ Isotopologue in the 426nm Band

N''	J''	$F'-F''$	Peak Frequency (cm^{-1})
4	2.5	5-5	23461.4160
		4-4	23461.1328
		3-3	23460.8633
		2-2	23460.6895
		1-1	-
		-	-
5	3.5	6-6	23460.1738
		5-5	23459.8848
		4-4	23459.6367
		3-3	23459.4570
		2-2	-
		1-1	-
6	4.5	7-7	23458.8281
		6-6	23458.5469
		5-5	23458.3047
		4-4	23458.1250
		3-3	23457.9473
		2-2	-
7	5.5	8-8	23457.3789
		7-7	23457.1035
		6-6	23456.8750
		5-5	23456.6816
		4-4	23456.5117
		3-3	23456.4004
8	6.5	9-9	23455.8320
		8-8	23455.5684
		7-7	-
		6-6	23455.1387
		5-5	23454.9512
		4-4	23454.8418
9	7.5	10-10	23454.1934
		9-9	23453.9277
		8-8	23453.6973
		7-7	23453.5000
		6-6	23453.3125

		5-5	23453.1738
--	--	-----	------------

Table C2 cont. – $^pQ_{3e4f}$ Assignments for the ^{187}ReC Isotopologue in the 426nm Band

N''	J''	$F'-F''$	Peak Frequency (cm^{-1})
10	8.5	11-11	23452.4531
		10-10	23452.1992
		9-9	23451.9609
		8-8	23451.7656
		7-7	23451.5781
		6-6	23451.4297
11	9.5	12-12	23450.6270
		11-11	23450.3711
		10-10	23450.1328
		9-9	23449.9316
		8-8	23449.7480
		7-7	23449.5879

Appendix D

Assignments for the ^{185}ReC Isotopologue in the 426nm Band

Table D1 – ${}^1R_{3e1e}$ Assignments for the ${}^{185}\text{ReC}$ Isotopologue in the 426nm Band

N''	J''	$F'-F''$	Peak Frequency (cm^{-1})
2	3.5	6-6	-
		7-6	23472.7246
		5-5	-
		6-5	23473.2070
		4-4	-
		5-4	23473.5430
		3-3	-
		4-3	-
		2-2	-
		3-2	23473.9473
		2-1	-
3	4.5	7-7	-
		8-7	23474.4355
		6-6	-
		7-6	23474.8594
		5-5	-
		6-5	23475.1816
		4-4	-
		5-4	23475.4219
		3-3	-
		4-3	23475.6055
		3-2	23475.344
4	5.5	8-8	-
		9-8	23476.0527
		7-7	-
		8-7	23476.4434
		6-6	-
		7-6	23476.7539
		5-5	-
		6-5	23477.0059
		4-4	-
		5-4	23477.1875
		4-3	23477.3359

Table D1 cont. – ${}^t\text{R}_{3e1e}$ Assignments for the ${}^{185}\text{ReC}$ Isotopologue in the 426nm Band

N''	J''	$F'-F''$	Peak Frequency (cm^{-1})
5	6.5	9-9	-
		10-9	23477.5879
		8-8	-
		9-8	23477.9531
		7-7	-
		8-7	23478.2539
		6-6	-
		7-6	23478.4961
		5-5	-
		6-5	23478.6895
		5-4	23478.8477
6	7.5	10-10	-
		11-10	23479.0254
		9-9	-
		10-9	23479.3750
		8-8	-
		9-8	23479.6680
		7-7	-
		8-7	23479.9102
		6-6	-
		7-6	23480.1113
		6-5	23480.2773
7	8.5	11-11	-
		12-11	23480.3711
		10-10	-
		11-10	23480.7148
		9-9	-
		10-9	23480.9961
		8-8	-
		9-8	23481.2422
		7-7	-
		8-7	23481.4473
		7-6	23481.6191

Table D1 cont. – ${}^1R_{3e1e}$ Assignments for the ${}^{185}\text{ReC}$ Isotopologue in the 426nm Band

N''	J''	$F'-F''$	Peak Frequency (cm^{-1})
8	9.5	12-12	-
		13-12	23481.6387
		11-11	-
		12-11	23481.9590
		10-10	-
		11-10	23482.2813
		9-9	-
		10-9	23482.4824
		8-8	-
		9-8	23482.6855
		8-7	23482.8672
9	10.5	13-13	-
		14-13	23482.8008
		12-12	-
		13-12	23483.1152
		11-11	-
		12-11	23483.3906
		10-10	-
		11-10	23483.6328
		9-9	-
		10-9	23483.8457
		9-8	-
10	11.5	14-14	-
		15-14	23483.8711
		13-13	-
		14-13	23484.1777
		12-12	-
		13-12	-
		11-11	-
		12-11	-
		10-10	-
		11-10	-
		9-9	-

Table D2 – ${}^p\text{Q}_{3e4f}$ Assignments for the ${}^{185}\text{ReC}$ Isotopologue in the 426nm Band

N''	J''	$F'-F''$	Peak Frequency (cm^{-1})
4	2.5	5-5	23461.9961
		4-4	-
		3-3	23461.4727
		2-2	23461.2559
		1-1	-
		-	-
5	3.5	6-6	23460.7383
		5-5	23460.4512
		4-4	-
		3-3	-
		2-2	-
		1-1	-
6	4.5	7-7	23459.3945
		6-6	23459.1152
		5-5	23458.8887
		4-4	-
		3-3	23458.5059
		2-2	-
7	5.5	8-8	23457.9473
		7-7	23457.6797
		6-6	-
		5-5	-
		4-4	-
		3-3	-
8	6.5	9-9	23456.4082
		8-8	23456.1465
		7-7	23455.9199
		6-6	23455.7246
		5-5	-
		4-4	23455.3828
9	7.5	10-10	23454.7715
		9-9	23454.5176
		8-8	23454.2930
		7-7	23454.0938
		6-6	23453.9180

		5-5	23453.7539
--	--	-----	------------

Table D2 cont. – $^pQ_{3e4f}$ Assignments for the ^{185}ReC Isotopologue in the 426nm Band

N''	J''	$F'-F''$	Peak Frequency (cm^{-1})
10	8.5	11-11	23453.0430
		10-10	23452.7910
		9-9	23452.5645
		8-8	23452.3750
		7-7	23452.1875
		6-6	23452.0313
11	9.5	12-12	23451.2227
		11-11	23450.9746
		10-10	23450.7480
		9-9	23450.5488
		8-8	23450.3555
		7-7	23450.2031
12	10.5	13-13	23449.3105
		12-12	23449.0586
		11-11	-
		10-10	-
		9-9	-
		8-8	-

Appendix E

Assignments for the ^{187}ReC Isotopologue in the 438nm Band

Table E1 – ${}^1R_{3e1e}$ Assignments for the ${}^{187}\text{ReC}$ Isotopologue in the 438nm Band

N''	J''	$F'-F''$	Peak Frequency (cm^{-1})
3	4.5	7-7	22830.6770
		8-7	22830.7083
		6-6	22831.0675
		7-6	22831.0950
		5-5	22831.3518
		6-5	22831.3737
		4-4	22831.5710
		5-4	22831.5842
		3-3	22831.7201
		4-3	22831.7344
4	5.5	3-2	22831.8483
		8-8	22832.2899
		9-8	22832.3140
		7-7	22832.6486
		8-7	22832.6710
		6-6	22832.9285
		7-6	22832.9482
		5-5	22833.1513
		6-5	22833.1639
		4-4	22833.3165
5	6.5	5-4	22833.3292
		4-3	22833.4513
		9-9	22833.8284
		10-9	22833.8484
		8-8	22834.1689
		9-8	22834.1865
		7-7	22834.4460
		8-7	22834.4614
		6-6	-
		7-6	22834.6798
5-5	22834.8447		
6-5	22834.8564		
5-4	22834.9960		

Table E1 cont. – ${}^4R_{3e1e}$ Assignments for the ${}^{187}\text{ReC}$ Isotopologue in the 438nm Band

N''	J''	$F'-F''$	Peak Frequency (cm^{-1})
6	7.5	10-10	22835.2930
		11-10	22835.3115
		9-9	22835.6225
		10-9	22835.6382
		8-8	22835.8953
		9-8	22835.9085
		7-7	-
		8-7	22836.1302
		6-6	22836.3041
		7-6	22836.3140
		6-5	22836.4558
7	8.5	11-11	22836.6870
		12-11	22836.7018
		10-10	22837.0019
		11-10	22837.0160
		9-9	22837.2750
		10-9	22837.2858
		8-8	-
		9-8	22837.5076
		7-7	22837.6909
		8-7	22837.6977
		7-6	22837.8539
8	9.5	12-12	22838.0061
		13-12	22838.0204
		11-11	22838.3195
		12-11	22838.3309
		10-10	22838.5883
		11-10	22838.5985
		9-9	-
		10-9	22838.8177
		8-8	-
		9-8	22839.0070
		8-7	22839.1743

Table E1 cont. – ${}^1R_{3e1e}$ Assignments for the ${}^{187}\text{ReC}$ Isotopologue in the 438nm Band

N''	J''	$F'-F''$	Peak Frequency (cm^{-1})
9	10.5	13-13	22839.2622
		14-13	22839.2717
		12-12	22839.5645
		13-12	22839.5743
		11-11	-
		12-11	22839.8354
		10-10	-
		11-10	22840.0626
		9-9	-
		10-9	22840.2602
		9-8	22840.4247
10	11.5	14-14	-
		15-14	22840.4466
		13-13	-
		14-13	22840.7397
		12-12	-
		13-12	22841.0049
		11-11	-
		12-11	22841.2341
		10-10	-
		11-10	22841.4301
		10-9	22841.6067
11	12.5	15-15	-
		16-15	22841.5544
		14-14	-
		15-14	22841.8502
		13-13	-
		14-13	22842.1083
		12-12	-
		13-12	22842.3381
		11-11	-
		12-11	22842.5402
		11-10	22842.7202

Table E1 cont. – ${}^4R_{3e1e}$ Assignments for the ${}^{187}\text{ReC}$ Isotopologue in the 438nm Band

N''	J''	$F'-F''$	Peak Frequency (cm^{-1})
12	13.5	16-16	-
		17-16	22842.5956
		15-15	-
		16-15	22842.8831
		14-14	-
		15-14	22843.1422
		13-13	-
		14-13	22843.3717
		12-12	-
		13-12	22843.5799
13	14.5	12-11	22843.7584
		17-17	-
		18-17	22843.5657
		16-16	-
		17-16	22843.8512
		15-15	-
		16-15	22844.1057
		14-14	-
		15-14	22844.3424
		13-13	-
14	15.5	14-13	22844.5481
		13-12	22844.7298
		18-18	-
		19-18	22844.4673
		17-17	-
		18-17	22844.7492
		16-16	-
		17-16	22845.0052
		15-15	-
		16-15	22845.2398
14	15.5	14-14	-
		15-14	22845.4481
		14-13	22845.6382

Table E1 cont. – ${}^1R_{3e1e}$ Assignments for the ${}^{187}\text{ReC}$ Isotopologue in the 438nm Band

N''	J''	$F'-F''$	Peak Frequency (cm^{-1})
15	16.5	19-19	-
		20-19	22845.3018
		18-18	-
		19-18	22845.5845
		17-17	-
		18-17	22845.8364
		16-16	-
		17-16	22846.0710
		15-15	-
		16-15	22846.2855
		15-14	22846.4750
16	17.5	20-20	-
		21-20	22846.0710
		19-19	-
		20-19	22846.3511
		18-18	-
		19-18	22846.6091
		17-17	-
		18-17	22846.8422
		16-16	-
		17-16	22847.0543
		16-15	22847.2464
17	18.5	21-21	-
		22-21	22846.7748
		20-20	-
		21-20	22847.0543
		19-19	-
		20-19	22847.3098
		18-18	-
		19-18	22847.5426
		17-17	-
		18-17	22847.7466
		17-16	22847.9335

Table E2 – ${}^{\text{P}}\text{Q}_{3\text{e}4\text{f}}$ Assignments for the ${}^{187}\text{ReC}$ Isotopologue in the 438nm Band

N''	J''	$F'-F''$	Peak Frequency (cm^{-1})
4	2.5	5-5	22818.4126
		4-4	22818.0100
		3-3	-
		2-2	-
		1-1	-
		-	-
5	3.5	6-6	22817.1064
		5-5	22816.7373
		4-4	22816.4471
		3-3	22816.2344
		2-2	22816.0657
		1-1	-
6	4.5	7-7	22815.7118
		6-6	22815.3727
		5-5	22815.0953
		4-4	22814.8653
		3-3	22814.6919
		2-2	-
7	5.5	8-8	22814.2333
		7-7	22813.9180
		6-6	22813.6493
		5-5	22813.4197
		4-4	22813.2317
		3-3	22813.0795
8	6.5	9-9	22812.6825
		8-8	22812.3788
		7-7	22812.1162
		6-6	22811.8922
		5-5	22811.6900
		4-4	22811.5338
9	7.5	10-10	22811.0517
		9-9	22810.7640
		8-8	22810.5044
		7-7	22810.2775
		6-6	22810.0778

		5-5	22809.9091
--	--	-----	------------

Table E2 cont. – $^{\text{P}}\text{Q}_{3e4f}$ Assignments for the ^{187}ReC Isotopologue in the 438nm Band

N''	J''	$F'-F''$	Peak Frequency (cm^{-1})
10	8.5	11-11	22809.3455
		10-10	22809.0651
		9-9	22808.8145
		8-8	22808.5857
		7-7	22808.3888
		6-6	22808.2111
11	9.5	12-12	22807.5694
		11-11	22807.2943
		10-10	22807.0460
		9-9	22806.8216
		8-8	22806.6163
		7-7	22806.4359
12	10.5	13-13	22805.7171
		12-12	22805.4464
		11-11	22805.2067
		10-10	22804.9818
		9-9	22804.7790
		8-8	22804.5899
13	11.5	14-14	22803.7949
		13-13	22803.5342
		12-12	22803.2921
		11-11	22803.0656
		10-10	22802.8592
		9-9	22802.6712
14	12.5	15-15	22801.8034
		14-14	22801.5458
		13-13	22801.3032
		12-12	22801.0818
		11-11	22800.8766
		10-10	22800.6835
15	13.5	16-16	22799.7409
		15-15	22799.4854
		14-14	22799.2479
		13-13	22799.0219

		12-12	22798.8172
		11-11	22798.6260

Table E2 cont. – $^pQ_{3e4f}$ Assignments for the ^{187}ReC Isotopologue in the 438nm Band

N''	J''	$F'-F''$	Peak Frequency (cm^{-1})
16	14.5	17-17	22797.6085
		16-16	22797.3566
		15-15	22797.1183
		14-14	22796.8988
		13-13	22796.6907
		12-12	22796.4954
17	15.5	18-18	22795.4071
		17-17	22795.1617
		16-16	22794.9102
		15-15	22794.7027
		14-14	22794.4929
		13-13	22794.2970

Table E3 – $^{\circ}\text{P}_{3f4f}$ Assignments for the ^{187}ReC Isotopologue in the 438nm Band

N''	J''	$F'-F''$	Peak Frequency (cm^{-1})
5	3.5	5-6	22813.7759
		4-5	22813.4010
		3-4	22813.1144
		2-3	22812.8938
		1-2	22812.6978
		0-1	22812.5825
6	4.5	6-7	22811.4177
		5-6	22811.0666
		4-5	22810.7791
		3-4	22810.5570
		2-3	22810.3933
		1-2	22810.2313
7	5.5	7-8	22808.9797
		6-7	22808.6525
		5-6	22808.3808
		4-5	22808.1441
		3-4	22807.9521
		2-3	22807.7975
8	6.5	8-9	22806.4626
		7-8	22806.1562
		6-7	22805.8889
		5-6	22805.6591
		4-5	22805.4563
		3-4	22805.2968
9	7.5	9-10	22803.8694
		8-9	22803.5803
		7-8	22803.3197
		6-7	22803.0873
		5-6	22802.8868
		4-5	22802.7152
10	8.5	10-11	22801.2063
		9-10	22800.9280
		8-9	22800.6701

		7-8	22800.4399
		6-7	22800.2385
		5-6	22800.0597

Table E3 cont. – $^{\circ}\text{P}_{3f4f}$ Assignments for the ^{187}ReC Isotopologue in the 438nm Band

N''	J''	$F'-F''$	Peak Frequency (cm^{-1})
11	9.5	11-12	22798.4694
		10-11	22798.1948
		9-10	22797.9430
		8-9	22797.7147
		7-8	22797.5080
		6-7	22797.3241
12	10.5	12-13	22795.6582
		11-12	22795.3863
		10-11	22795.1402
		9-10	22794.9102
		8-9	22794.7027
		7-8	22794.5182

Table E4 – ${}^sQ_{3f1e}$ Assignments for the ${}^{187}\text{ReC}$ Isotopologue in the 438nm Band

N''	J''	$F'-F''$	Peak Frequency (cm^{-1})
4	2.5	5-5	22818.8921
		4-4	22818.4971
		3-3	22818.2180
		2-2	-
		1-1	-
		-	-
5	3.5	6-6	22817.5687
		5-5	22817.2072
		4-4	22816.9290
		3-3	22816.6926
		2-2	-
		1-1	-
6	4.5	7-7	22816.1689
		6-6	22815.8411
		5-5	22815.5624
		4-4	22815.3376
		3-3	22815.1522
		2-2	22815.0152
7	5.5	8-8	22814.6919
		7-7	22814.3813
		6-6	22814.1134
		5-5	22813.8870
		4-4	22813.6983
		3-3	22813.5461
8	6.5	9-9	22813.1394
		8-8	22812.8450
		7-7	22812.5825
		6-6	22812.3557
		5-5	22812.1633
		4-4	22812.0039
		10-10	22811.5118

9	7.5	9-9	22811.2220
		8-8	22810.9723
		7-7	22810.7456
		6-6	22810.5467
		5-5	22810.3796

Table E4 cont. – ${}^sQ_{3f1e}$ Assignments for the ${}^{187}\text{ReC}$ Isotopologue in the 438nm Band

N''	J''	F'-F''	Peak Frequency (cm ⁻¹)
10	8.5	11-11	22809.8062
		10-10	22809.5283
		9-9	22809.2778
		8-8	22809.0507
		7-7	22808.8547
		6-6	22808.6801
11	9.5	12-12	22808.0240
		11-11	22807.7585
		10-10	22807.5123
		9-9	22807.2846
		8-8	22807.0843
		7-7	22806.9057
12	10.5	13-13	22806.1763
		12-12	22805.9134
		11-11	22805.6591
		10-10	22805.4464
		9-9	22805.2460
		8-8	22805.0591
13	11.5	14-14	22804.2566
		13-13	22803.9927
		12-12	22803.7548
		11-11	22803.5342
		10-10	22803.3285
		9-9	22803.1398
14	12.5	15-15	22802.2646
		14-14	22802.0041
		13-13	22801.7705
		12-12	22801.5458
		11-11	22801.3418
		10-10	22801.1508

15	13.5	16-16	22800.2012
		15-15	22799.9504
		14-14	22799.7128
		13-13	22799.4854
		12-12	22799.2850
		11-11	22799.0935

Table E4 cont. – $^8\text{Q}_{3f1e}$ Assignments for the ^{187}ReC Isotopologue in the 438nm Band

N''	J''	F'-F''	Peak Frequency (cm ⁻¹)
16	14.5	17-17	22798.0676
		16-16	22797.8208
		15-15	22797.5873
		14-14	22797.3566
		13-13	22797.1581
		12-12	22796.9667
17	15.5	18-18	22795.8661
		17-17	22795.6254
		16-16	22795.3863
		15-15	22795.1617
		14-14	-
		13-13	22794.7681

Table E5 – ${}^qR_{3f4f}$ Assignments for the ${}^{187}\text{ReC}$ Isotopologue in the 438nm Band

N''	J''	$F'-F''$	Peak Frequency (cm^{-1})
2	0.5	4-3	22822.2555
		3-2	22821.8220
		2-1	22821.5160
		-	
		-	
		-	
3	1.5	5-4	22822.0596
		4-3	22821.6591
		3-2	22821.3534
		2-1	22821.0647
		1-0	22820.9169
		-	
4	2.5	6-5	22821.7776
		5-4	22821.3990
		4-3	22821.1040
		3-2	22820.8480
		2-1	22820.6828
		1-0	22820.4771
5	3.5	7-6	22821.4122
		6-5	22821.0520
		5-4	-
		4-3	22820.5402
		3-2	22820.3720
		2-1	-
6	4.5	8-7	22820.9688
		7-6	22820.6387
		6-5	22820.3646
		5-4	22820.1397

		4-3	22819.9619
		3-2	22819.7863
7	5.5	9-8	22820.4489
		8-7	22820.1397
		7-6	22819.8735
		6-5	22819.6479
		5-4	22819.4638
		4-3	22819.3112

Table E5 cont. – ${}^q\text{R}_{3f4f}$ Assignments for the ${}^{187}\text{ReC}$ Isotopologue in the 438nm Band

N''	J''	$F'-F''$	Peak Frequency (cm^{-1})
8	6.5	10-9	22819.8524
		9-8	22819.5581
		8-7	22819.3031
		7-6	22819.0711
		6-5	22819.4638
		5-4	-
9	7.5	11-10	22819.1820
		10-9	22818.8921
		9-8	-
		8-7	22818.4126
		7-6	-
		6-5	22818.0808
10	8.5	12-11	22818.4312
		11-10	22818.1565
		10-9	-
		9-8	22817.6777
		8-7	22818.2278
		7-6	22817.3395
11	9.5	13-12	22817.6145
		12-11	22817.3395
		11-10	-
		10-9	22816.8645
		9-8	22817.4952
		8-7	-
12	10.5	14-13	22816.7147
		13-12	22816.4471
		12-11	-

		11-10	22815.9844
		10-9	22816.6926
		9-8	-

Table E6 – ${}^1P_{3e1e}$ Assignments for the ${}^{187}\text{ReC}$ Isotopologue in the 438nm Band

N''	J''	$F'-F''$	Peak Frequency (cm^{-1})
1	2.5	4-5	22821.4122
		3-4	22821.9857
		2-3	-
		1-2	-
		0-1	-
		-	-
2	3.5	5-6	22821.6073
		4-5	22821.7900
		3-4	-
		2-3	-
		1-2	-
		0-1	-
3	4.5	6-7	22821.1597
		5-6	22821.5243
		4-5	-
		3-4	-
		2-3	-
		1-2	-
4	5.5	7-8	22820.8479
		6-7	22821.1887
		5-6	-
		4-5	-
		3-4	-
		2-3	-
5	6.5	8-9	22820.4600
		7-8	22820.7930
		6-7	-

		5-6	-
		4-5	-
		3-4	-
6	7.5	9-10	22820.0011
		8-9	22820.3219
		7-8	-
		6-7	-
		5-6	-
		4-5	-

Table E6 cont. – ${}^1P_{3e1e}$ Assignments for the ${}^{187}\text{ReC}$ Isotopologue in the 438nm Band

N''	J''	$F'-F''$	Peak Frequency (cm^{-1})
7	8.5	10-11	22819.4763
		9-10	22819.7863
		8-9	-
		7-8	-
		6-7	-
		5-6	-
8	9.5	11-12	22818.8737
		10-11	22819.1820
		9-10	-
		8-9	-
		7-8	-
		6-7	-
9	10.5	12-13	22818.2037
		11-12	22818.4971
		10-11	-
		9-10	-
		8-9	-
		7-8	-
10	11.5	13-14	22817.4580
		12-13	22817.7468
		11-12	-
		10-11	-
		9-10	-
		8-9	-
		14-15	22816.6424
		13-14	22816.9190

11	12.5	12-13	-
		11-12	-
		10-11	-
		9-10	-
12	13.5	15-16	22815.7554
		14-15	22816.0193
		13-14	-
		12-13	-
		11-12	-
		10-11	-

Appendix F

Assignments for the ^{185}ReC Isotopologue in the 438nm Band

Table F1 – ${}^4R_{3e1e}$ Assignments for the ${}^{185}\text{ReC}$ Isotopologue in the 438nm Band

N''	J''	$F'-F''$	Peak Frequency (cm^{-1})
3	4.5	7-7	22831.1585
		8-7	22831.1890
		6-6	22831.5446
		7-6	22831.5710
		5-5	22831.8267
		6-5	22831.8413
		4-4	22832.0373
		5-4	22832.0549
		3-3	22832.1906
		4-3	22832.2052
4	5.5	3-2	22832.3140
		8-8	22832.7717
		9-8	22832.7950
		7-7	22833.1300
		8-7	22833.1513
		6-6	22833.4056
		7-6	22833.4239
		5-5	22833.6217
		6-5	22833.6371
		4-4	22833.7891
		5-4	22833.8007
		4-3	22833.9217
		9-9	22834.3125
		10-9	22834.3331
		8-8	22834.6558

5	6.5	9-8	22834.6729
		7-7	22834.9273
		8-7	22834.9421
		6-6	22835.1398
		7-6	22835.1537
		5-5	22835.3115
		6-5	22835.3276
		5-4	22835.4619

Table F1 cont. – ${}^1R_{3e1e}$ Assignments for the ${}^{185}\text{ReC}$ Isotopologue in the 438nm Band

N''	J''	F'-F''	Peak Frequency (cm ⁻¹)
6	7.5	10-10	22835.7821
		11-10	22835.7994
		9-9	22836.1087
		10-9	22836.1234
		8-8	22836.3715
		9-8	22836.3850
		7-7	22836.5937
		8-7	22836.6054
		6-6	22836.7783
		7-6	22836.7863
		6-5	22836.9357
7	8.5	11-11	-
		12-11	22837.1905
		10-10	22837.4907
		11-10	22837.5076
		9-9	22837.7566
		10-9	22837.7694
		8-8	22837.9820
		9-8	22837.9927
		7-7	-
		8-7	22838.1728
		7-6	22838.3194
		12-12	22838.5021
		13-12	22838.5145
		11-11	22838.8103
		12-11	22838.8177

8	9.5	10-10	-
		11-10	22839.0775
		9-9	-
		10-9	22839.3057
		8-8	-
		9-8	22839.4934
		8-7	22839.6562

Table F1 cont. – ${}^1R_{3e1e}$ Assignments for the ${}^{185}\text{ReC}$ Isotopologue in the 438nm Band

N''	J''	F'-F''	Peak Frequency (cm ⁻¹)
9	10.5	13-13	-
		14-13	22839.7624
		12-12	-
		13-12	22840.0626
		11-11	-
		12-11	22840.3262
		10-10	-
		11-10	22840.5478
		9-9	-
		10-9	22840.7397
		9-8	22840.9081
10	11.5	14-14	-
		15-14	22840.9450
		13-13	-
		14-13	22841.2341
		12-12	-
		13-12	22841.4944
		11-11	-
		12-11	22841.7223
		10-10	-
		11-10	22841.9229
		10-9	22842.0897
		15-15	-
		16-15	22842.0523
		14-14	-
		15-14	22842.3431

11	12.5	13-13	-
		14-13	22842.6028
		12-12	-
		13-12	22842.8278
		11-11	-
		12-11	22843.0277
		11-10	22843.2051

Table F1 cont. – ${}^1R_{3e1c}$ Assignments for the ${}^{185}\text{ReC}$ Isotopologue in the 438nm Band

N''	J''	F'-F''	Peak Frequency (cm ⁻¹)
12	13.5	16-16	-
		17-16	22843.0946
		15-15	-
		16-15	22843.3816
		14-14	-
		15-14	22843.6432
		13-13	-
		14-13	22843.8675
		12-12	-
		13-12	22844.0646
13	14.5	12-11	22844.2464
		17-17	-
		18-17	22844.0646
		16-16	-
		17-16	22844.3546
		15-15	-
		16-15	22844.6086
		14-14	-
		15-14	22844.8334
		13-13	-
		14-13	22845.0370
		13-12	22845.2232
		18-18	-
		19-18	22844.9702
		17-17	-

14	15.5	18-17	22845.2557
		16-16	-
		17-16	22845.5097
		15-15	-
		16-15	22845.7374
		14-14	-
		15-14	22845.9426
		14-13	22846.1300

Table F1 cont. – ${}^1R_{3e1e}$ Assignments for the ${}^{185}\text{ReC}$ Isotopologue in the 438nm Band

N''	J''	$F'-F''$	Peak Frequency (cm^{-1})
15	16.5	19-19	-
		20-19	22845.8081
		18-18	-
		19-18	22846.0905
		17-17	-
		18-17	22846.3511
		16-16	-
		17-16	22846.5810
		15-15	-
		16-15	22846.7849
		15-14	22846.9788
16	17.5	20-20	-
		21-20	22846.5810
		19-19	-
		20-19	22847.8658
		18-18	-
		19-18	22847.1166
		17-17	-
		18-17	22847.3451
		16-16	-
		17-16	22847.5571
		16-15	22847.7561
		21-21	-
		22-21	22847.2926
		20-20	-

17	18.5	21-20	22847.5689
		19-19	-
		20-19	22847.8196
		18-18	-
		19-18	-
		17-17	-
		18-17	-
		17-16	-

Table F2 – ${}^PQ_{3e4f}$ Assignments for the ${}^{185}\text{ReC}$ Isotopologue in the 438nm Band

N''	J''	$F'-F''$	Peak Frequency (cm^{-1})
4	2.5	5-5	22818.8921
		4-4	22818.4971
		3-3	22818.2180
		2-2	-
		1-1	-
		-	-
5	3.5	6-6	22817.5687
		5-5	22817.2072
		4-4	22816.9290
		3-3	22816.6926
		2-2	-
		1-1	-
6	4.5	7-7	22816.1689
		6-6	22815.8411
		5-5	22815.5624
		4-4	22815.3376
		3-3	22815.1522
		2-2	22815.0152
7	5.5	8-8	22814.6919
		7-7	22814.3813
		6-6	22814.1134
		5-5	22813.8870
		4-4	22813.6983

		3-3	22813.5461
8	6.5	9-9	22813.1394
		8-8	22812.8450
		7-7	22812.5825
		6-6	22812.3557
		5-5	22812.1633
		4-4	22812.0039
9	7.5	10-10	22811.5118
		9-9	22811.2220
		8-8	22810.9723
		7-7	22810.7456
		6-6	22810.5467
		5-5	22810.3796

Table F2 cont. – $^{\text{p}}\text{Q}_{3\text{e}4\text{f}}$ Assignments for the ^{185}ReC Isotopologue in the 438nm Band

N''	J''	$F'-F''$	Peak Frequency (cm^{-1})
10	8.5	11-11	22809.8062
		10-10	22809.5283
		9-9	22809.2778
		8-8	22809.0507
		7-7	22808.8547
		6-6	22808.6801
11	9.5	12-12	22808.0240
		11-11	22807.7585
		10-10	22807.5123
		9-9	22807.2846
		8-8	22807.0843
		7-7	22806.9057
12	10.5	13-13	22806.1763
		12-12	22805.9134
		11-11	22805.6591
		10-10	22805.4464
		9-9	22805.2460
		8-8	22805.0591
13	11.5	14-14	22804.2566
		13-13	22803.9927
		12-12	22803.7548
		11-11	22803.5342

		10-10	22803.3285
		9-9	22803.1398
14	12.5	15-15	22802.2646
		14-14	22802.0041
		13-13	22801.7705
		12-12	22801.5458
		11-11	22801.3418
		10-10	22801.1508
		15	13.5
15-15	22799.9504		
14-14	22799.7128		
13-13	22799.4854		
12-12	22799.2850		
11-11	22799.0935		

Table F2 cont. – $^{\text{P}}\text{Q}_{3\text{e}4\text{f}}$ Assignments for the ^{185}ReC Isotopologue in the 438nm Band

N''	J''	$\text{F}'\text{-F}''$	Peak Frequency (cm^{-1})
16	14.5	17-17	22798.0676
		16-16	22797.8208
		15-15	22797.5873
		14-14	22797.3566
		13-13	22797.1581
		12-12	22796.9667
17	15.5	18-18	22795.8661
		17-17	22795.6254
		16-16	22795.3863
		15-15	22795.1617
		14-14	-
		13-13	22794.7681

Table F3 – $^{\circ}\text{P}_{3f4f}$ Assignments for the ^{185}ReC Isotopologue in the 438nm Band

N''	J''	$F'-F''$	Peak Frequency (cm^{-1})
4	2.5	4-5	22816.5217
		3-4	22816.1293
		2-3	-
		1-2	22815.5951
		-	-
		-	-
5	3.5	5-6	22814.2333
		4-5	22813.8674
		3-4	-
		2-3	22813.3507
		1-2	22813.1676
		-	-
6	4.5	6-7	22811.8758
		5-6	22811.5338
		4-5	22811.2397
		3-4	22811.0170
		2-3	22810.8346
		1-2	-
7	5.5	7-8	22809.4330
		6-7	22809.1135
		5-6	22808.8299

		4-5	22808.6059
		3-4	22808.4170
		2-3	22808.2460
8	6.5	8-9	22806.9177
		7-8	22806.6163
		6-7	22806.3477
		5-6	22806.1185
		4-5	22805.9248
		3-4	22805.7579
9	7.5	9-10	22804.3272
		8-9	22804.0356
		7-8	22803.7759
		6-7	22803.5493
		5-6	22803.3501
		4-5	22803.1788

Table F3 cont. – $^{\circ}\text{P}_{3f4f}$ Assignments for the ^{185}ReC Isotopologue in the 438nm Band

N''	J''	$F'-F''$	Peak Frequency (cm^{-1})
10	8.5	10-11	22801.6589
		9-10	22801.3794
		8-9	22801.1254
		7-8	22800.9032
		6-7	22800.6995
		5-6	22800.5206
11	9.5	11-12	22798.9185
		10-11	22798.6501
		9-10	22798.3982
		8-9	22798.1743
		7-8	22797.9708
		6-7	22797.7877
12	10.5	12-13	22796.1052
		11-12	22795.8380
		10-11	22795.5959
		9-10	22795.3863
		8-9	22795.1747
		7-8	-

Table F4 – ${}^sQ_{3f1e}$ Assignments for the ${}^{185}\text{ReC}$ Isotopologue in the 438nm Band

N''	J''	$F'-F''$	Peak Frequency (cm^{-1})
4	2.5	5-5	22818.8921
		4-4	22818.4971
		3-3	22818.2180
		2-2	-
		1-1	-
		-	-
5	3.5	6-6	22817.5687
		5-5	22817.2072
		4-4	22816.9290
		3-3	22816.6926
		2-2	-
		1-1	-
6	4.5	7-7	22816.1689
		6-6	22815.8411
		5-5	22815.5624
		4-4	22815.3376
		3-3	22815.1522
		2-2	22815.0152
7	5.5	8-8	22814.6919
		7-7	22814.3813
		6-6	22814.1134

		5-5	22813.8870
		4-4	22813.6983
		3-3	22813.5461
8	6.5	9-9	22813.1394
		8-8	22812.8450
		7-7	22812.5825
		6-6	22812.3557
		5-5	22812.1633
		4-4	22812.0039
9	7.5	10-10	22811.5118
		9-9	22811.2220
		8-8	22810.9723
		7-7	22810.7456
		6-6	22810.5467
		5-5	22810.3796

Table F4 cont. – $^sQ_{3f1e}$ Assignments for the ^{185}ReC Isotopologue in the 438nm Band

N''	J''	$F'-F''$	Peak Frequency (cm^{-1})
10	8.5	11-11	22809.8062
		10-10	22809.5283
		9-9	22809.2778
		8-8	22809.0507
		7-7	22808.8547
		6-6	22808.6801
11	9.5	12-12	22808.0240
		11-11	22807.7585
		10-10	22807.5123
		9-9	22807.2846
		8-8	22807.0843
		7-7	22806.9057
12	10.5	13-13	22806.1763
		12-12	22805.9134
		11-11	22805.6591
		10-10	22805.4464
		9-9	22805.2460
		8-8	22805.0591
		14-14	22804.2566
		13-13	22803.9927

13	11.5	12-12	22803.7548
		11-11	22803.5342
		10-10	22803.3285
		9-9	22803.1398
14	12.5	15-15	22802.2646
		14-14	22802.0041
		13-13	22801.7705
		12-12	22801.5458
		11-11	22801.3418
		10-10	22801.1508
15	13.5	16-16	22800.2012
		15-15	22799.9504
		14-14	22799.7128
		13-13	22799.4854
		12-12	22799.2850
		11-11	22799.0935

Table F4 cont. – $^sQ_{3f1e}$ Assignments for the ^{185}ReC Isotopologue in the 438nm Band

N''	J''	$F'-F''$	Peak Frequency (cm^{-1})
16	14.5	17-17	22798.0676
		16-16	22797.8208
		15-15	22797.5873
		14-14	22797.3566
		13-13	22797.1581
		12-12	22796.9667
17	15.5	18-18	22795.8661
		17-17	22795.6254
		16-16	22795.3863
		15-15	22795.1617
		14-14	-
		13-13	22794.7681

Table F5 – ${}^qR_{3f4f}$ Assignments for the ${}^{185}\text{ReC}$ Isotopologue in the 438nm Band

N''	J''	$F'-F''$	Peak Frequency (cm^{-1})
2	0.5	4-3	22822.7240
		3-2	22822.2821
		2-1	-
		-	-
		-	-
		-	-
3	1.5	5-4	22822.5277
		4-3	22822.1270
		3-2	-
		2-1	-
		1-0	-
		-	-
4	2.5	6-5	22822.2456
		5-4	22821.8733
		4-3	-
		3-2	-
		2-1	-
		1-0	-
		7-6	22822.0794

5	3.5	6-5	22821.5243
		5-4	-
		4-3	-
		3-2	-
		2-1	-
6	4.5	8-7	22821.8063
		7-6	22821.1040
		6-5	-
		5-4	-
		4-3	-
		3-2	-
7	5.5	9-8	22821.4280
		8-7	22820.6067
		7-6	-
		6-5	-
		5-4	-
		4-3	-

Table F5 cont. – ${}^qR_{3f4f}$ Assignments for the ${}^{185}\text{ReC}$ Isotopologue in the 438nm Band

N''	J''	$F'-F''$	Peak Frequency (cm^{-1})
8	6.5	10-9	22820.9374
		9-8	22820.0233
		8-7	-
		7-6	-
		6-5	-
		5-4	-
9	7.5	11-10	22820.3431
		10-9	22819.3680
		9-8	-
		8-7	-
		7-6	-
		6-5	-
10	8.5	12-11	22819.6593
		11-10	22818.6232
		10-9	-
		9-8	-
		8-7	-
		7-6	-

11	9.5	13-12	22818.8737
		12-11	22817.8094
		11-10	-
		10-9	-
		9-8	-
		8-7	-
12	10.5	14-13	22817.9999
		13-12	-
		12-11	-
		11-10	-
		10-9	-
		9-8	-

Table F6 – ${}^1P_{3e1e}$ Assignments for the ${}^{185}\text{ReC}$ Isotopologue in the 438nm Band

N''	J''	$F'-F''$	Peak Frequency (cm^{-1})
1	2.5	4-5	22822.0794
		3-4	22822.4518
		2-3	-
		1-2	-
		0-1	-
		-	-
2	3.5	5-6	22821.8857
		4-5	22822.2555
		3-4	-
		2-3	-
		1-2	-
		0-1	-
3	4.5	6-7	22821.6328
		5-6	22821.9962
		4-5	-
		3-4	-
		2-3	-
		1-2	-

4	5.5	7-8	22821.3168
		6-7	22821.6652
		5-6	-
		4-5	-
		3-4	-
		2-3	-
5	6.5	8-9	22820.9374
		7-8	22821.2642
		6-7	-
		5-6	-
		4-5	-
		3-4	-
6	7.5	9-10	22820.4771
		8-9	22820.7930
		7-8	-
		6-7	-
		5-6	-
		4-5	-

Table F6 cont. – ${}^1P_{3e1e}$ Assignments for the ${}^{185}\text{ReC}$ Isotopologue in the 438nm Band

N''	J''	$F'-F''$	Peak Frequency (cm^{-1})
7	8.5	10-11	22819.9489
		9-10	22820.2585
		8-9	-
		7-8	-
		6-7	-
		5-6	-
8	9.5	11-12	22819.3464
		10-11	22819.6479
		9-10	-
		8-9	-
		7-8	-
		6-7	-
9	10.5	12-13	22818.6728
		11-12	22818.9756
		10-11	-
		9-10	-
		8-9	-

		7-8	-
10	11.5	13-14	22817.9344
		12-13	22818.2278
		11-12	-
		10-11	-
		9-10	-
		8-9	-
11	12.5	14-15	22817.1198
		13-14	22817.4099
		12-13	-
		11-12	-
		10-11	-
		9-10	-
12	13.5	15-16	22816.2344
		14-15	22816.5129
		13-14	-
		12-13	-
		11-12	-
		10-11	-

Appendix G

Assignments for the ^{187}ReC Isotopologue in the 448nm Band

Table G1 – ${}^1R_{3e1e}$ Assignments for the ${}^{187}\text{ReC}$ Isotopologue in the 448nm Band

N''	J''	$F'-F''$	Peak Frequency (cm^{-1})
3	4.5	7-7	22275.6031
		8-7	22275.6118
		6-6	22275.9699
		7-6	22275.9990
		5-5	22276.2524
		6-5	22276.2755
		4-4	22276.4595
		5-4	22276.4793
		3-3	22276.6215
		4-3	22276.6373
		3-2	22276.7369
4	5.5	8-8	22277.1573
		9-8	22277.1846
		7-7	22277.5187
		8-7	22277.5422
		6-6	22277.7992
		7-6	22277.8152

		5-5	22278.0142
		6-5	22278.0299
		4-4	22278.1814
		5-4	22278.1958
		4-3	22278.3201
5	6.5	9-9	-
		10-9	22278.6851
		8-8	22279.0007
		9-8	22279.0216
		7-7	22279.2773
		8-7	22279.2945
		6-6	-
		7-6	22279.5101
		5-5	-
		6-5	22279.6784
		5-4	22279.8182

Table G1 cont. – ${}^4R_{3e1e}$ Assignments for the ${}^{187}\text{ReC}$ Isotopologue in the 448nm Band

N''	J''	F'-F''	Peak Frequency (cm ⁻¹)
6	7.5	10-10	-
		11-10	22280.1033
		9-9	22280.4090
		10-9	22280.4261
		8-8	22280.6818
		9-8	22280.6977
		7-7	22280.9033
		8-7	22280.9172
		6-6	22281.0866
		7-6	22281.0958
		6-5	22281.2440
		7	
12-11	22281.4443		
10-10	22281.7421		
11-10	22281.7576		
9-9	-		
10-9	22282.0158		

	8.5	8-8	-
		9-8	22282.2433
		7-7	-
		8-7	22282.4290
		7-6	22282.5856
8	9.5	12-12	-
		13-12	22282.7070
		11-11	-
		12-11	22283.0062
		10-10	-
		11-10	22283.2697
		9-9	-
		10-9	22283.4937
		8-8	-
		9-8	22283.6850
		8-7	22283.8475

Table G1 cont. – ${}^t\text{R}_{3e1e}$ Assignments for the ${}^{187}\text{ReC}$ Isotopologue in the 448nm Band

N''	J''	$F'-F''$	Peak Frequency (cm^{-1})
9	10.5	13-13	-
		14-13	22283.8857
		12-12	-
		13-12	22283.1788
		11-11	22284.4269
		12-11	22284.4392
		10-10	-
		11-10	22284.6662
		9-9	-
		10-9	22284.8582
		9-8	22285.0243
10		14-14	-
		15-14	22284.9803
		13-13	-
		14-13	22285.2846
		12-12	-
		13-12	22285.5289

	11.5	11-11	-
		12-11	22285.7536
		10-10	-
		11-10	22285.9522
		10-9	22286.1249
11	12.5	15-15	-
		16-15	22285.9961
		14-14	-
		15-14	22286.2820
		13-13	-
		14-13	22286.5389
		12-12	-
		13-12	22286.7650
		11-11	-
		12-11	22286.9665
		11-10	22287.1343

Table G1 cont. – ${}^1R_{3e1e}$ Assignments for the ${}^{187}\text{ReC}$ Isotopologue in the 448nm Band

N''	J''	$F'-F''$	Peak Frequency (cm^{-1})
12	13.5	16-16	-
		17-16	22286.9270
		15-15	-
		16-15	22287.2015
		14-14	-
		15-14	22287.4589
		13-13	-
		14-13	22287.6846
		12-12	-
		13-12	22287.8893
		12-11	22288.0651
		17-17	-
		18-17	22287.7675
		16-16	-
		17-16	22288.0455
		15-15	-

13	14.5	16-15	22288.3044
		14-14	-
		15-14	22288.5104
		13-13	-
		14-13	22288.7372
		13-12	22288.9187
14	15.5	18-18	-
		19-18	22288.5325
		17-17	-
		18-17	22288.9187
		16-16	-
		17-16	22289.0652
		15-15	-
		16-15	-
		14-14	-
		15-14	22289.4984
		14-13	22289.6856

Table G1 cont. – ${}^1R_{3e1e}$ Assignments for the ${}^{187}\text{ReC}$ Isotopologue in the 448nm Band

N''	J''	$F'-F''$	Peak Frequency (cm^{-1})
15	16.5	19-19	-
		20-19	22289.2141
		18-18	-
		19-18	22289.4984
		17-17	-
		18-17	22289.7446
		16-16	-
		17-16	-
		15-15	-
		16-15	-
		15-14	-

Table G2 – ${}^PQ_{3e4f}$ Assignments for the ${}^{187}\text{ReC}$ Isotopologue in the 448nm Band

N''	J''	$F'-F''$	Peak Frequency (cm^{-1})
6	4.5	7-7	22260.6464
		6-6	22260.3100
		5-5	22260.0258
		4-4	22259.7886
		3-3	-
		2-2	22259.4900
7	5.5	8-8	22259.1368
		7-7	22258.8191
		6-6	22258.5474
		5-5	22258.3164
		4-4	22258.1290
		3-3	22257.9828
		9-9	22257.5553
		8-8	22257.2488

8	6.5	7-7	22256.9872
		6-6	22256.7579
		5-5	22256.5623
		4-4	22256.4006
9	7.5	10-10	22255.8889
		9-9	22255.5983
		8-8	22255.3377
		7-7	22255.1074
		6-6	22254.9095
		5-5	22254.7381
10	8.5	11-11	22254.1404
		10-10	22253.8575
		9-9	22253.6024
		8-8	22253.3755
		7-7	22253.1734
		6-6	22252.9985
11	9.5	12-12	22252.3166
		11-11	22252.0339
		10-10	22251.7849
		9-9	22251.5558
		8-8	22251.3483
		7-7	22251.1718

Table G2 cont. – $^pQ_{3e4f}$ Assignments for the ^{187}ReC Isotopologue in the 448nm Band

N''	J''	$F'-F''$	Peak Frequency (cm^{-1})
12	10.5	13-13	22250.4048
		12-12	22250.1318
		11-11	22249.8806
		10-10	22249.6567
		9-9	22249.4496
		8-8	22249.2677
13	11.5	14-14	22248.4081
		13-13	22248.1443
		12-12	22247.8973
		11-11	22247.6676
		10-10	22247.4622
		9-9	22247.2755
		15-15	22246.3355

14	12.5	14-14	22246.0742
		13-13	22245.8308
		12-12	22245.6064
		11-11	22245.3911
		10-10	22245.2022

Table G3 – $^{\circ}\text{P}_{3f4f}$ Assignments for the ^{187}ReC Isotopologue in the 448nm Band

N''	J''	$F'-F''$	Peak Frequency (cm^{-1})
3	1.5	3-4	22263.2424
		2-3	22262.7109
		1-2	22262.3404
		-	-
		-	-
		-	-
4	2.5	4-5	22261.0391
		3-4	22260.5783
		2-3	22260.2363
		1-2	-
		-	-
		-	-
		5-6	22258.7377

5	3.5	4-5	22258.3412
		3-4	22258.0304
		2-3	22257.8236
		1-2	22257.6500
		-	-
6	4.5	6-7	22256.3664
		5-6	22256.0114
		4-5	22255.7201
		3-4	22255.4836
		2-3	22255.2965
		1-2	22255.1560
7	5.5	7-8	22253.9081
		6-7	22253.5816
		5-6	22253.3044
		4-5	22253.0691
		3-4	22252.8743
		2-3	22252.7157
8	6.5	8-9	22251.3675
		7-8	22251.0604
		6-7	22250.7951
		5-6	22250.5590
		4-5	22250.3650
		3-4	22250.1990

Table G3 cont. – $^{\circ}\text{P}_{3f4f}$ Assignments for the ^{187}ReC Isotopologue in the 448nm Band

N''	J''	$F'-F''$	Peak Frequency (cm^{-1})
9	7.5	9-10	22248.7519
		8-9	22248.4544
		7-8	22248.1927
		6-7	22247.9627
		5-6	22247.7600
		4-5	22247.5891
10	8.5	10-11	22246.0513
		9-10	22245.7651
		8-9	22245.5078
		7-8	22245.2795
		6-7	22245.0734
		5-6	-

Appendix H

Assignments for the ^{185}ReC Isotopologue in the 448nm Band

Table H1 – ${}^1\text{R}_{3e1e}$ Assignments for the ^{185}ReC Isotopologue in the 448nm Band

N''	J''	$F'-F''$	Peak Frequency (cm^{-1})
3	4.5	7-7	-
		8-7	22276.2235
		6-6	22276.5774
		7-6	22276.6050
		5-5	22276.8559
		6-5	22276.8804
		4-4	22277.0649
		5-4	22277.0818
		3-3	-
		4-3	22277.2331
		3-2	22277.3382

4	5.5	8-8	-
		9-8	22277.7992
		7-7	22278.1297
		8-7	22278.1537
		6-6	-
		7-6	22278.4249
		5-5	-
		6-5	22278.6363
		4-4	22278.7866
		5-4	22278.7982
		4-3	22278.9210
5	6.5	9-9	-
		10-9	22279.3038
		8-8	-
		9-8	22279.6358
		7-7	-
		8-7	22279.9020
		6-6	-
		7-6	22280.1155
		5-5	-
		6-5	22280.2907
		5-4	22280.4261

Table H1 cont. – ${}^1R_{3e1e}$ Assignments for the ${}^{185}\text{ReC}$ Isotopologue in the 448nm Band

N''	J''	$F'-F''$	Peak Frequency (cm^{-1})
6	7.5	10-10	-
		11-10	22280.7264
		9-9	-
		10-9	22281.0430
		8-8	22281.2935
		9-8	22281.3084
		7-7	-
		8-7	22281.5250
		6-6	-
		7-6	22281.7031

		6-5	22281.8504
7	8.5	11-11	-
		12-11	22282.0609
		10-10	22282.3581
		11-10	22282.3725
		9-9	-
		10-9	22282.6371
		8-8	-
		9-8	22282.8581
		7-7	-
		8-7	22283.0392
		7-6	22283.1928
8	9.5	12-12	-
		13-12	22283.3271
		11-11	-
		12-11	22283.6336
		10-10	-
		11-10	22283.8857
		9-9	-
		10-9	22284.1049
		8-8	-
		9-8	22284.2970
		8-7	22284.4569

Table H1 cont. – ${}^tR_{3e1e}$ Assignments for the ${}^{185}\text{ReC}$ Isotopologue in the 448nm Band

N''	J''	$F'-F''$	Peak Frequency (cm^{-1})
9	10.5	13-13	-
		14-13	22284.5074
		12-12	-
		13-12	22284.8013
		11-11	-
		12-11	22285.0576
		10-10	-
		11-10	22285.2744
		9-9	-
		10-9	22285.4720

		9-8	22285.6397
10	11.5	14-14	-
		15-14	22285.6059
		13-13	-
		14-13	22285.8964
		12-12	-
		13-12	22286.1516
		11-11	-
		12-11	22286.3742
		10-10	-
		11-10	22286.5701
11	12.5	10-9	22286.7397
		15-15	-
		16-15	22286.6239
		14-14	-
		15-14	22286.9100
		13-13	-
		14-13	22287.1552
		12-12	-
		13-12	22287.3777
		11-11	-
12-11	22287.5787		
11-10	22287.7513		

Table H1 cont. – ${}^4R_{3e1e}$ Assignments for the ${}^{185}\text{ReC}$ Isotopologue in the 448nm Band

N''	J''	F'-F''	Peak Frequency (cm ⁻¹)
12	13.5	16-16	-
		17-16	-
		15-15	-
		16-15	22287.8341
		14-14	-
		15-14	22288.0838
		13-13	-
		14-13	22288.3118
		12-12	-

		13-12	22288.5104
		12-11	22288.6875
13	14.5	17-17	-
		18-17	-
		16-16	-
		17-16	22288.6875
		15-15	-
		16-15	22288.9317
		14-14	-
		15-14	22289.1700
		13-13	-
		14-13	22289.3637
		13-12	22289.5415
14	15.5	18-18	-
		19-18	-
		17-17	-
		18-17	22289.4482
		16-16	-
		17-16	22289.7073
		15-15	-
		16-15	-
		14-14	-
		15-14	-
		14-13	-

Table H2 – ${}^{\text{P}}\text{Q}_{3\text{e}4\text{f}}$ Assignments for the ${}^{185}\text{ReC}$ Isotopologue in the 448nm Band

N''	J''	F'-F''	Peak Frequency (cm ⁻¹)
6	4.5	7-7	22261.2343
		6-6	22260.9011
		5-5	22260.6264
		4-4	22260.4013
		3-3	22260.2147
		2-2	22260.0609
		8-8	22259.7271
		7-7	-

7	5.5	6-6	22259.1437
		5-5	22258.9169
		4-4	22258.7377
		3-3	22258.5759
8	6.5	9-9	22258.1461
		8-8	22257.8462
		7-7	22257.5836
		6-6	22257.3550
		5-5	22257.1618
		4-4	22257.0047
9	7.5	10-10	22256.4794
		9-9	22256.1894
		8-8	22255.9335
		7-7	22255.7064
		6-6	22255.5098
		5-5	22255.3572
10	8.5	11-11	22254.7305
		10-10	22254.4528
		9-9	22254.1999
		8-8	22253.9749
		7-7	22253.7722
		6-6	22253.6200
11	9.5	12-12	22252.9008
		11-11	22252.6301
		10-10	22252.3778
		9-9	22252.1553
		8-8	22251.9560
		7-7	22251.8000

Table H2 cont. – $^pQ_{3e4f}$ Assignments for the ^{185}ReC Isotopologue in the 448nm Band

N''	J''	$F'-F''$	Peak Frequency (cm^{-1})
12	10.5	13-13	22250.9948
		12-12	22250.7250
		11-11	22250.4793
		10-10	22250.2551
		9-9	22250.0514
		8-8	-
		14-14	22249.0034

13	11.5	13-13	22248.7383
		12-12	22248.4934
		11-11	22248.2702
		10-10	-
		9-9	-
14	12.5	15-15	22246.9273
		14-14	22246.6681
		13-13	-
		12-12	22246.2020
		11-11	22245.9959
		10-10	-

Table H3 – $^{\circ}P_{3f4f}$ Assignments for the ^{185}ReC Isotopologue in the 448nm Band

N''	J''	F'-F''	Peak Frequency (cm ⁻¹)
4	2.5	4-5	22261.6184
		3-4	22261.1970
		2-3	22260.8749
		1-2	22260.6083
		-	-
		-	22260.2363
		5-6	22259.3280

5	3.5	4-5	22258.9392
		3-4	22258.6381
		2-3	22258.3806
		1-2	22258.2350
		-	22258.0304
6	4.5	6-7	22256.9530
		5-6	22256.6060
		4-5	22256.3176
		3-4	22256.0773
		2-3	22255.9186
		1-2	22255.7201
7	5.5	7-8	22254.4964
		6-7	22254.1727
		5-6	22253.8980
		4-5	22253.6638
		3-4	22253.4730
		2-3	22253.3044
8	6.5	8-9	22251.9560
		7-8	22251.6518
		6-7	22251.3822
		5-6	22251.1549
		4-5	22250.9585
		3-4	22250.7951
9	7.5	9-10	-
		8-9	22249.0430
		7-8	22248.7834
		6-7	22248.5563
		5-6	22248.3502
		4-5	22248.1927

Table H3 cont. – $^{\circ}\text{P}_{3f4f}$ Assignments for the ^{185}ReC Isotopologue in the 448nm Band

N''	J''	F'-F''	Peak Frequency (cm^{-1})
10	8.5	10-11	22246.6354
		9-10	22246.3492
		8-9	22246.0973
		7-8	22245.8696
		6-7	-
		5-6	22245.5078

Appendix I

Assignments for the ^{187}ReC Isotopologue in the 462nm Band

Table I1 – ${}^t\text{R}_{3\text{ele}}$ Assignments for the ^{187}ReC Isotopologue in the 462nm Band

N''	J''	$F'-F''$	Peak Frequency (cm^{-1})
2	3.5	6-6	21654.5324
		7-6	21654.5896
		5-5	-
		6-5	21655.0048
		4-4	21655.2369
		5-4	21655.2754

		3-3	-
		4-3	21655.4685
		2-2	21655.5651
		3-2	21655.5883
		2-1	21655.6629
3	4.5	7-7	21655.9511
		8-7	21655.9959
		6-6	21656.3287
		7-6	21656.3656
		5-5	21656.6034
		6-5	21656.6345
		4-4	21656.8120
		5-4	21656.8374
		3-3	21656.9636
		4-3	21656.9850
		3-2	21657.0827
4	5.5	8-8	21657.2410
		9-8	21657.2807
		7-7	21657.5924
		8-7	21657.6250
		6-6	21657.8672
		7-6	21657.8938
		5-5	-
		6-5	21658.1025
		4-4	21658.2304
		5-4	21658.2626
		4-3	21658.3797

Table II cont. – ${}^1R_{3e1e}$ Assignments for the ${}^{187}\text{ReC}$ Isotopologue in the 462nm Band

N''	J''	F'-F''	Peak Frequency (cm ⁻¹)
		9-9	21658.4135
		10-9	21658.4473
		8-8	21658.7495
		9-8	21658.7763
		7-7	-

5	6.5	8-7	21659.0374		
		6-6	-		
		7-6	21659.2534		
		5-5	-		
		6-5	21659.4215		
		5-4	21659.5558		
6	7.5	10-10	21659.4607		
		11-10	21659.4902		
		9-9	21659.7850		
		10-9	21659.8014		
		8-8	21660.0435		
		9-8	21660.0626		
		7-7	-		
		8-7	21660.2787		
		6-6	-		
		7-6	21660.4585		
		6-5	21660.6021		
		7	8.5	11-11	21660.3844
				12-11	21660.4089
				10-10	-
11-10	21660.7164				
9-9	-				
10-9	21660.9735				
8-8	-				
9-8	21661.1913				
7-7	-				
8-7	21661.3809				
7-6	21661.5374				

Table II cont. – ${}^tR_{3e1e}$ Assignments for the ${}^{187}\text{ReC}$ Isotopologue in the 462nm Band

N''	J''	$F'-F''$	Peak Frequency (cm^{-1})
		12-12	21661.1806
		13-12	21661.2055
		11-11	-
		12-11	21661.5113
		10-10	-

8	9.5	11-10	21661.7646
		9-9	-
		10-9	21661.9889
		8-8	-
		9-8	21662.1827
		8-7	21662.3389
9	10.5	13-13	-
		14-13	21661.8860
		12-12	-
		13-12	21662.1827
		11-11	-
		12-11	21662.4407
		10-10	-
		11-10	21662.6653
		9-9	-
		10-9	21662.8581
		9-8	21663.0240
10	11.5	14-14	-
		15-14	21662.4407
		13-13	-
		14-13	21662.7328
		12-12	-
		13-12	21662.9914
		11-11	-
		12-11	21663.2145
		10-10	-
		11-10	21663.4107
		10-9	-

Table II cont. – ${}^4R_{3e1e}$ Assignments for the ${}^{187}\text{ReC}$ Isotopologue in the 462nm Band

N''	J''	F'-F''	Peak Frequency (cm ⁻¹)
		15-15	-
		16-15	21662.8780
		14-14	-
		15-14	21663.1641

11	12.5	13-13	-
		14-13	21663.4172
		12-12	-
		13-12	-
		11-11	-
		12-11	-
		11-10	-
12	13.5	16-16	-
		17-16	21663.1898
		15-15	-
		16-15	-
		14-14	-
		15-14	-
		13-13	-
		14-13	-
		12-12	-
		13-12	-
		12-11	-
13	14.5	17-17	-
		18-17	21663.3806
		16-16	-
		17-16	-
		15-15	-
		16-15	-
		14-14	-
		15-14	-
		13-13	-
		14-13	-
		13-12	-

Table II cont. – ${}^1R_{3e1e}$ Assignments for the ${}^{187}\text{ReC}$ Isotopologue in the 462nm Band

N''	J''	$F'-F''$	Peak Frequency (cm^{-1})
		18-18	-
		19-18	21663.3806
		17-17	-
		18-17	-

14	15.5	16-16	-
		17-16	-
		15-15	-
		16-15	-
		14-14	-
		15-14	-
		14-13	-

Table I2 – ${}^PQ_{3e4f}$ Assignments for the ${}^{187}\text{ReC}$ Isotopologue in the 462nm Band

N''	J''	$F'-F''$	Peak Frequency (cm^{-1})
3	1.5	4-4	21645.7260
		3-3	-
		2-2	-
		1-1	-

		-	-
		-	-
4	2.5	5-5	21644.3808
		4-4	21643.9674
		3-3	21643.6720
		2-2	21643.3948
		1-1	21643.2409
		-	-
5	3.5	6-6	-
		5-5	21642.5038
		4-4	21642.2156
		3-3	21641.9586
		2-2	21641.7827
		1-1	21641.6616
6	4.5	7-7	21641.2721
		6-6	21640.9186
		5-5	21640.6276
		4-4	21640.3838
		3-3	21640.1946
		2-2	21640.0531
7	5.5	8-8	21639.5260
		7-7	21639.1965
		6-6	21638.9134
		5-5	21638.6736
		4-4	-
		3-3	21638.3261
8	6.5	9-9	21637.6541
		8-8	-
		7-7	21637.0652
		6-6	21636.8287
		5-5	21636.6264
		4-4	21636.4615

Table I2 cont. – ${}^{\text{P}}\text{Q}_{3\text{e}4\text{f}}$ Assignments for the ${}^{187}\text{ReC}$ Isotopologue in the 462nm Band

N''	J''	$F'-F''$	Peak Frequency (cm^{-1})
9	7.5	10-10	21635.6517
		9-9	21635.3484
		8-8	21635.0839

		7-7	21634.8481
		6-6	21634.6497
		5-5	21634.4752
10	8.5	11-11	21633.5255
		10-10	21633.2364
		9-9	21632.9759
		8-8	21632.7463
		7-7	21632.5385
		6-6	21632.3622
11	9.5	12-12	21631.2789
		11-11	21630.9969
		10-10	21630.7360
		9-9	21630.5102
		8-8	21630.3086
		7-7	21630.1237
12	10.5	13-13	21628.9104
		12-12	21628.6375
		11-11	21628.3840
		10-10	21628.1559
		9-9	21627.9466
		8-8	21627.7619
13	11.5	14-14	21626.4196
		13-13	21626.1531
		12-12	21625.9003
		11-11	21625.6728
		10-10	21625.4641
		9-9	21625.2822
14	12.5	15-15	21623.8043
		14-14	21623.5413
		13-13	21623.3016
		12-12	-
		11-11	21622.8640
		10-10	21622.6658

Table I3 – ${}^{\circ}\text{P}_{3f4f}$ Assignments for the ${}^{187}\text{ReC}$ Isotopologue in the 462nm Band

N''	J''	F'-F''	Peak Frequency (cm^{-1})
3		3-4	21644.4582
		2-3	-
		1-2	21643.4578

	1.5	-	21643.1085
		-	21642.7193
		-	21642.4742
4	2.5	4-5	21642.1626
		3-4	21641.6616
		2-3	21641.2917
		1-2	21640.9787
		-	21640.6544
		-	21640.4234
5	3.5	5-6	21639.7458
		4-5	21639.3229
		3-4	21638.9771
		2-3	21638.7073
		1-2	21638.4142
		-	21638.1979
6	4.5	6-7	21637.2074
		5-6	21636.8292
		4-5	21636.5195
		3-4	21636.2630
		2-3	21635.9982
		1-2	21635.8067
7	5.5	7-8	21634.5416
		6-7	21634.1979
		5-6	21633.9094
		4-5	21633.6621
		3-4	-
		2-3	-
8	6.5	8-9	21631.7555
		7-8	21631.4346
		6-7	21631.1533
		5-6	21630.9161
		4-5	21630.6951
		3-4	21630.5370

Table I3 cont. – $^{\circ}\text{P}_{3f4f}$ Assignments for the ^{187}ReC Isotopologue in the 462nm Band

N''	J''	$\text{F}'\text{-F}''$	Peak Frequency (cm^{-1})
		9-10	21628.8480
		8-9	21628.5462

9	7.5	7-8	21628.2699
		6-7	21628.0336
		5-6	21627.8278
		4-5	21627.6562
10	8.5	10-11	21625.8183
		9-10	21625.5196
		8-9	21625.2584
		7-8	21625.0242
		6-7	21624.8206
		5-6	21624.6427
11	9.5	11-12	21622.6698
		10-11	21622.3812
		9-10	21622.1211
		8-9	-
		7-8	-
		6-7	-

Appendix J

Assignments for the ^{185}ReC Isotopologue in the 462nm Band

Table J1 – ${}^t\text{R}_{3e1e}$ Assignments for the ^{185}ReC Isotopologue in the 462nm Band

N''	J''	$F'-F''$	Peak Frequency (cm^{-1})
		6-6	21655.4323

2	3.5	7-6	21655.4640
		5-5	21655.8314
		6-5	21655.8788
		4-4	21656.1071
		5-4	21656.2981
		3-3	21656.1447
		4-3	21656.3287
		2-2	-
		3-2	21656.4546
		2-1	21656.5257
3	4.5	7-7	21656.8374
		8-7	21656.8757
		6-6	-
		7-6	21657.2410
		5-5	21657.4796
		6-5	21657.5069
		4-4	-
		5-4	21657.7039
		3-3	-
		4-3	21657.8508
4	5.5	8-8	21658.1230
		9-8	21658.1619
		7-7	-
		8-7	21658.5023
		6-6	-
		7-6	-
		5-5	-
		6-5	21658.9737
		4-4	-
		5-4	21659.1310
4-3	21659.2534		

Table J1 cont. – ${}^4R_{3e1e}$ Assignments for the ${}^{185}\text{ReC}$ Isotopologue in the 462nm Band

N''	J''	F'-F''	Peak Frequency (cm ⁻¹)
-----	-----	--------	------------------------------------

5	6.5	9-9	-
		10-9	21659.3294
		8-8	21659.6215
		9-8	21659.6493
		7-7	-
		8-7	21659.9044
		6-6	-
		7-6	21660.1164
		5-5	-
		6-5	21660.2787
		5-4	21660.4190
6	7.5	10-10	21660.3310
		11-10	21660.3644
		9-9	-
		10-9	21660.6770
		8-8	-
		9-8	21660.9346
		7-7	-
		8-7	21661.1465
		6-6	-
		7-6	21661.3252
7	8.5	6-5	21661.4729
		11-11	-
		12-11	21661.2830
		10-10	-
		11-10	21661.5924
		9-9	-
		10-9	21661.8451
		8-8	-
		9-8	21662.0624
		7-7	-
		8-7	21662.2502
7-6	-		

Table J1 cont. – ${}^4R_{3e1e}$ Assignments for the ${}^{185}\text{ReC}$ Isotopologue in the 462nm Band

N''	J''	$F'-F''$	Peak Frequency (cm^{-1})
-------	-------	----------	-------------------------------------

8	9.5	12-12	-
		13-12	21662.0839
		11-11	-
		12-11	21662.3824
		10-10	-
		11-10	21662.6401
		9-9	-
		10-9	21662.8581
		8-8	-
		9-8	21663.0530
		8-7	21663.2362
9	10.5	13-13	-
		14-13	21662.7606
		12-12	-
		13-12	21663.0530
		11-11	-
		12-11	21663.3147
		10-10	-
		11-10	21663.5272
		9-9	-
		10-9	21663.7344
		9-8	21663.9575
10	11.5	14-14	-
		15-14	21663.3147
		13-13	-
		14-13	21663.6018
		12-12	-
		13-12	21663.8567
		11-11	-
		12-11	21664.0783
		10-10	-
		11-10	21664.2808
		10-9	-

Table J1 cont. – ${}^4R_{3e1e}$ Assignments for the ${}^{185}\text{ReC}$ Isotopologue in the 462nm Band

N''	J''	F'-F''	Peak Frequency (cm ⁻¹)
11	12.5	15-15	-
		16-15	21663.7550
		14-14	-
		15-14	-
		13-13	-
		14-13	-
		12-12	-
		13-12	-
		11-11	-
		12-11	-
		11-10	-
12	13.5	16-16	-
		17-16	21664.0783
		15-15	-
		16-15	-
		14-14	-
		15-14	-
		13-13	-
		14-13	-
		12-12	-
		13-12	-
		12-11	-
13	14.5	17-17	-
		18-17	21664.2808
		16-16	-
		17-16	-
		15-15	-
		16-15	-
		14-14	-
		15-14	-
		13-13	-
		14-13	-
		13-12	-

Table J2 – ^PQ_{3e4f} Assignments for the ¹⁸⁵ReC Isotopologue in the 462nm Band

N''	J''	F'-F''	Peak Frequency (cm ⁻¹)
4	2.5	5-5	21645.1657
		4-4	21644.7971
		3-3	21644.5228
		2-2	21644.2683
		1-1	21644.0426
		-	21643.8730
5	3.5	6-6	21643.7262
		5-5	21643.3683
		4-4	21643.0794
		3-3	21642.8427
		2-2	21642.6289
		1-1	21642.4415
6	4.5	7-7	21642.1313
		6-6	21641.7986
		5-5	21641.4926
		4-4	21641.2721
		3-3	21641.0616
		2-2	21640.8701
7	5.5	8-8	21640.3838
		7-7	21640.0768
		6-6	21639.7773
		5-5	21639.5471
		4-4	21639.3465
		3-3	21639.1623
8	6.5	9-9	21638.5099
		8-8	21638.1979
		7-7	21637.9308
		6-6	21637.6928
		5-5	21637.4955
		4-4	-
9	7.5	10-10	21636.5000
		9-9	21636.2015
		8-8	21635.9438
		7-7	21635.7094
		6-6	21635.5122
		5-5	21635.3238

Table J2 cont. – ^PQ_{3e4f} Assignments for the ¹⁸⁵ReC Isotopologue in the 462nm Band

N''	J''	F'-F''	Peak Frequency (cm ⁻¹)
10	8.5	11-11	21634.3771
		10-10	21634.0891
		9-9	21633.8320
		8-8	21633.5956
		7-7	21633.3976
		6-6	21633.2156
11	9.5	12-12	21632.1295
		11-11	21631.8446
		10-10	21631.5941
		9-9	21631.3667
		8-8	21631.1613
		7-7	21630.9841
12	10.5	13-13	21629.7580
		12-12	21629.4810
		11-11	21629.2303
		10-10	-
		9-9	21628.8062
		8-8	21628.6221
13	11.5	14-14	21627.2613
		13-13	21626.9896
		12-12	21626.7495
		11-11	21626.5227
		10-10	21626.3230
		9-9	21626.1311
14	12.5	15-15	21624.6427
		14-14	21624.3749
		13-13	21624.1414
		12-12	21623.9561
		11-11	21623.7052
		10-10	21623.5213

Table J3 – ^oP_{3f4f} Assignments for the ¹⁸⁵ReC Isotopologue in the 462nm Band

N''	J''	F'-F''	Peak Frequency (cm ⁻¹)
3	1.5	3-4	21645.3510
		2-3	21645.0149
		1-2	21644.7042
		-	21644.3808
		-	21644.1535
		-	21643.9674
4	2.5	4-5	21643.0335
		3-4	21642.7193
		2-3	21642.3913
		1-2	-
		-	21641.8634
		-	-
5	3.5	5-6	21640.6075
		4-5	21640.3020
		3-4	21639.9555
		2-3	-
		1-2	-
		-	21639.2930
6	4.5	6-7	21638.0637
		5-6	21637.7590
		4-5	-
		3-4	-
		2-3	21636.9531
		1-2	21636.7891
7	5.5	7-8	21635.3958
		6-7	21635.0839
		5-6	21634.7858
		4-5	21634.5252
		3-4	21634.3263
		2-3	21634.1677
8	6.5	8-9	21632.6079
		7-8	21632.2934
		6-7	21632.0135
		5-6	21631.7736
		4-5	21631.5731
		3-4	21631.4090

Table J3 cont. – $^{\circ}\text{P}_{3f4f}$ Assignments for the ^{185}ReC Isotopologue in the 462nm Band

N''	J''	$F'-F''$	Peak Frequency (cm^{-1})
9	7.5	9-10	21629.6975
		8-9	21629.3930
		7-8	21629.1269
		6-7	21628.8919
		5-6	21628.6889
		4-5	21628.5174
10	8.5	10-11	21626.6636
		9-10	21626.3692
		8-9	21626.1138
		7-8	21625.8736
		6-7	21625.6728
		5-6	21625.4924
11	9.5	11-12	21623.5107
		10-11	21623.2283
		9-10	21622.9718
		8-9	21622.7193
		7-8	21622.5080
		6-7	21622.3267

Curriculum Vitae (CV)

Candidate's full name: Ryan Michael Joseph Hall

Universities attended:

Bachelor of Science (Chemistry Honours), University of New Brunswick,
2013

Master of Science (Chemistry), University of New Brunswick, 2016

Conference Presentations:

“High Resolution Laser Spectroscopy of Rhenium Carbide.” R. Hall, A. Adam,
and D. Tokaryk. 69th Meeting of the International Symposium on Molecular
Spectroscopy, University of Illinois, Champaign-Urbana, June 2014.

“An Analysis of the $4\Pi - X^4\Sigma^-$ Transition of Rhenium Monocarbide.” R. Hall, A.
Adam, and D. Tokaryk. 30th Meeting of the Symposium on Chemical Physics,
University of Waterloo, Ontario, November 2014.

“An Analysis of the $4\Pi - X^4\Sigma^-$ Transition of Rhenium Monocarbide.” R. Hall, A.
Adam, and D. Tokaryk. Science Atlantic – CIC Chemistry Conference
(ChemCon), University of New Brunswick, May 2015.